STUDY ON THE STRUCTURE OF TURBULENT SHEAR IN WALL NEAR LAYERS

By

RICHARD RUSHBY JOHNSON

A DISSERTATION PRESENTED TO THE GRADUATE COUNCIL OF
THE UNIVERSITY OF FLORIDA IN PARTIAL
FULFILLMENT OF THE REQUIREMENTS FOR THE DEGREE OF
DOCTOR OF PHILOSOPHY

UNIVERSITY OF FLORIDA
1974

DEDICATION

To Mom, Dad, and Grandma Rushby

for their constant love and support.

ACKNOWLEDGMENTS

In the fall of 1970 a hesitant young foreign student stepped into the office of Professor E. Rune Lindgren and was immediately bombarded with a fiery exposé on the state of the discipline in fluid mechanics. At first I was somewhat bewildered, but through the course of the next four years, I often found my way back to that office for stimulating discussions and informative encounters. I wish to thank Tex Lindgren for the way in which he has energetically taught and counselled me. His enthusiastic encouragement and questioning criticism have helped instill the necessary incentive to complete this dissertation. As my supervisory chairman, he has guided me both personally and professionally over the past four years.

My thanks go to Dr. Kurzweg for a most enjoyable series of class lectures, and for his lively and stimulating support of my work. I am grateful to Dr. Malvern for a welcome interest and many useful discussions. I wish to express my gratitude to Drs. R. J. Gordon and A. A. Broyles for their support as members of my supervisory committee, and to Dr. B. M. Leadon for his warm interest and encouragement.

I thank John Tang for his cheerful help with the experiments and Ric Schonblom for his ready assistance and companionship in the work done at Surge laboratory. I wish to express a special word of thanks to the Fung family: Yee-Tak for his close friendship and valuable help with the figures, and to Hope for her kind and cheerful assistance with the typing.

Thanks also to my close friends Karen Shelley, Wayne McKay, Arun Banerjee, Chang Sheng Ting, and Muvuro Simeon Zvobgo who have so well shared the excitement and disappointments of working on a dissertation, and who have contributed through discussion, encouragement, and companionship. Thanks to my brother Chris Johnson for his helpful remarks regarding the experimental arrangement, and to Norma Donovan for the typing of the final draft of this dissertation.

This work was supported in part by the National Science Foundation under Grant No. 24107 and in part by the Department of Engineering Sciences, University of Florida.

TABLE OF CONTENTS

		Page
ACKNOWLEDGMENTS		iii
LIST OF TABLES		vii
LIST OF FIGURES		viii
TABLE OF SYMBOLS		xiii
ABSTRACT		xv
CHAPTER 1	THE STUDY OF TURBULENCE	1
	Introduction	1
	General Background	3
	The Structure of Turbulence	7
	Measurements of Turbulence	10
CHAPTER 2	EXPERIMENTAL ARRANGEMENT	15
	Experimental Pipe Flow Facility	15
	Hot-Film Anemometer	18
	Prism, Trace-Particle Cinemometry for Three-Dimensional Flow Studies	19
CHAPTER 3	METHODS AND TECHNIQUES	25
	The Flow Apparatus and Its Operation	25
	The Hot-Film Anemometer	26
	Hot-Film Calibrations	27
	Hot-Film Measurements	33
	Studies Using a Microscope	35

		Page
	Trace-Particle Flow Visualization.....	37
	Calibration of the Prism for Three-Dimensional Flow Studies.....	42
	Computational Methods.....	44
CHAPTER 4	FLOW STUDIES BY THE HOT-FILM ANEMOMETER.....	51
	Calibration of the Hot-Film Anemometer.....	51
	Hot-Film Turbulence Measurements.....	68
	Measurements With a Microscope.....	74
CHAPTER 5	FLOW STUDIES BY THE PRISM, TRACE-PARTICLE METHOD.....	100
	Prism Calibration.....	101
	Trace-Particle Flow Measurements.....	101
CHAPTER 6	CONCLUSIONS.....	145
	Discussions of Recorded Features of Wall Turbulence.....	145
	Concluding Remarks.....	152
APPENDIX A	ANALYSIS OF THE RELATIONSHIP BETWEEN PARTICLE POSITION IN THE FLOW AND PARTICLE POSITION AS SEEN IN THE PRISM.....	158
APPENDIX B	COMPUTER PROGRAM FOR THE EVALUATION AND INTERPOLATION OF THE VELOCITY FIELD.....	164
BIBLIOGRAPHY.....		169
BIOGRAPHICAL SKETCH.....		174

LIST OF TABLES

Table		Page
4.1	Calibration values obtained by integration of the hot-film outputs from laminar velocity profiles in the pipe.....	53
4.2	Sample laminar velocity profile for the pipe.....	54
4.3	Calibration values obtained by integration of the hot-film outputs from laminar velocity profiles in the orifice.....	55
4.4	Sample laminar velocity profile for the orifice.....	56
4.5	Calibration of the hot-film anemometer by timing the motion of minute particles in the flow.....	63
4.6	Summary of measurements made with the hot-film anemometer.....	69
4.7	Sample set of velocity data measured with the hot-film anemometer for a Reynolds number of 6,500 and distance d_o = 1.4 mm.....	70
4.8	Microscope measurements at a Reynolds number of 9,000.....	95
4.9	Microscope measurements at a Reynolds number of 6,500.....	95
4.10	Microscope measurements at a Reynolds number of 4,000.....	96
5.1	Calibration values for the prism analysis.....	102
5.2	Averaged velocities obtained from the trace-particle measurements.....	104
5.3	Sample set of three-dimensional velocity data.....	117

LIST OF FIGURES

Figure		Page
2.1	Pipe flow apparatus with a close-up view of test section B	16
2.2	Details of the canopy	16
2.3	Schematic layout for the hot-film anemometer	20
2.4	Stereoscopic view with a prism	22
2.5	Glass prism mounted on a plexiglass pipe, with glycerin filling the space in between	23
3.1	Integration configurations for hot-film calibrations	30
3.2	Configuration for the trace-particle calibration of the hot-film sensor	31
3.3	Arrangement for locating the hot-film probe	34
3.4	Layout of the microscope, projector and pipe	36
3.5	General layout of the prism, projector, and pipe	40
3.6	The flow region	41
3.7	Grid placed in the pipe for calibration of the prism	43
3.8	Lattice for interpolation of velocity	49
4.1	Distribution of summation terms q for the orifice, $q = \pi\Delta r(E \cdot r)$, and for the pipe, $q = 2 \cdot E \cdot M$	58
4.2	Hot-film calibration values measured in the pipe	59
4.3	Approximations to the calibration curve	61
4.4	Calibration curve for the hot-film sensor	62

Figure		Page
4.5	Hot-film sensor showing free convection	65
4.6	Hot-film response in the immediate neighborhood of the wall	67
4.7	Mean-velocity distribution for a flow of Reynolds number 9,000	75
4.8	Mean-velocity distribution for a flow of Reynolds number 6,500	76
4.9	Mean-velocity profile for a flow of Reynolds number 4,000	77
4.10	Relative turbulence intensities for a flow of Reynolds number 9,000	78
4.11	Relative turbulence intensities for a flow of Reynolds number 6,500	79
4.12	Relative turbulence intensities for a flow of Reynolds number 4,000	80
4.13	Axial turbulence intensity for a flow of Reynolds number 9,000	81
4.14	Axial turbulence intensity for a flow of Reynolds number 6,500	82
4.15	Axial turbulence intensity for a flow of Reynolds number 4,000	83
4.16	Radial turbulence intensity for a flow of Reynolds number 9,000	84
4.17	Radial turbulence intensity for a flow of Reynolds number 6,500	85
4.18	Radial turbulence intensity for a flow of Reynolds number 4,000	86
4.19	Circumferential turbulence intensity for a flow of Reynolds number 9,000	87
4.20	Circumferential turbulence intensity for a flow of Reynolds number 6,500	88
4.21	Circumferential turbulence intensity for a Reynolds number of 4,000	89

Figure		Page
4.22	Summary of the mean-velocity profiles.....	90
4.23	Summary of the mean-velocity profiles in the wall region.....	91
4.24	Summary of the axial turbulence intensity profiles.....	92
4.25	Summary of the radial turbulence intensity profiles.....	93
4.26	Summary of the circumferential turbulence intensity profiles.....	94
4.27	Microscope measurement of the mean velocity profile for a flow of Reynolds number 9,000.....	97
4.28	Microscope measurement of the mean velocity profile for a flow of Reynolds number 6,500.....	98
4.29	Microscope measurement of the mean velocity profile for a flow of Reynolds number 4,000.....	99
5.1	Mean velocity profile.....	105
5.2	Relative turbulence intensities.....	106
5.3	Lattice for interpolation.....	109
5.4	The axial, radial, and circumferential planes.....	110
5.5	Summary sheet for figures of velocity field patterns.....	112
5.6	Velocity field for four axial planes at time t = 0.025 s.....	124
5.7	Velocity field on the circumferential plane $\Theta = -4°$ at time t = .025 s.....	125
5.8	Velocity field on the circumferential plane $\Theta = -2°$ at time t = .025 s.....	126
5.9	Velocity field on the circumferential plane $\Theta = 0°$ at time t = .025 s.....	127
5.10	Velocity field on the circumferential plane Θ 2° at time t = .025 s.....	128

Figure		Page
5.11	Velocity field on the circumferential plane $\Theta = 4°$ at time t = .025 s	129
5.12	Axial velocity field at three axial planes, at time t = .025 s	130
5.13	Axial-velocity field at three axial planes, at time t = .050 s	131
5.14	Velocity field on four axial planes at time t = .050 s	132
5.15	Velocity field on the circumferential plane $\Theta = -2°$ at time t = .050 s	133
5.16	Velocity field on the circumferential plane $\Theta = -2°$ at time t = .075 s	134
5.17	Axial-velocity field on three axial planes at time t = .075 s	135
5.18	Velocity field on five axial planes at time t = .075 s	136
5.19	Velocity field on six axial planes at time t = .125 s	137
5.20	Velocity field on five axial planes at time t = .275 s	138
5.21	Velocity field on three axial planes at time t = .300 s	139
5.22	Velocity field on three axial planes at time t = .325 s	140
5.23	Velocity field on three axial planes at time t = .375 s	141
5.24	Velocity field on the circumferential plane $\Theta = 4°$ at time t = .375 s	142
5.25	Velocity field for three axial planes at time t = .425 s	143
5.26	Velocity field on three axial planes at time t = .475 s	144
6.1	Summary of the velocity field in the axial planes	146

Figure Page

6.2 Summary of the axial-velocity field..... 147

6.3 Summary of the axial-radial velocity field..... 148

A-1 Prism mounted on the pipe..... 159

A-2 Stereoscopic effect for square pipe..... 162

TABLE OF SYMBOLS

a	distance of particle image from the prism-camera axis
b	length used in interpolation
d	particle diameter; distance from camera to pipe center
F	weighting function
h	distance from the camera to pipe center
R	pipe radius
Re	Reynolds number
r	radius
T_L	Lagrangian time scale
t	time
U,V,W	instantaneous velocities
$\overline{U},\overline{V},\overline{W}$	time-averaged velocities
u,v,w	fluctuating components of velocity
u',v',w'	turbulence intensities
u*	wall friction velocity
u^+	velocity ratio $\overline{U}/u^*$
x,y,z	cartesian co-ordinates
y	radial distance from the inner surface of the pipe
y^+	wall Reynolds number u^*y/ν

Greek Letters

γ	angle
δ	angle

Δ	increment
θ	angle; cylindrical co-ordinate
μ	viscosity
ν	kinematic viscosity
π	3.1416...
ρ	density
ϕ	angle
Ω	angle

Subscripts

a	air
B,C,D	point locations
g	glass, glycerin
o	centerline
P	point
p	pipe; plexiglass
w	water

Abstract of Dissertation Presented to the Graduate Council
of the University of Florida in Partial Fulfillment of the Requirements
for the Degree of Doctor of Philosophy

STUDY ON THE STRUCTURE OF TURBULENT
SHEAR IN WALL NEAR LAYERS

By

Richard Rushby Johnson

December 1974

Chairman: E. Rune Lindgren
Major Department: Engineering Sciences

Experimental studies are made on fully developed turbulent flows of water in a pipe of circular cross section by employing two different measuring techniques, flow visualization by trace particles, and hot-film anemometry. The two techniques demonstrate different descriptive approaches to self-preserving wall turbulence. By hot-film anemometry the flow field is explored point by point and the turbulence described in terms of average velocities and velocity correlations measured at these points, whereas by the trace-particle flow visualization the instantaneous three-dimensional velocity field is mapped out in space and time.

Hot-film calibrations are carried out for a velocity range of 1 to 100 mm/s. The calibration curve is found to exhibit a minimum velocity (1.4 mm/s) below which the hot-film sensor does not respond. The hot-film anemometer measurements concern the average velocity $\overline{U}$ and the turbulence intensities u', v', and w' along a pipe diameter for flows of Reynolds numbers 9,000, 6,500, and 4,000. At these low Reynolds number flows the shape of the average velocity profile is found to change significantly with Reynolds number. Measurements of the turbulence intensities

show a wide spread in values at these low Reynolds number flows, and the peak in the radial intensity profile reduces with decreasing Reynolds number and is expected to disappear at the Reynolds number of transition.

The trace-particle flow visualization technique is developed to obtain three-dimensional quantitative measurements of velocities in turbulent flow fields. Neutrally buoyant particles are added to the flow and their motions cinematographically recorded by viewing the flow through two faces of a glass prism. The glass prism affords a stereoscopic view of the flow field and permits the three-dimensional location of the illuminated particles viewed. The velocities are computed by measuring the change of particle positions from one cinematographic frame to the next and dividing by the time interval.

Utilizing the trace-particle method, measurements are made of the total instantaneous velocity vector field ($\overline{U}$ + u, v, w) in space and time for a Reynolds number flow of 6,500. The turbulent fluctuations in the wall near region are studied in detail and a sequence of four consecutive types of motion identified: the lifting of a low speed streak away from the pipe wall; the formation and rapid growth of a streamwise vortex; the sudden and strong radial velocity away from the wall region, followed almost immediately by a more chaotic but weaker motion; and an axial acceleration of the low speed streak near the wall.

Chairman

CHAPTER I
THE STUDY OF TURBULENCE

Introduction

There has long been interest in the study of turbulence and its phenomenology. Experimental studies on the transition process and on self-preserving turbulence such as those by Hagen (1839) and Reynolds (1883) show this early interest. While extensive research has been done since then, there is still no consistent theoretical or physical description which clearly answers certain fundamental questions. Questions such as: why, where, and how is turbulence exactly generated? by what mechanisms is turbulent energy created, transferred, and dissipated simultaneously? The difficulties in providing such answers are enormous. Experimental measurement of the appropriate flow quantities in their three-dimensional setting requires a record in space and time. The measuring instrument needs to be sensitive, fast responding, small, and rugged enough while not interfering with the flow pattern. Theoretically, there are not enough equations specified to solve for the numerous unknown quantities, and these equations are in addition partly non-linear. The combined difficulties have encouraged the growth of a symbiotic relationship between experimental and theoretical investigations. Experimental observations supply ideas for the theoretical analyses which in turn may indicate which measurements would be most useful.

Presently, the most extensively used instrument for the measurement of turbulent flows is the hot-wire or hot-film anemometer. Its

sensor is small, versatile, has a short response time, and operates over a wide range of velocities. It is well suited for obtaining time averaged quantities found in the statistical theories of turbulence and has supplied many of the present data on flow features. Hot-film anemometry, however, as all other techniques, has a limit to its capabilities. It cannot record data throughout a flow space simultaneously, nor can it function predictably in the regions extremely close to a boundary, where velocities are low and the calibration unclear. Several of the more recent theories and models of turbulent shear structure, such as the wave theory of M. Landahl (1967), the contrarotating vortex pair model of Bakewell & Lumley (1967) and the vortex stretching model of Kline, Reynolds, Schraub & Runstadler (1967) are concerned with the region very close to the boundary, and require information at many positions at the same time. The need for comprehensive and detailed data has led to the reconsideration of various flow visualization techniques during the course of the present study.

A detailed knowledge of the structure of non-isotropic wall turbulence of pipe flow is of vital importance to the understanding of the self-preservation mechanisms involved in bounded turbulent flows. Although turbulence is often defined as being irregular, as by Hinze (1959), it is the discernibility of statistically distinct average values of this irregular phenomenon that has formed the basis for most studies on turbulent structure. This discernibility has given some insight into the mechanisms involved. It is clear, however, that until both the relation between selected short and long time averages and the nature of repeated irregular motions are understood, there will not be a clear descriptive model of all features and events.

The importance of measurements of the detailed shear structure of turbulence is of more than academic interest in describing turbulence processes. Such processes and features are seen in many flow situations, and with more insight may be modified to allow for turbulence control or prediction. The drag reduction induced by the addition of polymers to turbulent flows is intimately connected with the turbulent shear structure, as is the prediction of the onset of transition or the criteria distinguishing between self-preserving and decaying turbulence.

During the course of the research presented in this dissertation a measuring technique was developed which was useful in obtaining numerous detailed data for turbulence structure evaluation. Initially,measurements were done with the hot-film anemometer. After recognition of the limitations involved, a visualization approach was adopted and developed. The three-dimensional motions of neutrally buoyant particles in the wall region of fully developed turbulent flow of water in a pipe of circular cross section were studied. The experiments were carried out at low Reynolds numbers, $3{,}500 \leq Re \leq 9{,}000$, in a pipe of 12.7 cm diameter, so as to have the turbulent events of a suitable size, strength, and duration, in order to show the continuity of concepts from the very first evidence of turbulence to turbulence of very high intensity.

General Background

Many descriptions of turbulence have been proposed. These descriptions usually fall into one of two categories. Either the model is explained in terms of the instantaneous values or in terms of time averages. For stability considerations, the Navier-Stokes equations are often applied directly. For fully developed turbulence, however, a time average of the Navier-Stokes equations is used. The averaging procedure first

indicated by Reynolds (1883) introduces additional time averaged correlation quantities, some of which are the familiar Reynolds stresses. There are two approaches for relating these Reynolds or eddy stresses to other flow parameters: the phenomenological and the statistical. The first seeks to establish some functional dependency for the Reynolds stress, usually by the assumption of some mechanism for generation of turbulence. Statistical theories consider the turbulent fluctuations as being random and are therefore suitable for an averaged description of flow fields.

Early studies on the nature of the structure close to the boundaries in self-preserving turbulence were mostly phenomenological. In order to explain the results of a series of heat conductivity experiments, Péclet & Masson (1860) hypothesized that the heat transferred between a body of fluid in violent motion and a bounding solid has to be conducted through a fluid film at the boundary. But it was Prandtl (1910) and then, independently, Taylor (1916) who proposed the laminar sub-layer hypothesis, maintaining that there was a thin layer of luid between the wall and the turbulent core, in which the fluid motion was smooth.

In a paper describing heat transfer measurements in pipe flow Eagle & Ferguson (1930) concluded that the laminar-film model alone was incomplete. They suggested that there was an intermediate layer in-between the laminar film and the turbulence. This middle layer was to have the properties of both the viscous wall layer and the turbulent core. The three zone concept was also given by von Kármán (1934).

The expression describing the velocity profile in the assumed laminar film is obtained directly by setting all turbulence terms to zero. In the turbulent region, however, the relationship between the Reynolds stresses and other flow variables must be established before

analysis is possible. To do this, Prandtl (1933) introduced the mixing-length theory which expressed the Reynolds stresses in terms of a length characteristic of the turbulent velocity fluctuations. As the name suggests the mixing-length may be described as the average length travelled by a small packet of fluid before it loses its identity by mixing with the flow. Prandtl then assumed that the mixing length was directly proportional to the distance from the wall. Von Kármán assumed that in the average, the local flow conditions at each point were similar, except for scale.

The statistical approach also attempts to supply extra relationships involving Reynolds stresses. These relationships provide a more complete averaged picture of turbulence. Taylor (1935) in a description of his statistical theory for turbulent flow suggested that a certain form of statistical correlation could be applied to the fluctuating velocities. These correlations are the time averaged product of two velocity components separated by some distance in space, or separated by some interval in time. For zero separation the correlations are identical with the Reynolds stresses and are known as autocorrelations.

The development of hot-film anemometry as a velocity measuring technique made correlation measurements, such as those by Dryden (1939) feasible. The statistical approach grew in prominence and stimulated analytical work on turbulent flows which were either isotropic or homogeneous, as for example the studies of von Kármán & Howarth (1938), Batchelor (1953) and Deissler (1958).

By applying the Fourier transform to the velocity correlation tensor, Taylor (1938) introduced the important concept of energy spectra for turbulence. The transform represents the velocity fluctuations as

a sum of sine waves of different amplitudes and frequencies. The transformed correlations appear as an energy spectrum in which the distribution of energy in turbulent flow fields is specified as a function of the frequencies contained in the velocity fluctuations. Taylor's consideration of the one-dimensional energy spectrum was extended to three dimensions by Heisenberg (1948). Because of the complexity of the three-dimensional spectrum, most studies such as those by Lin (1948), Townsend (1956) and Batchelor (1953) consider the one-dimensional spectrum in isotropic turbulence. In a comprehensive experimental study Laufer (1951; 1954) measured energy spectra for turbulent flows in two-dimensional channels and in circular pipes. These measurements were used by Hinze (1959) in his monograph on the structure of turbulence.

Both the phenomenological and statistical theories of turbulence are applied to the Navier-Stokes equations as modified by Reynolds. Unlike the turbulence structure studies, theoretical investigations on laminar instabilities do not employ averages, but rather the Navier-Stokes equations directly. The idea is to introduce small perturbations into the variables in these equations and see if the perturbations die out or grow. Rayleigh (1880) showed that the flow is unstable if the velocity profile possesses an inflexion point. Theoretical instability studies on laminar flow have been continued, among others, by Tollmien (1926), Taylor (1936), and Lin (1948), while experimental studies have been done by Schubauer & Skramstad (1949), Schubauer & Klebanoff (1956), Klebanoff & Tidstrom (1959) as well as Kovasznay et al. (1962). Theoretical studies on the transition process are conspicuously absent except for one work by Lindgren (1969), while experimental studies on the same subject are numerous, starting with Hagen (1839), Reynolds (1883), and

Schiller (1921). More recent studies have been presented, among others, by Lindgren (1954; 1957; 1959a,b,c; 1960a,b; 1962; 1963), Peters (1970), Wygnanski & Champagne (1973), and Wygnanski, Sokolov & Friedman (1974).

More recently the trend has been to integrate the ideas on instabilities with those of correlations and energy spectra in the study of fully developed turbulent flow. As this study expressly concerns the turbulence structure in self-preserving flow in pipes it is necessary to more fully review these recent trends.

The Structure of Turbulence

The classical investigations on the structure of self-preserving flows of air through two-dimensional channels and pipes of circular cross section by Laufer (1951; 1954) have been extended by Compte-Bellot (1965) and Coantic (1962; 1967a,b) to include more completely the viscous sublayer.(1) The trend in recent years has been to concentrate more and more on the structure of the sublayer in order to obtain more insight into the mechanism of self-preservation of turbulence. This is exhibited in a series of papers by Kline and co-workers (1959, 1965, and 1967). These investigations together with other important contributions by Popovitch & Hummel (1967), Willmarth & Tu (1967), and Bakewell & Lumley (1967) show that the sublayer connot be a passive region dominated by viscosity

(1) The smooth layer of Prandtl's (1910) laminar-film hypothesis became known as the viscous sublayer after it was convincingly shown not to be laminar (Fage & Townend (1932), Laufer (1951), and Nedderman(1961)). There is some question as to the usefulness of talking of a viscous sublayer when considering instantaneous values as in this study. Here the name viscous sublayer will be used for the zone $0 < y^+ < 10$ with the understanding that it defines only a flow region and not a flow structure. Similarly, the buffer zone which was proposed by Eagle & Ferguson (1930) will be taken as the zone $10 < y^+ < 40$. The wall Reynolds number y^+ is defined as $y^+ = u^* \cdot y/\nu$, where u^* = wall friction velocity; y = the radial distance from the wall; and ν = kinematic viscosity.

but plays an active role in generation and preservation of turbulent shear flow. This thinking is not new, and was pointed out seventeen years ago by Lindgren (1957; 1959a) when referring to observations by Fage & Townend (1932), but has become popular only recently.

Both theoretical and experimental advances have been made regarding the process of self-preservation and structure of turbulence. In proposing a linear model of turbulence, Schubert & Corcos (1967) assume that "the rest of the boundary layer is assumed to drive motion in the layer (in and somewhat outside the viscous sublayer) by means of a fluctuating pressure which is independent of distance from the wall." They used the ideas on turbulent pressure given by Corcos (1964). However, based on the conclusions of a spectral analysis, carried out on the wall pressure fluctuation correlations of Willmarth & Wooldridge (1962) by Corcos (1964), Landahl (1967) proposed a wave-guide model for turbulent shear flow. Waves of the kind suggested by Landahl (1967) were detected by Morrison & Kronauer (1969). Bakewell & Lumley (1967), using their own correlation measurements on turbulent flows of glycerin, performed an eigenfunction decompostion of the streamwise fluctuating velocity. The resulting dominant eigenfunction and a mixing length approximation were used in an analysis to present the dominant large scale structure in the viscous sublayer as "consisting of randomly distributed counterrotating eddy pairs of elongated streamwise extent" (Bakewell & Lumley, 1967). Maybe the most significant advance though, was the recognition by Kline, Reynolds, Schraub & Runstadler (1967) of well organized but intermittent sets of motions developing in the viscous sublayer and finally bursting strongly out away from the boundary.

From visual observations of a turbulent boundary layer Kline, Reynolds, Schraub & Ranstadler (1967) and Kim, Kline & Reynolds (1971) have described the sequence of events associated with a burst. In their description they see a low-speed streak "lifting" up from the wall. This lifting carries low momentum fluid into a faster moving zone and distorts the mean forward velocity profile until it produces a local inflexion point. The unstable profile (see Rayleigh, 1880) is followed by a sudden oscillation (most commonly a streamwise spiral as reported by Kline et al. (1971) and then "bursting" and "ejection"). The suggestion was that the oscillation was the result of a primary linear instability, and that bursting was a secondary instability. Corino & Brodkey (1969) also made visual observations, but in a pipe. They observed that: "the sublayer was continuously disturbed by small-scale velocity fluctuations of low magnitude and periodically disturbed by fluid elements which penetrated into the region from positions further removed from the wall. From a thin region adjacent to the sublayer, fluid elements were periodically ejected outward toward the centreline." The subsequent motion toward the boundary was called a "sweep".

Because long time averages would tend to obscure the detailed turbulence structure associated with these intermittent events, many investigations now consider either sampled or instantaneous velocity data. By taking two fluctuating velocity components u and v and classifying them according to their signs Wallace, Eckelmann & Brodkey (1972) were able to estimate the contributions of the ejection and sweep type motions to the Reynolds stress term. They found that both of the motions each contributed about 70% to the total shear stress. The negative contribution of 40% is attributed to interaction between the ejection and sweep

motions. Willmarth & Lu (1973) did similar measurements but with additional classification. Extending his original wave-guide model of 1967, Landahl (1972a,b and 1973) defined "wave breakdown" as "the onset of a violent small-scale secondary instability developing on a large-scale primary disturbance of wave-like travelling type," and then proposes that the breakdown may be a key element in a burst regeneration mechanism. These mechanisms have mainly been seen in turbulent flows at lower Reynolds numbers. Morrison, Bullock & Kronauer (1971) suggest that these events may not occur for Re > 30,000.

Measurements of Turbulence

Measurement of turbulence may at best be described as difficult. The varied spatial and temporal dependence of the variables, the three-dimensionality, and the requirement of minimum interference between measuring probes and flow structure make turbulence measurement a science of its own. The complexity involved has stimulated a wide range of measuring techniques, from the simple but very informative types of qualitative methods such as the trace-dye observations by Reynolds (1883) on transition, to the application of sophisticated quantitative techniques, such as the hot-wire measurements of Laufer (1951; 1954).

The history of turbulence measurement goes hand in hand with the development of the theories of turbulence. Sometimes the observations inspire an analysis and sometimes a theory initiates a particular type of measurement. Stanton (1916) noted that the laminar-film models of Prandtl (1910) and Taylor (1916) arose from heat transfer considerations, but could be best verified by velocity measurement. Stanton, Marshall & Bryant (1920) published the results of velocity measurements done with a Pitot-static tube on the flows of air in a pipe. After applying a

correction term they concluded that the experiments confirmed the existence of a laminar film; however, the skin friction factor calculated from the corrected profiles did not agree with the measured values.

Probably the best known pipe-flow measurements done with a pitot-tube are those of Nikuradse. Nikuradse (1930) described the results of experiments performed on the flow of water through brass pipes. The more complete report of these experiments was published in 1932 and was used extensively in texts on heat transfer. However, as Lindgren (1957) points out, the reports of 1930 and 1932 do not agree. The data of the measurements were all adjusted in the final report by a constant amount, which substantially changed the values closer to the boundary.

Hot-wire anemometry brought a new tool to the field of measurement in turbulence. The technique is based on the observation that the amount of heat transferred from a heated wire is a calculable function of the local mass flow rate. The operation of such hot-wire anemometers is given a lengthy description by Hinze (1959). There have been a large number of studies concerning hot-wire and hot-film anemometry, such as King (1914); Dryden & Kuethe (1929); Kovasznay (1947); Ling & Hubbard (1956); and Wood (1968), and at present it is the most common instrument for studying turbulence. As recently as 1971, however, Perry & Morrison (1971a,b) concluded that errors of up to 20% may be involved in the usual static calibration procedures, and that there may be up to 20% difference in intensity indicated when using different anemometer systems on the same flow.

Hot-wires were used very successfully by Laufer (1951; 1954) in his measurements near the boundary in channel and pipe flows. From correlation measurements he was able to estimate the terms constituting the

energy balance within the buffer zone. Bakewell & Lumley (1967) did measurements much closer to the wall, extending them into the viscous sublayer. Their experiments were carried out on the turbulent flows of glycerin in a cylindrical pipe.

The idea of visualization of flow patterns is not new. The dye experiments of Reynolds (1883) to show transition, are well known. Marey (1893) mixed wax and resin into small neutrally buoyant beads to be used as trace particles in water, whereas Eden (1912) mixed aniline and toluene together to form neutrally buoyant droplets. As early as 1902 Ahlborn sprinkled aluminum powder on water for studying surface flows, a technique which was also very successfully used by Prandtl & Tietjens (1925) in their visualization experiments of the flow around cylinders and airfoils. All visualization techniques, however, are not old. Baker (1966) describes an electrochemical method where the colour change in a pH indicator (thymol blue) is triggered by the local proton transfer reaction around the positive electrode of a d-c voltage supply. Also using electrodes and a voltage supply Kolin (1953) describes measurements made using the hydrogen bubbles generated at the cathode. Kolin (1944) also considered the method of electromagnetic velocimetry. The method is based on the induction of a potential gradient in the flow when a magnetic field is applied normal to the flow direction. Popovitch & Hummel (1967b) showed that electromagnetic radiation of appropriate wavelengths could be used to activate colour changes in certain dyes, and would therefore be suitable for flow visualization without introducing probes into the field.

The hydrogen bubble technique is of particular interest because of its use in the recent boundary layer studies by Kline, Reynolds &

Schraub (1967) and Kim, Kline & Reynolds (1971). The method was first described by Kolin (1953) and then again by Geller (1955). Cutter & Smith (1961) extended the ideas to study the flow around aircraft models in a tow tank, and by kinking the cathode wire they were able to generate filament lines of bubbles which originated at the kinks. Schraub, Kline, Henry, Runstadler & Littell (1965) made a major improvement by generating both "timelines" and streaklines simultaneously, thus producing the "combined-time-streak marker". A detailed error analysis of the hydrogen bubble technique was carried out by Schraub et al. (1965). Later Kline et al. (1967), and Kim et al. (1971) made excellent use of the technique in observing the "bursty" nature of the wall-near region in turbulent shear flow. They pulsed the cathode so as to produce lines of time-streak markers normal to the mean flow direction and were able to follow subsequent motions.

The use of trace particles in flow visualization has been known for a long time. In their ultramicroscope measurements, Fage & Townend (1932) describe in detail the motions very close to a wall, by observing tiny particles already present in the water. This type of approach was also used by Vogelpohl & Mannesmann (1946) and Bock (1963). Nedderman (1961) applied the concept of stereoscopic photography to measure three-dimensional velocities in the wall region of turbulent pipe flow. The trace particles considered were very small air bubbles and these were photographed simultaneously by two cameras placed at an angle to one another. An alternative method for obtaining three-dimensional perspective is that of van Meel & Vermij (1961). They illuminated the flow field with a system of parallel bundles of light of different colours and took colour photographs of the particle motions. The colour then defined the third

co-ordinate. Caffyn & Underwood (1952) and Nieuwenhuizen (1964) both describe rather novel, but different arrangements or mirrors so as to project two orthogonal veiws of a particle onto one camera frame. The recent pipe flow observations of Corino & Brodkey (1969) in which they followed colloidal sized particles (magnesium oxide) flowing in a liquid (trichloroethylene) show the usefulness of the trace-particle method even in modern investigations. However, care is needed in interpretation, as is well demonstrated by Hama (1962) and in particle selection, as is shown by the investigations of Roberson (1955).

CHAPTER 2
EXPERIMENTAL ARRANGEMENT

Experimental Pipe Flow Facility

Central to all the experiments performed in this study is the major pipe facility of Lindgren (described by Lindgren & Chao, 1969). The constant head, closed circuit arrangement is shown in figure 2.1. Distilled water from the constant-head tank F passes through the honeycomb straightener in the settling chamber G and into the sharp-edged entrance of the 23.6 m long, 0.127 m inner diameter plexiglass pipe A. From the test pipe A the water discharges into the 0.46 m diameter plexiglass access chamber B and on through the plexiglass return pipe C to the glassed centrifugal pump. This 0.8 m^3/min. Goulds pump supplies the water back into the head tank via the vertical pipe I. The overflow from the constant head tank flows down pipe J into the mixing tank E before feeding back into the pump. Tank E is also fed from storage tank K, which helps to maintain a steady supply pressure on the pump so as to avoid cavitation, and to ensure that the pressure drop in test pipe A remains steady.

The pump is flexibly attached to the return pipe C in order to insulate the main flow pipe A from the mechanical vibrations of the pump. Mixing tank E and the constant head tank F contain cooling coils to allow for water temperature control. Two thermometers are positioned in the water, one upstream of pipe A and the other in chamber B just downstream of A.

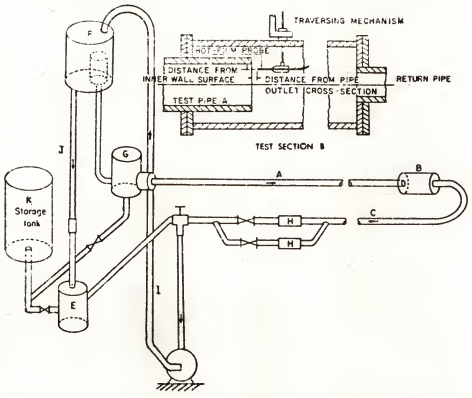

FIGURE 2.1 Pipe flow apparatus with a close-up view of test section B.

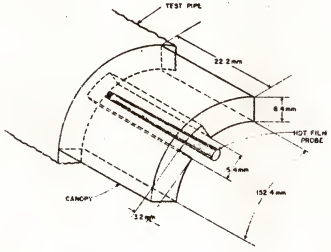

FIGURE 2.2 Details of the canopy.

Two Ramaco (Instrument Co., Inc. models V-3-SP and V-1-SP) flowmeters and two control valves, one in each branch of the return circuit C, are used to monitor and control the flow rate. The flowmeters are of a strain gauge type and record the turbulent drag on a thick nylon disc as a measure of the flow rate. The strain gauge is connected with a Wheatstone bridge and a voltage supply, and the output is recorded on a Honeywell Electronik 94 strip chart recorder. One of the flowmeters has a range of 0.008 to 0.08 m^3/min. while the other spans 0.08 to 0.8 m^3/min., thus allowing for close determination of the flow rate over a wide range of values.

The pipe A is very carefully aligned longitudinally with level and transit and is cradled by 1.2 m long angle-iron sections supported at each 1.3 m interval by steel pipe legs. The pipe of 0.635 cm wall thickness is made up of eleven pipe lengths with five permanent and five flange joints. The flanged couplings have locational spigots and are O-ring sealed. The inner diameter was checked to vary less than ± 0.5 mm over the pipe length.

Details of the test section B are shown in figure 2.1. Measurements employing the constant temperature hot-film anemometer were made in section B at the outlet end of pipe A. The pipe cross-section is traversed with the hot-film probe along a vertical diameter by means of a hand-operated traversing mechanism. The mechanism is mounted outside and on top of section B (sometimes placed in the horizontal position for horizontal traversing) and carries the probe holder on the end of a shaft passing through the wall of section B. For probe settings closer to the wall than 5.8 mm there is a micrometer built into the mechanism which can be adjusted to allow a positional accuracy of ± 0.01 mm. For probe

positions larger than 5.8 mm from the one inside surface of the pipe to within 5 mm of the opposite surface the distance may be set in 0.25 mm increments along a scale graduated in divisions of 0.1 inch and equipped with a vernier.

As shown in figure 2.2, the test pipe outlet end in the measuring section B is equipped with a canopy containing a slot in order to allow the traversing of the probe to zero distance from the tube wall, while at the same time jet diffusion effects of the flow are suppressed after it emerges from the test pipe. The 6.4 mm by 3.2 mm slot is just large enough to accommodate the probe and support, while the canopy extends the pipe by 22.2 mm and spans 152.4 mm circumference. The canopy is carefully matched to the pipe inside diameter.

Other special features of the pipe facility include deaerating pipes connected to the tops of the settling chamber G and the mixing tank E to allow the escape of entrained air. A Precision Scientific Co. water still supplies the distilled water utilized for the present experiments. No surfaces of system components in contact with the fluid flow are made of metal except for the Ramaco velocity meters which are made of stainless steel. In order to avoid fluid contamination the pump is glassed on the inside and the settling tank of steel is glass fiber lined.

Hot-Film Anemometer

The hot-film equipment consists of two model 1010 Thermo Systems Incorporated (T.S.I.) constant temperature anemometers, two model 1005B T.S.I. linearizers and an assortment of probes. The anemometer units supply the feedback control for constant temperature operation and monitor the primary output from the hot-film. The linearizers condition the

primary signal by squaring, balancing, and again squaring the signal so that the final output is directly proportional to the velocity (within some limits). Also included in the apparatus are two model 1060 T.S.I. Root Mean Square (RMS) voltmeters, a T.S.I. model 1015C correlator and two Honeywell Electronik 94 strip chart recorders. The typical arrangement for an x-probe experiment is shown schematically in figure 2.3.

The various probes employed include a T.S.I. model 1210-10W single probe and a T.S.I. model 1241-10W x-probe. The cross or x-probe has two independently mounted films which are each arranged to be 45° to the main-flow direction, but normal to one another. The cross probe thus measures two velocity components, one in the mean flow direction and the other normal to the mean flow, depending on the probe orientation. The leads from the hot-film connections to the anemometers are of matched length and resistance.

Prism, Trace-Particle Cinemometry for Three-Dimensional Flow Studies

For the flow visualization experiments only a few pieces of equipment other than the pipe facility are used. These include a Kodak carousel slide projector, a mirror, a glass prism, and a Bell and Howell Model 71 35 mm movie camera. The projector is utilized as a light source for illuminating the flow region with the help of the mirror by which the light beam from the projector may be properly directed inside the pipe. Trace particles of neutrally buoyant pliolite (supplied by Firestone Rubber Co.) are carried in the water while a Hewlett-Packard Model 5243L digital counter acts as a film timer.

The prism is employed so as to obtain the three-dimensional position of each trace particle. A stereoscopic view of the flow field under consideration is given by simultaneously observing views through two of

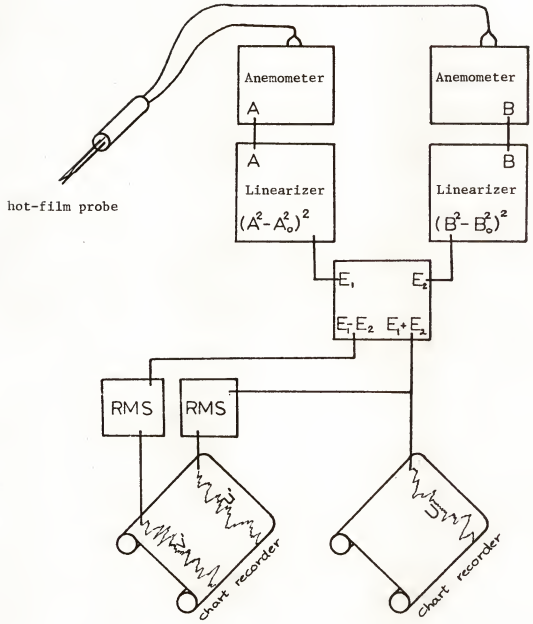

FIGURE 2.3 Schematic layout for the hot-film anemometer.

the faces of a prism as shown in figure 2.4. Thus a particle in the flow field is seen as an image in each of the prism faces. The distance of the images apart $(a_1 + a_2)$ is some measure of the distance d_1 of the particle from the third face of the prism. The distance $(a_1 - a_2)/2$ of the two images from the prism-camera axis is a measure of the distance d_2 of the particle itself from the same axis. The third co-ordinate of the particle is given by the axial distance of the two images from either prism end.

For the prism mounted on the pipe the relationships between the image co-ordinates in the prism and the particle co-ordinates are complicated by the curvature of the pipe, but may be derived as is done in Appendix A. Figure 2.5 shows the layout with the camera, the prism, and the pipe. The gap between the prism and the pipe is filled with glycerin (refractive index 1.474) which closely matches that of the glass (n = 1.475) and the plexiglass (n ≃ 1.49). In the analysis the prism, glycerin, and pipe wall are assumed to possess the same refractive index.

A cartesian co-ordinate system (x, y, z) with the origin at the pipe center and with the x-direction along the pipe axis is used. If subscripts are used to distinguish various points in the analysis (see figure 2.5), the results of the derivation of Appendix A may be summarized as:

$$\phi = \tan^{-1}[z_B/(d - h + \tan(\tfrac{\pi}{2} - \Omega)z_B)]$$

$$y_B = -\tan(\tfrac{\pi}{2} - \Omega)z_B + h$$

$$\delta = \sin^{-1}[\frac{n}{n_g} \cdot \sin(\tfrac{\pi}{2} - \Omega + \phi)]$$

$$A = 1 + \tan^2(\Omega + \delta)$$

$$B = 2\tan(\Omega + \delta)y_B - 2\tan^2(\Omega + \delta)z_B$$

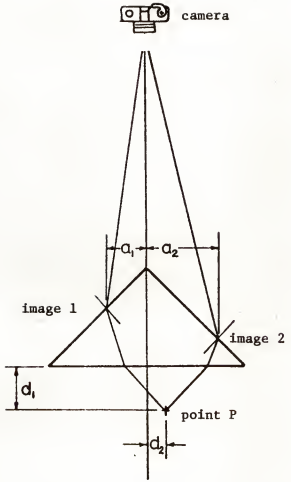

FIGURE 2.4 Stereoscopic view with a prism.

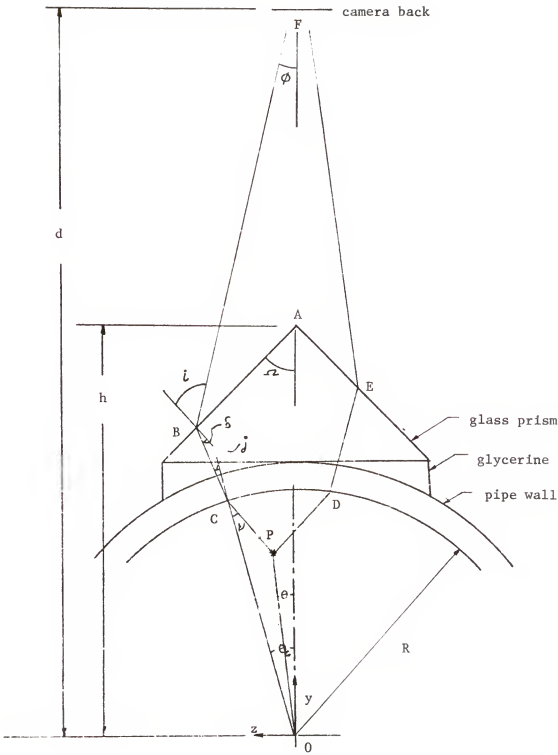

FIGURE 2.5 Glass prism mounted on a plexiglass pipe, with glycerine filling the space in between.

$$C = y_B^2 - R^2 + \tan^2(\Omega + \delta)z_B^2 - 2\tan(\Omega + \delta)z_B y_B$$

$$x_C = [-B + \sqrt{B^2 - 4AC}]/2A$$

$$\Theta_C = \tan^{-1}[x_C / \sqrt{R^2 - x_C^2}]$$

$$\nu_C = \sin^{-1}[\frac{n_g}{n_w} \cdot \sin(\frac{\pi}{2} - \Omega - \delta - \Theta_C)]$$

(2.1)

for an image point located at any positive co-ordinate position z_B. Each particle has two associated images, one at positive $z_B = a_1$ and one at negative $z_{B-} = -a_2$. The a_2 value is treated as positive in the relations above and it is recalled that $z_D + z_C$, $\Theta_D = \Theta_C$, and $\nu_D = \nu_{C-}$. By intersecting lines PC and PD the co-ordinates of P are given as:

$$z_P = \frac{[\tan(\frac{\pi}{2} - \Theta_D - \nu_D)z_D + \tan(\frac{\pi}{2} - \Theta_C - \nu_C)z_C - \sqrt{R^2 - z_C^2} + \sqrt{R^2 - z_D^2}}{[\tan(\frac{\pi}{2} - \Theta_C \quad \nu_C) + \tan(\frac{\pi}{2} - \Theta_D - \nu_D)]}$$

$$y_P = (z_P - z_C)\tan(\frac{\pi}{2} - \Theta_C - \nu_C) + \sqrt{R^2 - z_C^2}$$

(2.2)

x_p = axial distance from prism end of both images.

Thus the three-dimensional particle position (x, y, z) is given in terms of the measured values z_B, z_{B-}, and x_B of the image position in the prism faces, the refractive indices n_a, n_P, and n_w, and the geometry as given by d, h, and Ω. Details of this analysis as well as an analysis applied to a square pipe are given in Appendix A.

CHAPTER 3
METHODS AND TECHNIQUES

The following descriptions give in some detail the various methods used and the different techniques employed. The careful explanations of the experimental procedures are essential for evaluation of results presented later. The discussion concerns the operation of the pipe flow facility, the velocity measurements, and the computational procedures. Three velocity measuring techniques have been used: hot-film anemometry, microscope observation, and cinematographic recording of trace-particle motions.

The Flow Apparatus and Its Operation

The operation of the pipe flow apparatus is straightforward. Providing there was enough distilled water in the storage tank the pipe was filled and the pump started. The entrapped air in the tank was exhausted through the deaerating tube, while the air bubbles trapped in the pipe itself were released through two pressure taps. The flow rate was adjusted by means of the control valve to give the desired value of the flowmeter output. The water coolers were switched on and the water temperature checked every ten minutes. The temperature in the laboratory is thermostatically regulated for 20 ± 0.5°C and the amount of cooling was adjusted to keep the temperature of the fluid flow constant. The velocity measurements were usually performed one hour after starting the pump, when stable temperature conditions prevailed.

Certain elementary precautions were observed. The pump was not run unless there was enough supply pressure from the storage tank to avoid cavitation. All air was purged from the system. The overflow was always checked before making flow rate, or velocity measurements. The temperature variation had to be less than 0.10°C over 30 minutes before performing measurements, and the flow was never reversed when filters were in use in the flow circuit.

Calibration of the two flowmeters was done by the bucket and stopwatch method. The return flow was diverted by a valve immediately upstream of the pump, leading the water to a collecting bucket, the pump being supplied by water from the storage tank. For lower flow rates, measurements were performed with the pump both on and off to check for pump vibration effects. There were none. Only the smaller flowmeter was used in the present study.

The Hot-Film Anemometer

Standard operation procedures as indicated in the Thermo Systems, Inc. (T.S.I.) manuals were observed. A schematic of the typical x-probe arrangement is shown in figure 2.3. After allowing the appropriate warm-up time for each piece of electronic equipment and after allowing the water to reach operating temperature the "cold" resistance of each film was measured. The overheat ratio, or ratio of the hot-film operating resistance to the cold-film resistance was set at 1.04 for x-probe or 1.08 for single film probes. The low values of overheat ratio made the system very sensitive to temperature changes in the water, but reduced wall proximity effects when the probe was near the boundary. The low ratio also prevented bubble formation on the hot film.

The anemometer bridge was balanced with the flow at rest, and the probe positioned well away from any boundary. The output from the anemometer was carried to the linearizer, where it was squared, and then zeroed by subtracting out the full "at rest" signal. The Root Mean Square (R.M.S.) voltmeters and the strip chart recorders were all zeroed and balanced for the no-flow condition.

To run the system for velocity measurements, the flow was set to the desired value and the probe positioned at the desired location. Then, with no change in electronics, the output signal, after a second squaring in the linearizer, was regarded as being the measure of velocity. The relationship between velocity and linearizer output was not quite linear at the lower velocities as reported in detail below. The time constant on the R.M.S. voltmeters was set at 100 seconds. In order to insure a good average when recording turbulence, a time record of 15 minutes was taken for each location.

Hot-Film Calibrations

Calibration of the hot-film anemometer was done by several techniques in the very low velocity range 1 to 100 mm/s. The first was to tow the submerged hot-film sensor along a 3.5 m tank filled with water. The probe was suspended from the underside of a platform, and could be lowered into the water in the tank of 0.14 m^2 square cross section. The platform ran on a set of rails mounted on the tank sides and was towed by a constant speed motor. There was a variety of pulley ratios available for the motor, thus allowing different platform speeds. Stopwatch measurements were made as the sensor travelled over a distance of 0.6 m near the mid-section of the tank. The hot-film output was recorded on the strip chart recorder. Persistent vibration problems with the carriage and water contamination led to inconsistent results for low velocities.

The tow tank was the only moving sensor arrangement. In other techniques the sensor was held still and the fluid velocity over the sensor was recorded. Several configurations were attempted, but the most successful was to utilize the test pipe itself. It was hoped that under laminar flow conditions simple center-line hot-film measurements could be compared with average flow values assuming parabolic velocity profiles. However, very small temperature gradients in the fluid as caused by air currents in the laboratory, coupled with the low flow velocities, caused the velocity profile to be asymmetric in the vertical plane. Therefore, it became necessary to integrate hot-film calibration readings over the whole diameter and compare with each flow rate. Initially, a 63.5 mm diameter sharp edged orifice plate was placed inside the pipe just upstream of the sensor so as to produce nearly slug flow for calibration purposes. Subsequently, the orifice was removed and calibration readings were performed for laminar pipe flow.

For the calibration in the laminar flow range, the actual average velocity was obtained from the flowmeter readings of flow rate. At the same time, a complete traverse of the vertical pipe diameter was made using the hot-film anemometer, taking measurements every 3.5 mm. The velocity profile was integrated over the pipe cross section to obtain an estimate of the flow rate Q in terms of the hot-film output. The horizontal velocity-profiles were also measured and were found to be uniform for the orifice, or symmetrically parabolic for the fully developed laminar flow in the pipe. Therefore, for the orifice the volume flow rate was estimated from the hot-film measurements by applying a stepwise summation procedure. Each element was a cylindrical shell truncated at

a height corresponding to the velocity profile at that radius. The procedure yields

$$Q = \Sigma\ \pi r(U_r + U_{-r})\Delta r$$

where r = radius, Δr = radius increment between readings, U_r = velocity at radius r above the orifice centerline (in hot-film output) and U_{-r} = velocity at radius r below the centerline. For the measurements at the pipe outlet the summation was performed by adding together elements of parabolic shape. The height of each element was equal to the hot-film voltage output at each measurement station on a vertical diameter, while the base was equal to the horizontal measure of the pipe at that station. From this

$$Q = \Sigma\ 1.33\ U_r\ \sqrt{2Ry - y^2}\ \cdot\ \Delta y$$

where R = pipe radius, y = radial distance from the wall, and Δy = the increment in y.

Both of these integrating configurations are shown in figure 3.1. Also shown in figure 3.1 is the case of choosing a linear rather than parabolic horizontal velocity profile. It underestimates the flow rate while a direct average of the measured profile multiplied by the cross-sectional area overestimates the flow rate. This gives an upper and lower bound to the possible error involved.

Another approach was to obtain the velocity of the fluid in the neighborhood of the hot-film by flow visualization. Minute particles already present in the distilled water were made quite clear by strong illumination. The hot-wire sensor was placed at the pipe centerline. A 500 watt slide projector was used to project a plane of light 3 mm thick and 75 mm wide; the arrangement is seen in figure 3.2. The illuminating plane was made to lie parallel with the laminar flow, and

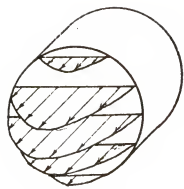

parabolic

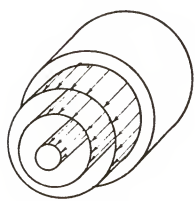

uniform

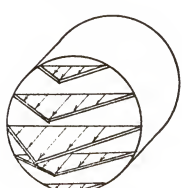

linear

FIGURE 3.1 Integration configurations for hot-film anemometer calibrations.

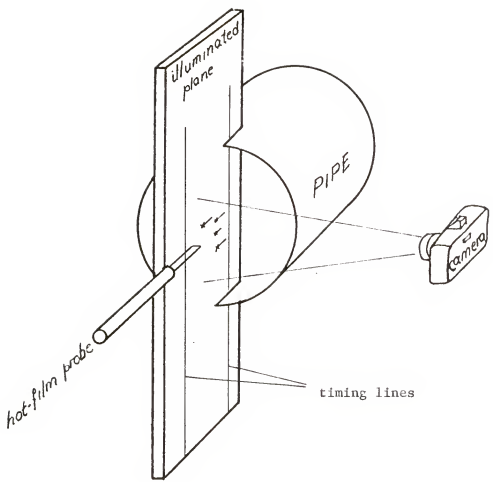

FIGURE 3.2 Configuration for the trace-particle calibration of the hot-film sensor.

to include the hot-film sensors. For higher velocities (above 6 mm/s) the illuminated plane was photographed with a Tetronix Polaroid camera. The streak exposures were taken on a one second speed setting, which was itself checked against an oscilloscope time base. For the lower velocities the particles were timed over a central span with a stop-watch while observing the plane with the naked eye. A 75 mm measuring length was marked in the light beam by two lines on a transparent slide in the projector. Measurements were made both above and below the hot-film probe, and for each flow setting the profile in the probe neighborhood was plotted. The velocity at the sensor itself was estimated from the profile. This technique was successful and laid some of the groundwork for the trace-particle measurements that were done later.

The calibrations described were not quite sufficient to fully interpret the hot-film measurements. Calibrations were not made under turbulent conditions, and were not influenced by the effects of a nearby boundary. The effect of the boundary on the sensor was carefully recorded for "zero flow" conditions. With the flow at rest, the probe was moved closer and closer to the boundary, and the output recorded. Thereafter, the near-boundary zone was similarly traversed under laminar flow conditions. It is assumed that in the region close to the boundary (less than 5 mm from the wall) the velocity profile is approximately linear and that the velocity at 5 mm from the wall may be obtained from the regular calibration curve, allowing calibration for specified wall near positions. This was done at several laminar flow rates. The method does not solve the problem of calibration under turbulent conditions and its velocity range is less than that for the turbulent flow.

Hot-Film Measurements

By using a constant temperature hot-film anemometer, extensive velocity measurements were performed on fully developed turbulent flows of water in the 12.7 cm test pipe. The hot-film probe was mounted at the outlet end of the pipe and could be traversed along a diameter as described in Chapter 2. The water was drained from the system, and either a cross or single sensor probe was placed in the holder and moved to the wall position. The horizontal distance d_o between the pipe outlet plane and the hot-film sensor was approximately set and the probe clamped. The distance was then measured with an optical cathetometer as shown in figure 3.3 which determined the setting to within ± 0.03 mm. The reference setting of the probe relative to the inner tube surface was also done with the cathetometer with the help of an arrangement of mirrors as shown in figure 3.3. For the x-probe these settings were made with respect to the center of the cross, and the probe was oriented as required by the velocity components to be measured.

The centerline position, and intermediate stations y/R = 0.7, 0.5, 0.4, 0.3, 0.25, 0.20, 0.15, 0.10, 0.07, 0.05, 0.04, 0.03, 0.025, 0.020, 0.017, 0.015, 0.012, 0.010, 0.007, 0.005, and -0.005 were calculated in terms of readings on the traversing mechanism relative to the wall reference settings. Here y = distance from the inner surface of the pipe, and R = radius of the pipe = 63.5 mm. For cases of measurements taken upstream of the outlet end of the pipe, location of the probe tip was possible only to a wall near position of y/R not less than 0.02. The order in which these positions were traversed was randomized, in order not to interpret a systematic drift as a radial dependency.

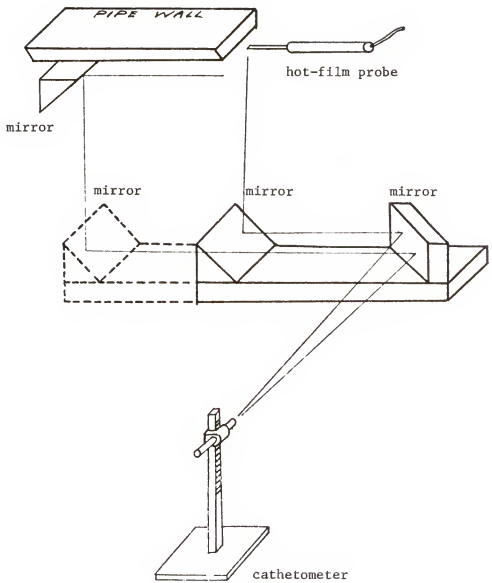

FIGURE 3.3 Arrangement for locating the hot-film probe.

Repeated checks on both flow and anemometer conditions were done by locating the probe at the centerline of the pipe for every fourth set of turbulent flow data readings. The water temperature at the pipe outlet was read on the thermometer located in the settling chamber B, for every hot-film reading. The flow rate was recorded for every probe location.

Measurements of the mean axial velocity $\overline{U}$ and the axial turbulence intensity u' were made with single sensor probes. With the cross probe it was possible by subtracting and adding the signals from each of the two hot-film sensors to obtain v' and $\overline{uv}$ or w' in addition to $\overline{U}$ and u'. Here v = the fluctuating radial velocity and w = the fluctuating circumferential (or azimuthal) velocity. The combination depends on the probe orientation.

Studies Using a Microscope

For the zone very close to the pipe wall the hot-film anemometer is not altogether successful because of boundary effects and low velocities encountered. In order to supplement the average velocity measurements in the immediate neighborhood of the boundary, and in order to establish by measurement the condition of "no-slip" at the wall some readings were taken using a microscope. The flow region close to the boundary was strongly illuminated showing particles similar to those utilized for the hot-film calibrations. Their size was later estimated to be between 5 and 20 microns. The microscope was mounted normal to the pipe axis and focused on the inner surface of the pipe as is shown in figure 3.4.

The microscope focuses on a 5.6 mm diameter area, and has a 2.5 mm scale with 0.025 mm divisions in the view. The microscope was mounted on

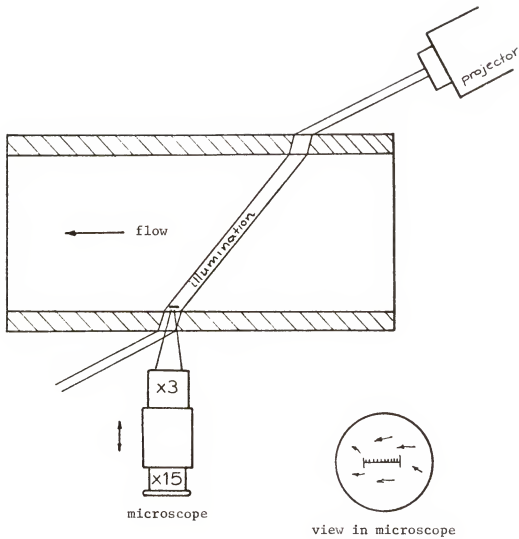

FIGURE 3.4 Layout of the microscope, projector, and pipe.

a threaded collar for focusing and advancing the microscope 0.51 mm per turn. The depth of view was approximately equivalent to 1/16 turn (0.03 mm). When using the microscope the reference point for focusing on the inner pipe surface was noted, then the collar was advanced 1/8 turn. This corresponds to a microscope difference in distance of a 0.06 mm increment. For each increment the new focal plane then increased a distance y from the inner pipe surface. Distance y is equal to the distance moved by the microscope multiplied by the refractive index of water.

The illuminated particles were seen through the microscope and the hairline scale was aligned parallel to the pipe axis. With a stopwatch the particles were timed over a 2.54 mm or 5.08 mm span. Because the flow was turbulent, 20 such readings were made at each setting, and the average velocity computed. The highest recorded velocity was 3.2 mm/s and the method was only useful within a 1.3 mm distance from the wall.

Trace-Particle Flow Visualization

The use of particles already present in the distilled water, and the incompleteness of the hot-film measurements stimulated an interest in the trace particle technique. After some difficulties and trial and error work, the technique was successfully employed. Neutrally buoyant particles of 48 to 63 microns in size were added to the flow. The material used was "pliolite", and it is supplied in large pea-sized kernels by Firestone Rubber Co. The pliolite was ground in a colloidal mill and then sieved. The particles of a given size range were vigorously mixed with distilled water and then allowed to stand for 1 hour. The floating particles were scooped off and thrown away, the decanted water containing the neutrally buoyant particles was then added to the main flow circuit through the supply tank. The size of the

neutrally buoyant particles (48-63 microns) was chosen to be small enough to closely follow the fluid motion, but yet be large enough to be conveniently photographed. The response of the particles to the turbulent velocity fluctuations can only be estimated. Hinze (1959) comments: "Theoretically very little is known about the fluid dynamics of a mixture of discrete particles of arbitrary size and concentration with a fluid, where both are in turbulent motion."

By considering the equations and assumptions for particle motion made by Tchen (1947) and modified by Corrsin & Lumley (1956) (as cited in Hinze (1959)) it may be shown that for homogeneous turbulence the ratio of the mean square of the particle-velocity fluctuations to the mean square of the fluid-velocity fluctuations may be written as:

$$\frac{u'_p}{u'} = (\alpha T_L + \beta^2)/(\alpha T_L + 1)$$

where $\alpha = 36\ \mu/(2\ \rho_p + \rho)d^2$, $\beta = 3\ \rho/(2\ \rho_p + \rho)$ and T_L = Lagrangian time scale $= \int_0^\infty R_L(\tau)d\tau$. For the case considered here the particle density ρ_p closely equals the fluid density ρ, d is the diameter of the particle, and μ the fluid viscosity. This ratio only strictly applies to situations where (see Hinze (1959)): (1) the turbulence is homogeneous, (2) the domain of turbulence is infinite in extent, (3) the particle is spherical and so small that its motion relative to the ambient fluid follows Stokes' law of resistance, (4) the particle is small compared with the smallest wavelength present in the turbulence, and (5) during the motion of the particle the neighborhood will be formed by the same fluid particles. The Lagrangian time correlation here is assumed an exponential function of the Lagrangian time scale T_L for short times, namely

$$R_L(\tau) = \exp(-t/T_L)$$

for time t.

The condition of flow homogenity is here satisfied in only one direction, and the second condition limits discussion to the core region of flow. The particles are not spherical but are considered small enough to respond according to the Stokes law of resistance for a possible relative velocity between particle and fluid. Condition five is described by Hinze (1959) as being the difficult one to satisfy because of the deformable property of a fluid packet as compared with the solid particle, and is only satisfactorily approximated by small particles of density close to that of the fluid, as in the present case. The low velocities encountered (less than 65 mm/s) and the low Reynolds number of 6,500 ensure that the particles are able to closely follow the average motions of flow.

The quantity $\beta = 3\rho/(2\rho_p + \rho)$ is very close to one for the almost zero density-difference between particle and fluid. Also, the quantity $\alpha T_L = 36\ \mu T_L/(2\ \rho_p + \rho)d^2 \simeq 12\ T_L\ \nu/d^2 \simeq 4{,}800\ T_l$ is quite large even for a small Lagrangian time scale T_L. Brodkey (1967) gives a parameter to be added to the particle-to-fluid intensity ratio for the wall effect, if the particle is near a boundary. The parameter is $(\beta/32)(d/y)^3$, where y is the distance of the particle from the wall. Even for y = d the parameter is only 1/32. Therefore, the particle may be expected to follow not only the average motions closely, but also the fluctuations.

An illuminated flow region 0.5 m from the outlet end of the pipe was viewed through the glass prism. Enough particles were added so as to ensure that there were always more than sixty within the flow region behind the prism shown in figure 3.6. As already described, the illumination of the particles was done by means of a light beam from a 500 W

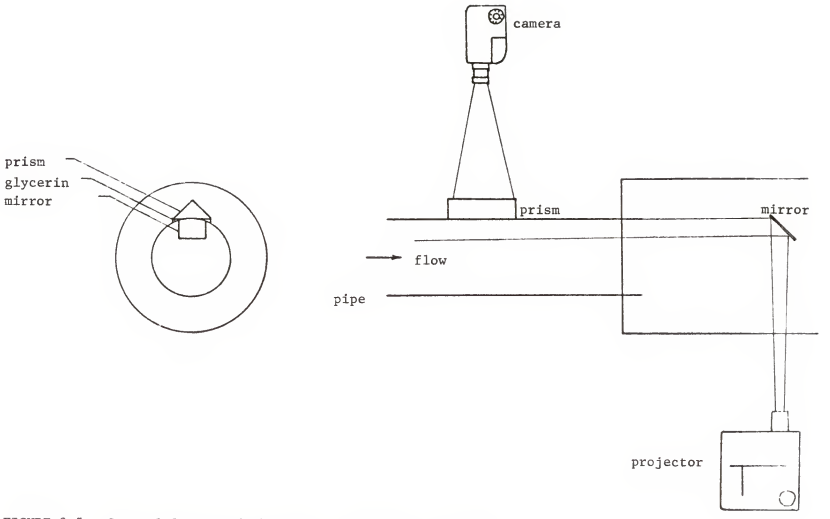

FIGURE 3.5 General layout of the prism, projector, and pipe.

radial plane
chosen for
averaging
velocities

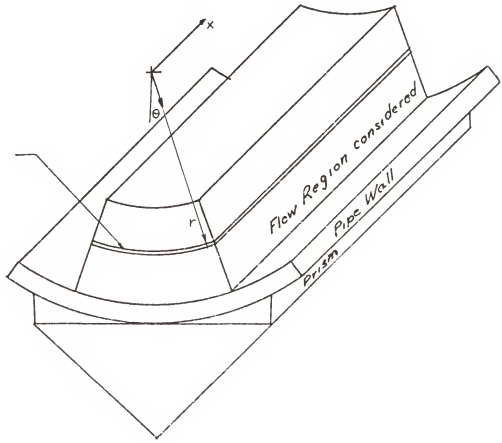

FIGURE 3.6 The flow region.

projector directed along the inside of the pipe through a mirror placed in the work section B (see figure 3.5). The particle motions were recorded cinematographically through both the prism faces simultaneously. Initially, an attempt was made to obtain streak pictures (approximately 5 frames per second). Because of the short time spans desired and the focusing difficulty, however, it was found preferable to make a cinematographic record at some higher speed (about 40 frames per second) and measure the change in particle position from one frame to the next. The particle positions are given in three dimensions by the two images seen in the prism faces as exp ined in Chapter 2. The camera was mounted 55.8 cm from the center of pipe, and the 150 mm telephoto lens with a close-up attachment allowed for suitable focus.

In order to transfer the film records, each frame of the film was fixed in a slide mount, projected, enlarged, and copied onto graph paper. The image pairs were identified and each particle path was traced on another sheet of graph paper. This procedure checked the continuity from one frame to the next and ensured that image pairs were correctly identified. The three co-ordinates associated with each image pair were written down for each time frame. These co-ordinates were then used in the prism analysis equations (2.1) and (2.2). The reading accuracy on the graph sheet is estimated at $\pm$ 0.12 mm which approximately corresponds to a $\pm$ 0.02 mm accuracy in the flow field itself.

Calibration of the Prism for Three-Dimensional Flow Studies

Equations (1.1) and (1.2) derived in the prism analysis, and used in the evaluation of the trace-particle data were checked by a calibration procedure. A grid of known cylindrical co-ordinates (x, r, θ) was placed in the pipe, as is shown in figure 3.7. The grid was scribed onto the edge of a plexiglass plate, which was machined to form

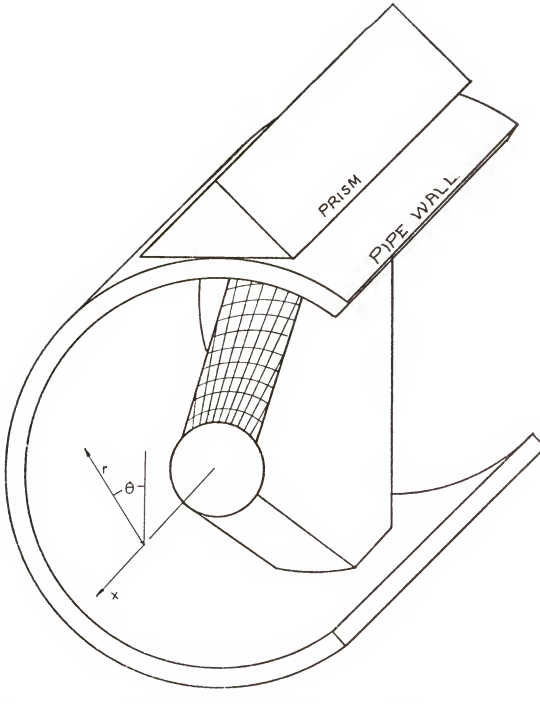

FIGURE 3.7 Grid placed in the pipe for calibration of the prism.

part of a straight conical surface. With the grid in place the pipe was filled with water and the grid photographed through the prism with exactly the same camera arrangement as used for the flow measurements.

The photograph was projected and copied on a piece of graph paper. Each of the grid points was identified in the two prism views on each frame. The co-ordinates of these grid points were read off from the graph sheet and used in equations (2.1) and (2.2) to predict the pipe positions (x, r, θ) of the grid points in the pipe. The predictions then could be compared with the known pipe positions of the grid points.

Computational Methods

Evaluation programs were written in Fortran IV and computations performed on an International Business Machines 370 housed at the Northeast Regional Data Center located at the University of Florida. For the purposes of this study the computer was used extensively to help evaluate the vast amount of data collected, involving some numerical techniques.

The experimental data collected from both the hot-film and trace-particle measurements on the turbulent flows needed to be processed in certain elementary ways in order to be useful. Numerical values had to be non-dimensionalized by the appropriate flow field quantities and put into suitable form for comparison.

The hot-film anemometer calibration curve relating hot-film output voltage to velocity was non-linear for velocities less than 31 mm/s. The following expressions were used to model the calibration: (see Chapter 4 for a detailed description of how they were derived)

$$U = -18.05\ E^2 + 47.2\ E + 1.25 \qquad 0 < E < 0.06$$

$$U = -1.69\ E^2 + 17.83\ E + 3.03 \qquad 0.06 \leq E \leq 0.59$$

$$U = -0.46\ E^2 + 15.44\ E + 3.72 \qquad 0.59 \leq E \leq 1.79$$

$$U = 12.76\ E + 7.05 \qquad 1.79 \leq E$$

where U = velocity; and E = voltage output of the x-probe.

The hot-film voltage outputs of the average velocities were substituted directly into the calibration equations to calculate the velocity U. For the root mean square (R.M.S.) measurements of the fluctuations, the slopes from the calibration curve were used to obtain the turbulence intensities. The resulting quantities were non-dimensionalized to the following forms: distance from the wall y/R and $y^* = u^*y/\nu$; average velocity $\overline{U}/\overline{U}_o$ and $U^+ = \overline{U}/u^*$; and turbulence intensities $u'/\overline{U}_o$, $v'/\overline{U}_o$, $w'/\overline{U}_o$, or u'/u^*, v'/u^*, w'/u^*. Here y = distance from the inner pipe wall; R = pipe radius; $\overline{U}$ = average axial velocity at some position y; $\overline{U}_o$ = average velocity at pipe center; ν = kinematic viscosity; $u^* = \text{wall friction velocity} = \sqrt{\nu \frac{\partial U}{\partial y}}$; u' = turbulence intensity = $\sqrt{\overline{u^2}}$; while u, v, and w are the fluctuating velocity components in the axial, radial and circumferential (azimuthal) directions, respectively.

For close wall positions where the boundary influenced the hot-film, an estimate of this effect was obtained from static measurements. Before each experimental run the hot-film was tranversed along a pipe diameter with the flow at rest. Near to the wall there was a negative signal. The negative signal was assumed to be due to the influence of the boundary (for lack of a better estimate) and was subsequently added to the near-wall measurements.

The temperature was kept nearly constant and change was jointly accounted for along with an output drift from probe contamination. In the cases where there was a drift over the seven hours it took for a complete experimental run, the drift was well monitored by the hourly centerline measurements. The hourly readings were plotted as $\overline{U}$ hourly/$\overline{U}_o$ against time, and the intermediate readings multiplied by the appropriate ratio. The ratio never fell below 0.94.

Checking the calibration analysis of the prism also required some computation. The photograph of the grid through the prism gave a set of prism co-ordinates for each of the grid points. These co-ordinate sets were made up of the three values: the distance of either image from the prism end x_B, the distance of the image in the positive prism face from the prism axis z_{B+}, and the distance of the image in the negative prism face from the prism axis z_{B-}. These three values were used in prism equations (2.1) and (2.2) to evaluate the co-ordinates (x_p, y_p, z_p) for each grid point.

The particle co-ordinates read from each frame of the cine film of the turbulence were used in the same way. For each particle in each frame the measurements x_B, z_B, and z_{B-} were used in equations (2.1) and (2.2) to obtain x_p, y_p, and z_p. The procedure was carried out frame by frame and by identifying a particle from one frame to the next, its change in position was calculated. In order to obtain the velocity three frames were considered, and the velocity at the mid-frame given by

$$U = (x_{p3} - x_{p1}) / (t_3 - t_1)$$

$$V = (r_{p3} - r_{p1}) / (t_3 - t_1)$$

$$W = r_{p2} (\theta_{p3} - \theta_{p1}) / (t_3 - t_1)$$

where U, V, and W are the instantaneous velocities in the axial, radial and circumferential directions, respectively; and (x_p, r_p, θ_p) is the particle position in cylindrical co-ordinates; while t_1, t_2, and t_3 are the instants at which the particle was in positions 1, 2, and 3. The use of three frames rather than two effectively approximates the particle path from time t_1 to time t_3 by the portion of a parabola.

There were always more than sixty particles in the studied flow region. Therefore, the velocity was always known at more than sixty points in the flow field. However, these positions were arbitrarily distributed throughout the region. In order to interpret the recorded data with some confidence the velocities were evaluated by two approaches. In the first approach the data were grouped in order to form averages. In the second approach an interpolation procedure was used to evaluate the velocities at a given set of positions in the flow field.

In order to formulate the averages, the flow region was divided into thin shell-like sections as shown in figure 3.6. Assuming that the averages in fully developed turbulent pipe flow show only a radial dependency, the values on each shell were summed for a spatial average. These spatial averages were then summed over time to obtain a combined space-time average. For the small volume viewed, and for the comparatively short time-record neither space nor time averages alone were complete, and therefore could not be compared. The average velocities $\overline{U}$, $\overline{V}$, $\overline{W}$ were computed, and then the intensities were evaluated as

$$u' = [\sum_{o}^{n} (U - \overline{U})^2_i]/n$$

where n = total number of measured velocity data utilized in the summation. Similar relationships are used for v' and w'.

The interpolation procedure required more computation. The flow field was divided into a lattice as is shown in figure 3.8. Then to find the interpolated velocity at each of the grid points (x_i, y_i, z_i) of the lattice, the velocities within a 4 mm radius were considered. Each velocity then made a contribution which was weighted according to its distance from the grid point. Thus, the grid point velocities were given by

$$U_i = \sum_1^n (U \cdot F)_i / \sum_1^n F$$

with similar expressions for V_i and W_i. Here n = number of points within 4 mm of the lattice point i, and F = the weighting factor. Initially, F was chosen as a linear function of distance

$$F = (4 - b)/4$$

where b = distance from lattice point to known-velocity point. This choice stemmed from the idea that the function F whould look something like the correlation function, where b would be approximately the macroscale of turbulence. With the linear choice of F it was hoped to get a first approximation to the velocities at the grid points. With these grid point velocities a first approximation of the correlation function was possible, which then would serve as an improvement for F. Computation time limited this procedure to a linear function of F.

For the positions closer than 4 mm to the boundary, the wall position (y = 0 and U = V = W = 0) was considered to contribute one velocity value just as any other particle would. Also, closer than 4 mm to the wall the sphere of interpolation is broken by the boundary. The correct way to counteract this would be to define a different function F. This was planned to automatically appear in the correlations after the first approximation. However, as this was not obtained, another procedure was

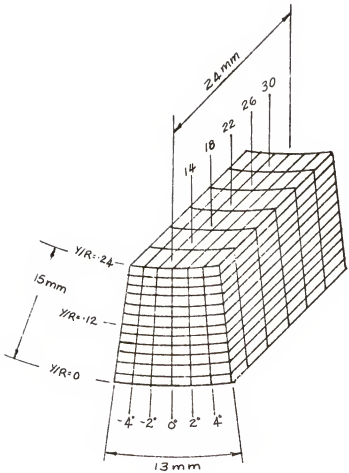

FIGURE 3.8 Lattice for interpolation of velocity.

adopted. For every velocity point (x_p, v_p, z_p) more than a distance y_i from the lattice point an equivalent velocity point of zero magnitude was placed at point (x_p, y_a, z_p) where $y_a = (y_i - y_p)$. The contribution of this point to the lattice point velocity was then weighted by $F = (4 - y_p)$.

With these restrictions the velocities were interpolated at the lattice points for each time frame giving both a space and time record of the velocity field. The computer programs used are given in Appendix B with some few explanations.

CHAPTER 4
FLOW STUDIES BY THE HOT-FILM ANEMOMETER

The results of the hot-film measurements presented in this chapter concern experiments made on fully developed turbulent flows at the outlet end of the 12.7 cm diameter pipe. The Thermo Systems, Inc. (T.S.I.) constant temperature hot-film anemometer arrangement described previously was used throughout. The experiments were performed prior to those described in the next chapter and do not attempt to measure the bursty nature of the region near the wall. They do include a calibration of the hot-film sensor to very low velocities, and extensive mean velocity and turbulence intensity measurements over the whole pipe diameter. As will be shown, the wall near measurements are not very reliable, and are difficult to interpret.

Calibration of the Hot-Film Anemometer

In order to be able to make velocity measurements close to a boundary in turbulent flow, it is essential to have an accurate and reliable calibration curve for the hot-film sensor. Preferably this calibration should also include the characteristic heat transfer effects of a nearby boundary and of the turbulent fluctuations. The calibrations described here cover a velocity range of 1.2 to 100 mm/s, and attempts are made to incorporate the boundary effects into the measurements. The calibrations are not done under non-steady or turbulent flow conditions.

The calibration values obtained by traversing the hot-film sensor along the vertical pipe diameter and integrating the resultant laminar profile are given in table 4.1. The average velocity, U_{ave}, is found from the flowmeter measurements of flow rate. The average voltage E_{ave} or hot-film output is calculated by the method of integration as described in Chapter 3. Assuming a parabolic horizontal profile

$$Q_E = \Sigma(A_p \Delta r)$$
$$= \Sigma \frac{2}{3} \cdot 2E \cdot \sqrt{R^2 - r^2}\, \Delta r$$

where A_p = area of a parabola with base $(4R^2 - 4r^2)^{\frac{1}{2}}$ and height E, and where R = pipe radius = 6.35 cm, r = radius to point of measurement, and Δr = increment in r between readings. The sample set of data for one such calibration value in table 4.2 shows this summation performed for r = 5.08 mm, R = 6.35 cm, and hot-film output values E.

$$Q_E = \Sigma \frac{2}{3} (40.323 - r^2)^{\frac{1}{2}} \cdot 2E$$
$$= \Sigma M\, 2E$$

For the example given in table 4.2, Q_E = 107.8, and therefore:

E_{ave} = Q_E divided by the cross sectional area of the pipe

= 0.864 volts

and the average velocity from measuring the flow rate is

U_{ave} = 16.5 mm/s

Very similar results were obtained for the calibration procedure in which the velocity profile at a sharp edged orifice is measured. The calibration values are shown in table 4.3, while table 4.4 shows a sample laminar velocity profile for the 61 mm diameter orifice. The flow is fairly uniform for the main portion of the diameter and the following summation is considered

TABLE 4.1 Calibration values obtained by integration of the hot-film outputs from laminar velocity profiles in the pipe.

U_{ave} mm/s	U/U_{20}	E_{ave} volts	E_{ave}/E_{20}
1.57	.079	.005	.005
1.59	.080	.005	.005
1.84	.092	.008	.008
1.97	.099	.015	.015
1.94	.097	.017	.016
2.13	.107	.022	.021
2.14	.107	.021	.020
2.44	.122	.026	.024
2.66	.133	.031	.029
3.14	.157	.023	.021
3.27	.164	.035	.033
3.91	.196	.043	.040
4.15	.208	.067	.063
4.47	.224	.070	.066
4.71	.236	.060	.057
5.14	.257	.098	.092
5.21	.260	.084	.079
5.33	.267	.110	.103
5.40	.270	.127	.120
5.77	.288	.152	.143
6.97	.348	.165	.155
7.12	.356	.159	.153
7.95	.398	.240	.226
8.40	.420	.326	.308
8.55	.428	.332	.312
10.52	.526	.337	.316
11.40	.570	.550	.518
11.68	.584	.460	.433
12.19	.609	.528	.496
12.70	.635	.578	.544
16.50	.825	.864	.813
17.36	.868	.863	.812
19.70	.985	1.04	.980
35.0	1.75	2.06	1.94
37.2	1.86	2.33	2.19
44.0	2.20	2.87	2.70
49.2	2.46	3.25	3.06
59.4	2.97	4.05	3.81
71.1	3.56	5.10	4.80
54.9	2.75	3.75	3.53
64.0	3.20	4.45	4.18
78.1	3.90	5.50	5.18

$U_{ave} = Q_m/A$ = measured flow rate/pipe area
$E_{ave} = Q_E/A$ = integrated hot-film output/pipe area
E_{20} = value of E_{ave} at U_{20} = 20 mm/s

TABLE 4.2 Sample laminar velocity profile for the pipe.

Position inches	Hot-film output E volts	Multiplier M	2•E•M
1.2	.12	.94	.22
1.4	.30	1.23	.74
1.6	.52	1.45	1.50
1.8	.78	1.62	2.54
2.0	1.00	1.75	3.50
2.2	1.22	1.86	4.54
2.4	1.42	1.95	5.54
2.6	1.59	2.02	6.42
2.8	1.72	2.07	7.10
3.0	1.78	2.11	7.50
3.2	1.80	2.13	7.68
3.4	1.80	2.15	7.74
3.6	1.78	2.14	7.60
3.8	1.76	2.13	7.50
4.0	1.74	2.10	7.30
4.2	1.66	2.05	6.80
4.4	1.56	2.00	6.24
4.6	1.42	1.92	5.46
4.8	1.24	1.81	4.48
5.0	1.06	1.69	3.58
5.2	.84	1.54	2.58
5.4	.58	1.35	1.56
5.6	.30	1.10	.66
			107.78

TABLE 4.3 Calibration values obtained by integration of the hot-film outputs from laminar velocity profiles in the orifice.

U_{ave} mm/s	U/U_{20}	E_{ave} volts	E_{ave}/E_{20}
5.20	.260	.109	.122
6.65	.333	.168	.188
8.10	.405	.196	.219
3.12	.156	.023	.026
5.82	.291	.130	.145
8.72	.436	.262	.293
12.2	.61	.373	.416
18.0	.90	.705	.79
22.1	1.11	.99	1.11
23.5	1.18	1.06	1.18
25.7	1.29	1.37	1.53
32.5	1.63	2.01	2.24
46.2	2.31	3.15	3.52
11.3	.57	.31	.51
18.7	.94	.56	.92
15.7	.79	.44	.71
33.5	1.68	1.12	1.84
53.6	2.68	2.03	3.34

TABLE 4.4 Sample laminar velocity profile for the orifice.

Position inches	Hot-film output E volts	E•r	$\pi\Delta r(E \cdot r)$
2.0	zero	zero	zero
2.2	zero	zero	zero
2.4	.74	.78	3.15
2.6	1.79	1.52	6.14
2.8	1.82	1.18	4.76
3.0	1.84	.83	3.35
3.2	1.83	.46	1.86
3.4	1.84	.09	.36
3.6	1.86	.28	1.13
3.8	1.90	.67	2.71
4.0	1.97	1.08	4.36
4.2	2.03	1.52	6.15
4.4	2.13	2.01	8.10
4.6	0.19	.22	.89
4.8	zero	zero	
5.0	zero	zero	
	total =	10.64	

Pipe center at position = 3.5

$$Q_E = \Sigma\ (A_c\ \Delta r)$$

$$= \Sigma_{2r}\ \pi r E \Delta r$$

where A_c = the area of a cylindrical shell of height E and radius r.

For the example considered $Q_E = 10.6\ \pi\Delta r = 43.0\ cm^2V$

E_{ave} = Q_E divided by the cross sectional area of the orifice

= 1.37 volts

while U_{ave} = 25.7 mm/s.

Neither of these techniques of averaging the values over the pipe nor over the orifice, is entirely satisfactory because they involve a range of values over which the calibration is not linear (see figure 4.4). However, the similarity in the results, shown later in figure 4.4, indicates some agreement with the true calibration curve. The two techniques differ quite sharply as to which of the hot-film outputs contribute most heavily to the evaluation of E_{ave}. Figure 4.1 shows the values of the terms contributing to Q_E for the orifice (E·r) and the pipe (2·E·M), respectively. It is noticed that, for the pipe flow, the measurements over the whole central region contribute fairly evenly whereas for the orifice the center contribution is zero. The different assumptions as to the shape of the horizontal velocity-profile are somewhat questionable. However, the final calibration curves are in good agreement with each other.

The data from the pipe flow calibrations are used in a curve fitting procedure. The values are plotted as shown in figure 4.2 and the best fitting straight line U = 12.76 E + 7.05 drawn through the data points within the higher velocity range. The straight line is a least squares fit to the data with U > 30 mm/s. For the values of U < 30 mm/s

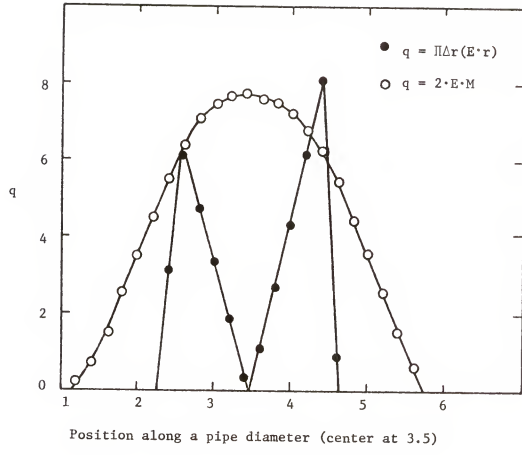

FIGURE 4.1 Distribution of summation terms q for the orifice, $q = \Pi\Delta r(E \cdot r)$, and for the pipe, $q = 2 \cdot E \cdot M$.

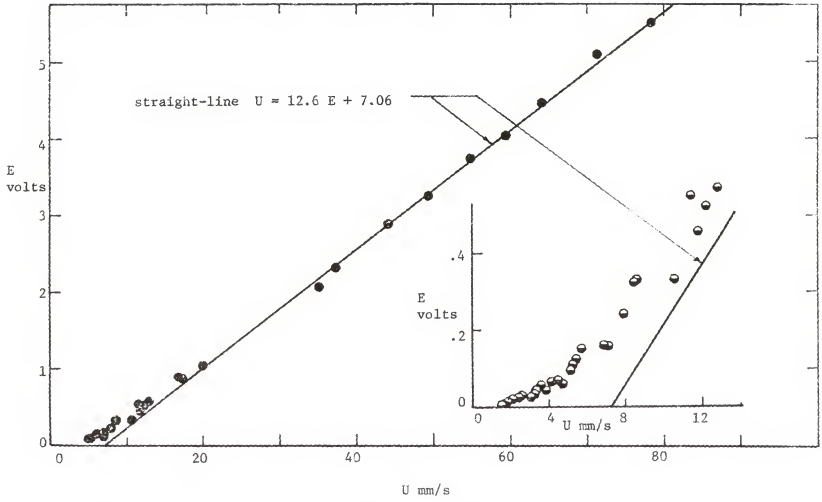

FIGURE 4.2 Hot-film calibration values measured in the pipe.

there is a significant deviation from the linear relationship. This deviation is plotted in figure 4.3 as the difference ΔU between the straight line and actual values of U, against the difference $\Delta E = (1.79 - E)$ between the voltage at 30 mm/s and the actual voltage. The resulting plot is approximated by the straight line sections

$$E = 0.0554\ \Delta U/\Delta E + 1.61 \qquad 0 < E < 0.6$$

$$E = 0.535\ \Delta U/\Delta E + 0.59 \qquad 0.6 \leq E < 0.59$$

$$E = 2.20\ \Delta U/\Delta E - 2.3 \qquad 0.59 \leq E < 1.79$$

Solving these for ΔU and adding them to the straight line $U = 12.76E + 7.05$ yields the calibration curve over the whole range

$$U = + 12.76E + 7.05 \qquad E \geq 1.79$$

$$U = .46\ E^2 + 15.44E + 3.72 \qquad 1.79 > E \geq 0.59$$

$$U = -1.69\ E^2 + 17.83 + 3.03 \qquad 0.59 > E \geq 0.06$$

$$U = -18.05\ E^2 + 47.26E + 1.25 \qquad 0.06 > E > 0$$

The calibration curve is then made up of a collection of parabolas. It may be noted that neither a least square fit of a quadratic or cubic expression was able to fit the values very satisfactorily.

The hot-film calibration curve is also determined by timing the motion of minute particles as described in Chapter 3. Table 4.5 contains these calibrations made by the trace-particle visualization technique illustrated in figure 3.2. The results for the three methods recorded in tables 4.1, 4.3, and 4.5 are plotted in figure 4.4. The data are normalized with respect to a velocity of 20 mm/s in order to be directly comparable with one another. Also drawn in figure 4.4 is the calibration curve fitted to the integrated data of the flow cross section.

The calibration data from the orifice and pipe flows, and from trace-particle visualization of the flow agree well with each other.

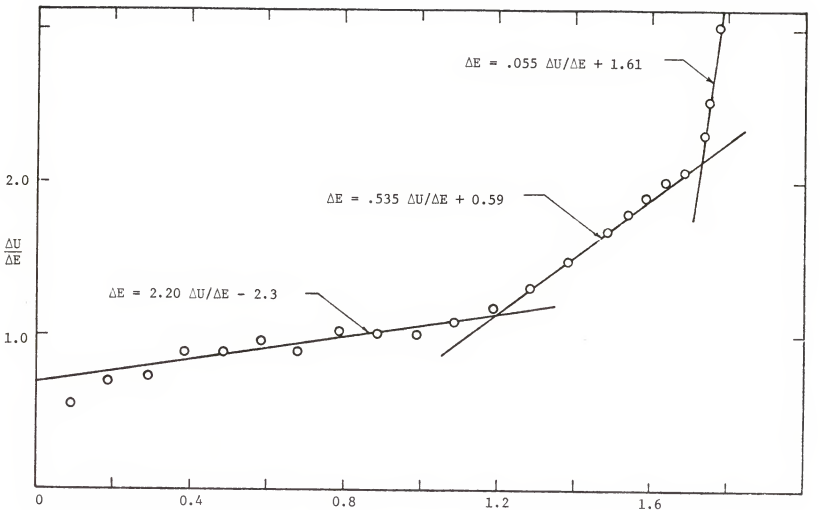

FIGURE 4.3 Approximations to the calibration curve.

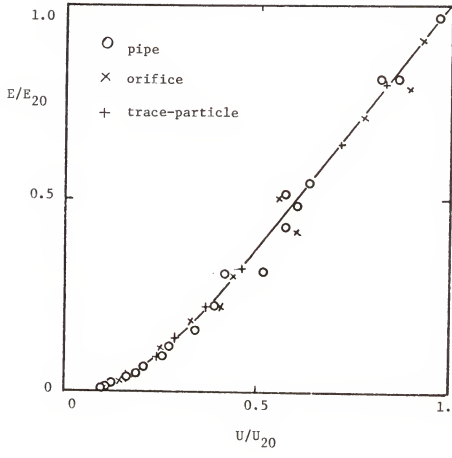

FIGURE 4.4 Calibration curve for the hot-film sensor.

TABLE 4.5 Calibration of the hot-film anemometer by timing the motion of minute particles in the flow.

U_{ave} mm/s	U_{ave}/U_{20}	E_{ave} volts	E_{ave}/E_{20}
3.9	.195	.036	.055
1.57	.078	zero	zero
3.14	.157	.024	.037
3.39	.169	.029	.045
2.45	.123	.010	.015
4.85	.243	.064	.099
5.35	.268	.080	.123
8.68	.434	.19	.29
5.78	.289	.086	.13
7.39	.369	.144	.22
9.32	.466	.21	.32
12.0	.60	.32	.49
14.5	.73	.42	.65
16.8	.84	.56	.80
20.5	1.03	.71	1.09
23.3	1.17	.78	1.20
21.8	1.09	.73	1.12
27.0	1.35	.82	1.26
18.4	.92	.57	.88
8.04	.402	.12	.184
3.32	.166	.024	.037
3.64	.182	.05	.047
4.79	.239	.10	.093
6.52	.326	.20	.186
8.22	.411	.30	.279
11.51	.58	.50	.466
12.81	.64	.60	.559
18.70	.94	1.00	.93

For the higher velocity range the hot-film output is well represented by a linear relation of the flow velocity. There is a lower limit, U = 1.4 mm/s below which the hot-film does not respond to the flow velocity. This limit depends somewhat on the overheat ratio used for the hot-film, and indicates a dominance of free convectional heat transfer over forced. This feature is not all that unexpected when the free convection velocity U_f is included in the analysis. A typical hot-film configuration is shown in figure 4.5, and if the free convection velocity U_f is greater than the flow velocity U, then the hot-film output, A + B, from the two sensors A and B of the x-probe, will be

$$(A + B) = \text{constant } [(U_f + v - U - u) \cos 45° + (U_f + v + U + u)\sin 45°]$$
$$= \text{constant } \sqrt{2}\,(U_f + v)$$

under which circumstances the output should be independent of U.

The effect of the boundary upon the calibration values is noticeable only when the probe is located near the boundary. Figure 4.6 shows the hot-film output for the probe in positions close to the wall and for different flow velocities. From the curve for zero flow it can be seen that the apparent negative effect of the hot-film response is noticeable for positions closer to the wall than 10 mm. The boundary has the effect of reducing the total heat loss from the hot-film. Whether the reduced loss is due to restricted free convection or possibly due to the heat reflection by the boundary is not clear. These readings were taken at the upper inner surface of the pipe by a single sensor hot-film probe. Readings at the bottom inner surface showed similar effects only not so pronounced, implying that some of these effects, but not all, are due to free convection. Conduction of heat towards the boundary may also be

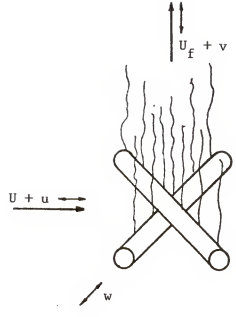

FIGURE 4.5 Hot-film sensor showing free convection.

present because of the difference between the specific heat of the wall and that of the water.

One disturbing feature of the graphs in figure 4.6 is the observation that the readings within 1 mm of the boundary do not discriminate between flows of different lower flow rates and hence velocity differences. This insensitivity is not detected for measurements within the same region near the wall at higher Reynolds number, turbulent flows, but its existence at low Reynolds numbers remove any confidence in the interpretation of near-wall readings. Close to the boundary there is an additional problem with the x-probe, due to its size. For measurements performed outside the outlet end of the pipe parts of the probe are shielded from the primary flow field when its radial distance from the pipe wall is less than 1.4 mm.

The combination of poor low velocity response, uncertain boundary effects and geometric constraints make it clear that the hot-film sensor is not suited to measurements in the immediate boundary zone. Therefore, although turbulence measurements are made all the way to the wall, values taken closer to the wall than 1.5 mm (or $y/R = 0.025$) should not be considered reliable. In the present experiments the thickness of the viscous sublayer would be 2.3, 3.0, and 4.9 mm for flows of Reynolds numbers 9,000, 6,500, and 4,000, respectively. It should also be noted that the calibrations performed here are for laminar flow conditions, i.e., "static" calibrations. As Perry & Morrison (1971b) clearly show, there may be a considerable difference between static and dynamic calibrations. Dynamic calibration measurements are made under fluctuating or unsteady flow conditions and are thus more suited to turbulent flows.

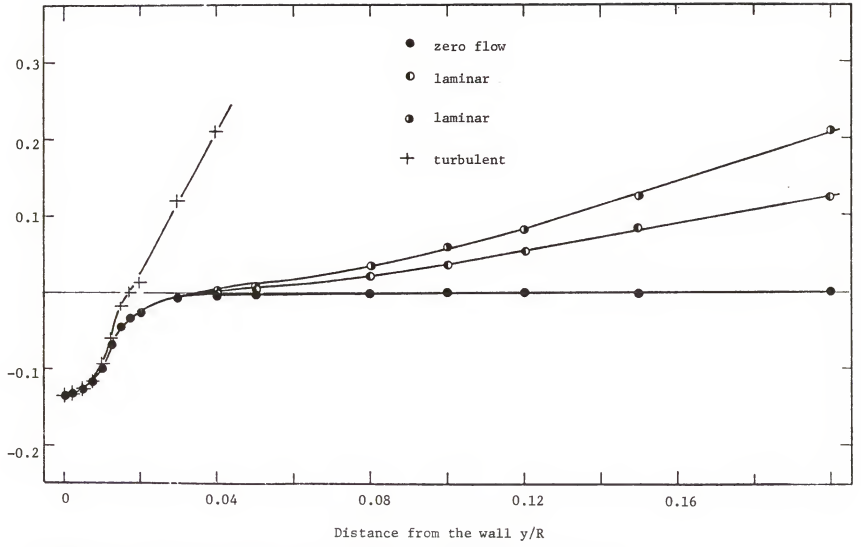

FIGURE 4.6 Hot-film response in the immediate neighborhood of the wall.

Hot-Film Turbulence Measurements

Turbulence measurements were made with the hot-film sensor at the outlet end of the 0.127 m diameter, 23.6 m long pipe described in Chapter 3. The probes used are the T.S.I. model 1241 - 10W cross-film probes mounted on the pipe-traversing mechanism. The probe location is determined by its radial position y from the pipe wall, and its distance d_o from the pipe-outlet plane. The distance d_o is defined to be positive for positions outside the pipe, and negative for positions inside. The axial velocity component is measured for every data point, together with one of either the radial or circumferential velocity components, as determined by the probe orientation.

Table 4.6 gives a summary of the sets of measurements made. The Reynolds number, $Re = \overline{U}D/\nu$, is based on the average pipe velocity calculated from the flow rate. Each set of measurements was done for a constant value of d_o and for a specified probe orientation as indicated in table 4.6. A sample set of data obtained at a Reynolds number of 6,500 for one value of d_o is shown in table 4.7.

By traversing the probe outside of the pipe end it is possible to make measurements all the way out to the boundary, but with the disadvantage of experiencing the effects of the jet diffusion characteristics. The jet diffusion should decrease with decreasing distance d_o, and it was hoped that the data obtained at different d_o values could be extrapolated to $d_o = 0$, as was done by Lindgren & Chao (1969). The results of the mean forward velocity profiles given in figures 4.7 through 4.9 show, however, that there is no clear trend to be extrapolated in the variation with d_o. The success with which Lindgren & Chao (1969) employed the extrapolation technique may lie in their use of single sensor probes

TABLE 4.6 Summary of measurements made with the hot-film anemometer.

Run name	Reynolds number	Probe orientation	Probe position d_o	Plotting symbol
Jan 20	9000	radial	2.3	○
Jan 22	6500	radial	2.3	○
Jan 18	4000	radial	2.3	○
Feb 19	9000	radial	1.4	◑
Feb 20	6500	radial	1.4	◑
Feb 16	4000	radial	1.4	◑
Feb 15	9000	radial	-2.6	+
Feb 15	6500	radial	-2.6	+
Feb 15	4000	radial	-2.6	+
Jan 25	9000	circum.	2.6	●
Jan 23	6500	circum.	2.6	●
Jan 24	4000	circum.	2.6	●
Feb 1	9000	circum.	1.3	◐
Jan 27	6500	circum.	1.3	◐
Jan 30	4000	circum.	1.3	◐
Feb 12	9000	circum.	-1.8	×
Feb 13	6500	circum.	-1.8	×
Feb 3	4000	circum.	-1.8	×

TABLE 4.7 Sample set of velocity data measured with the hot-film anemometer for a Reynolds number of 6,500 and a distance d_o = 1.4 mm.

y/R	$\overline{U}/U_o$	$u'/\overline{U}_o$	$v'/\overline{U}_o$
1.000	1.00	0.036	0.029
0.050	0.50	0.124	0.020
0.120	0.72	0.093	0.031
0.150	0.76	0.085	0.032
0.015	0.17	0.052	0.024
0.010	0.13	0.030	0.015
0.080	0.64	0.111	0.024
1.000	1.00		
0.013	0.15	0.037	0.019
0.005	0.10	0.018	0.010
0.030	0.31	0.101	0.021
0.020	0.21	0.074	0.024
0.100	0.67	0.106	0.025
0.040	0.41	0.113	0.016
1.000	1.00		
0.035	0.79	0.096	0.018
0.0	0.07	0.016	0.011
0.200	0.80	0.076	0.036
0.060	0.56	0.105	0.021
0.045	0.44	0.114	0.021
0.018	0.20	0.068	0.026
0.025	0.28	0.084	0.023
1.000	1.00	0.035	0.028

and consequently smaller values for d_o. The geometric size of the cross probe used here excluded readings for $d_o < 1.2$ mm, and $y < 2.0$ mm.

The mean velocities are plotted in figures 4.7, 4.8, and 4.9, in co-ordinates of the universal logarithmic velocity profile. The variables are expressed in terms of wall-friction velocity u^*. By definition $u^* = \sqrt{\nu \frac{\partial \bar{U}}{\partial y}}$ where y = radial distance from the wall, and $\bar{U}$ = local axial velocity. The velocity ratio is defined as $u^+ = \bar{U}/u^*$, and the distance parameter is defined as $y^+ = u^* y/\nu$. The curves for $u^+ = y^+$ and $u^+ = 5.5 + 2.5 \ln y^+ = 5.5 + 5.75 \log_{10} y^+$ are shown for reference. For very small y^+ values the experimental data for each of the Reynolds numbers show a deviation from the curve $u^+ = y^+$. This, however, is the region where the boundary effects and hot-film performance are at their worst. Microscope measurements presented later, probe the zone $y^+ < 3$ more effectively.

An interesting feature seen in figures 4.7, 4.8, and 4.9 is the variation of velocity with Reynolds number in the "wall region", the wall region being located outside the viscous sublayer, but not extending into the core-region. Townsend (1956) indicates that for lower Reynolds numbers the mean-velocity distribution changes with the Reynolds number, but that the variation is negligibly small. For the results shown here the variation is quite sizeable, in fact for Re = 4,000 it seems quite different from the universal logarithmic velocity distribution. Townsend (1956) also showed that the outer region in boundary flow became smaller with lower Reynolds number. The same effect should be expected for the core region in pipe turbulence. The curve for Re = 9,000 shows little or no apparent core region.

The turbulence intensity measurements for the three velocity components are shown in figure 4.10 through 4.21. The data show considerable scatter, especially for positions close to the boundary. The scatter is noticeably greater for flows at a lower Reynolds number and the variations seem to be larger than would be expected in a statistical description of turbulent velocity fluctuations. Although quite random in occurrence, there appear certain distinct sets of violent motions of highly variable events, which take place particularly in the wall region. Long time averaging over these events not only serves to obscure them but translates their importance into apparent scatter. Experimental observations reported in the next chapter will enhance such interpretations and will explain events giving rise to the scatter of the hot-film measurements at low Reynolds numbers.

Measurements of mean velocity profiles and turbulence intensity distributions are summarized in figures 4.22 through 4.26. The curves for the different Reynolds numbers are drawn to best fit the data points plotted in figures 4.7 through 4.21. A variation in the shape of the mean velocity profile with Reynolds number is seen in figure 4.22. It is known that universal velocity distributions and universal shear stress distributions have not been attained simultaneously for turbulent boundary layer flows. Clauser (1956), however, concluded that the dissimilarity was small and could mostly be neglected. From the results presented here it is clear that, at least within low Reynolds number ranges, this variation is neither small nor negligible. The differences may be very important in analyzing the continuity of the mechanisms involved in the transition and self-preserving processes in turbulence.

Possibly another important "self-preserving" criterion is seen in the variation of the radial turbulence intensity v' profile near the boundary. The peak so clearly defined for the higher Reynolds number flows is hardly detectable for Re = 4,000, at which Re value the slight peak has moved well away from the wall. The Reynolds number at which this peak disappears altogether may be related to the critical Reynolds number for self-preservation of turbulence. The axial turbulence intensity u' also shows a peak which moves toward the boundary with higher Reynolds number as may be expected. The peak in the circumferential turbulence intensity w' shows a smaller, but similar shift.

In the hot-film turbulence measurements presented, uncertainties in calibrations and measurements are recognized. The boundary effects are recognized in the same way, and for that reason no interpretations are made for readings closer to the boundary than 2 mm. The measurements, however, do give information about fully developed turbulent pipe flows of water at low Reynolds numbers, where turbulence characteristics are difficult to measure in average, but should be clearer in detail. The long time averaged hot-film measurements do not supply insight into the detailed mechanisms involved and do not describe the structure satisfactorily. The detailed structure is studied by the trace-particle technique, the results of which are reported in Chapter 5. In order to settle the question of the shape of the mean velocity profile for positions closer to the wall than 1 mm, microscope studies described in Chapter 3 are presented next, supplementing results already presented.

Measurements With a Microscope

The experimental arrangement for the microscope studies are described in Chapter 3. The data from these measurements are given in tables 4.8, 4.9, and 4.10 and then plotted in figures 4.27, 4.28, and 4.29. At all three Reynolds numbers, certain features seem clear. There is no evidence of slip at the wall. The profile in the immediate neighborhood of the wall appears linear. The hot-film data differ quite markedly from those of the microscope measurements at distances less than 1 mm from the boundary, but match well both in value and slope outside of the 1 mm zone. The matching occurs at slightly different positions for the different Reynolds numbers.

The accuracy of the microscope measurements is limited by the focusing depth on the microscope (0.03 mm), the field of view (5.5 mm), and the stopwatch time scale (0.1 s). Even with these limitations the simple microscope technique is quite useful and the conclusions presented appear reliable. Fluctuations in the velocity were observed even in positions in the immediate neighborhood of the wall, confirming the observations of Fage & Townend (1932). No estimate has been made of the strength of fluctuations observed by means of the microscope.

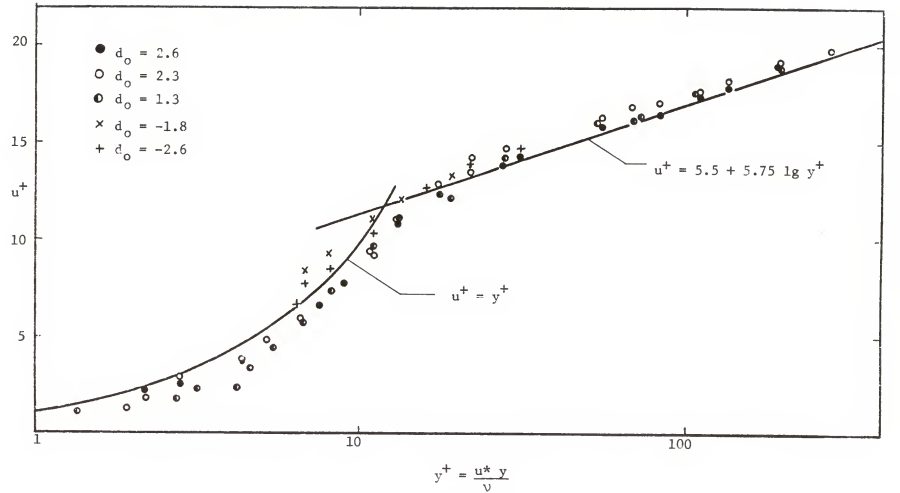

FIGURE 4.7 Mean-velocity distribution for a flow of Reynolds number 9,000.

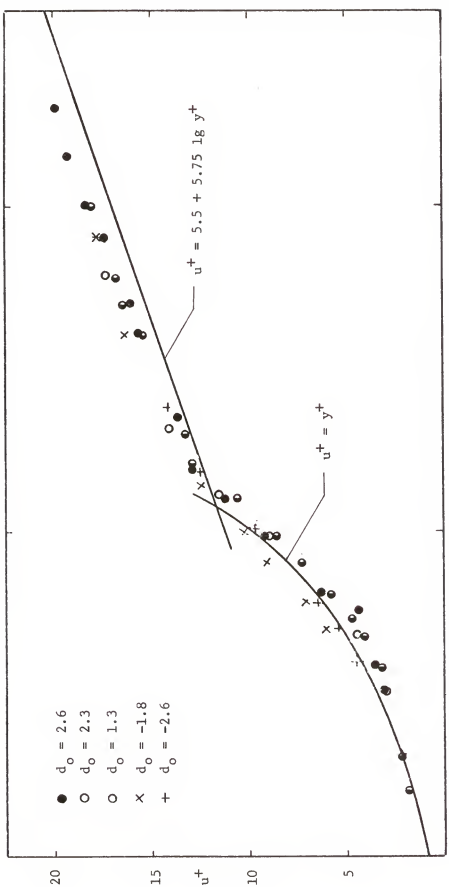

FIGURE 4.8 Mean-velocity distribution for a flow of Reynolds number 6,500.

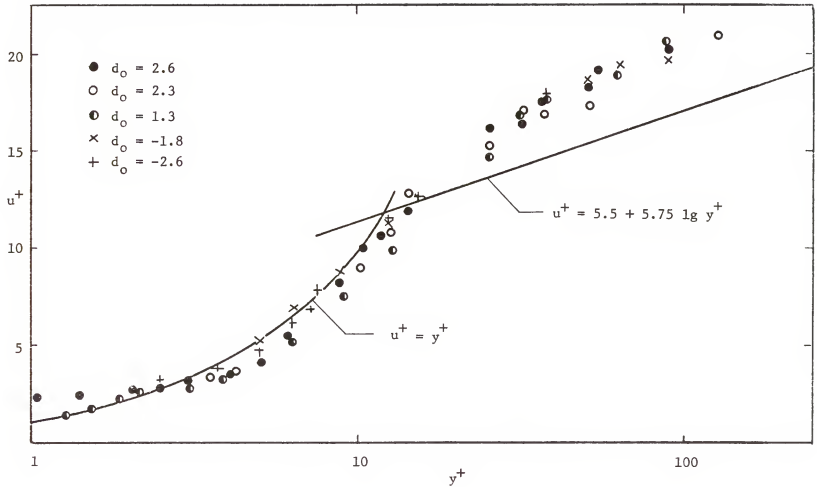

FIGURE 4.9 Mean-velocity profile for a flow of Reynolds number 4,000.

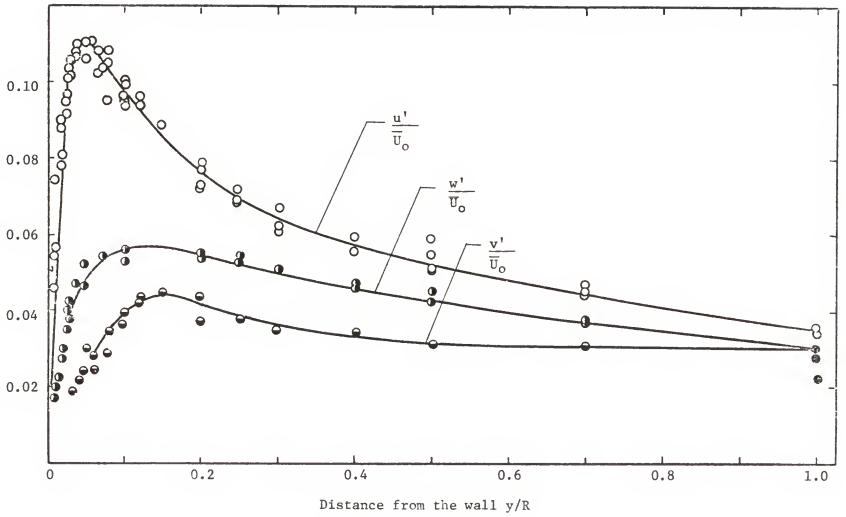

FIGURE 4.10 Relative turbulence intensities for a flow of Reynolds number 9,000.

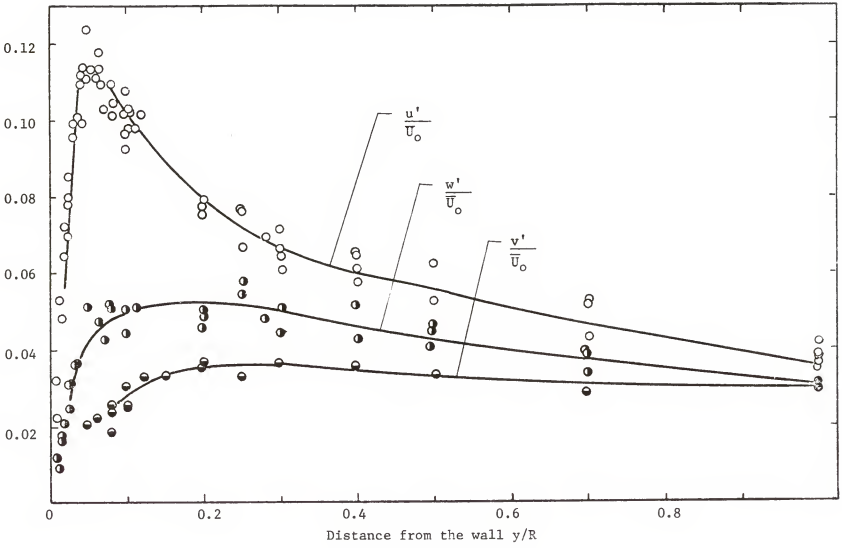

FIGURE 4.11 Relative turbulence intensities for a flow of Reynolds number 6,500.

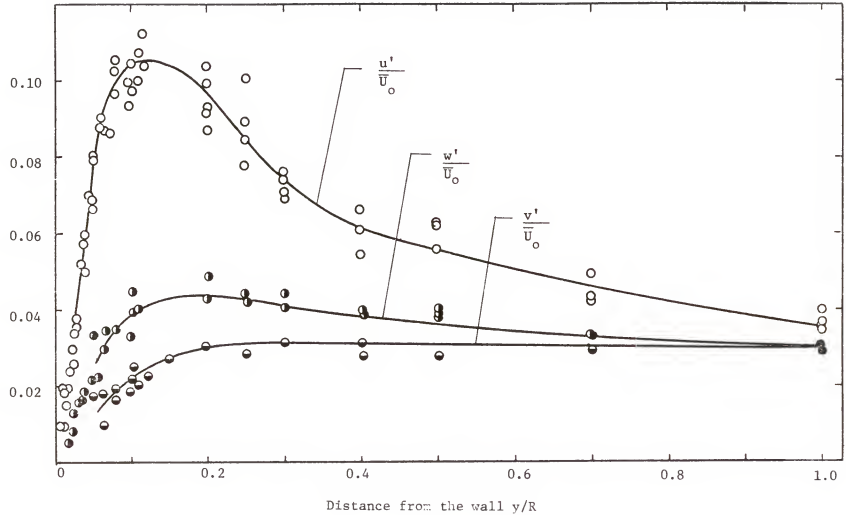

FIGURE 4.12 Relative turbulence intensities for a flow of Reynolds number 4,000.

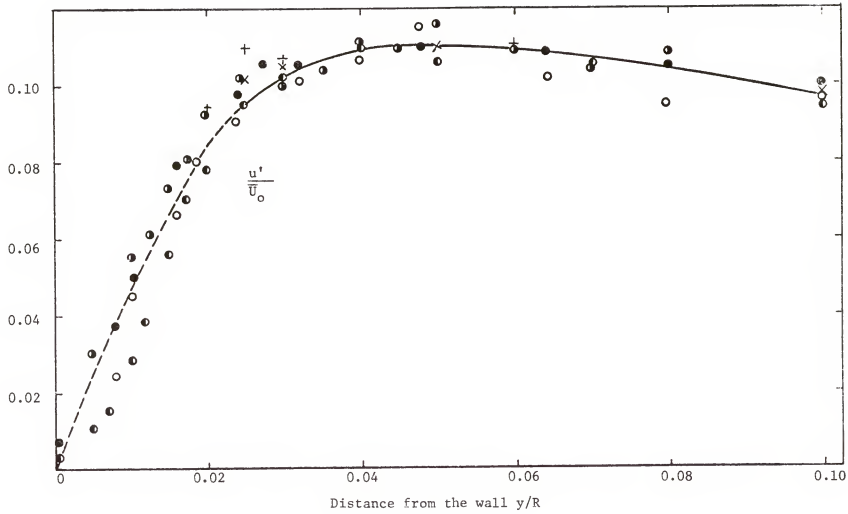

FIGURE 4.13 Axial turbulence intensity for a flow of Reynolds number 9,000.

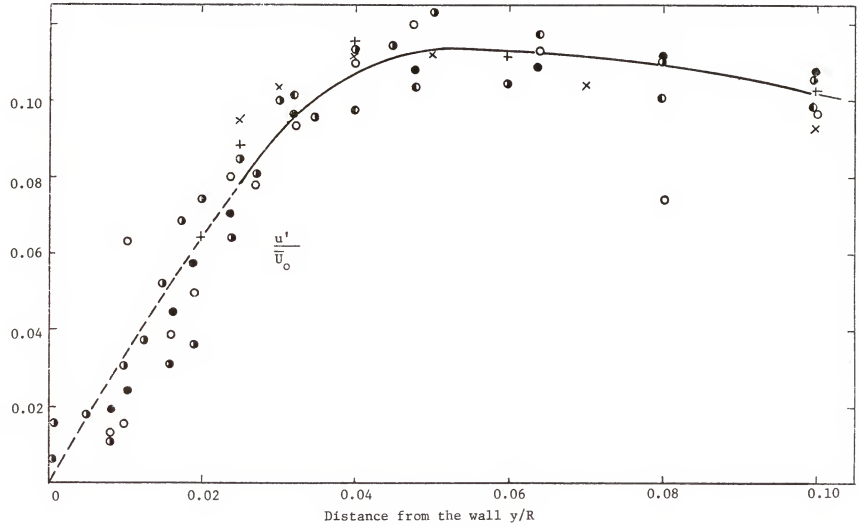

FIGURE 4.14 Axial turbulence intensity for a flow of Reynolds number 6,500.

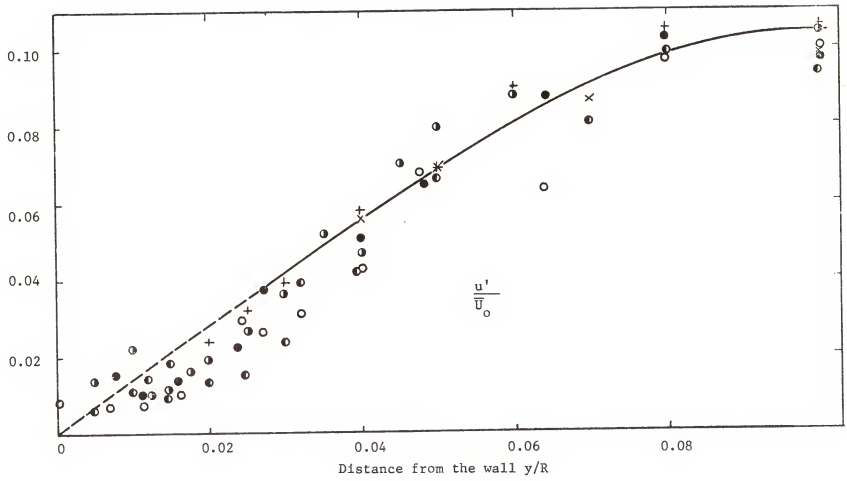

FIGURE 4.15 Axial turbulence intensity for a flow of Reynolds number 4,000.

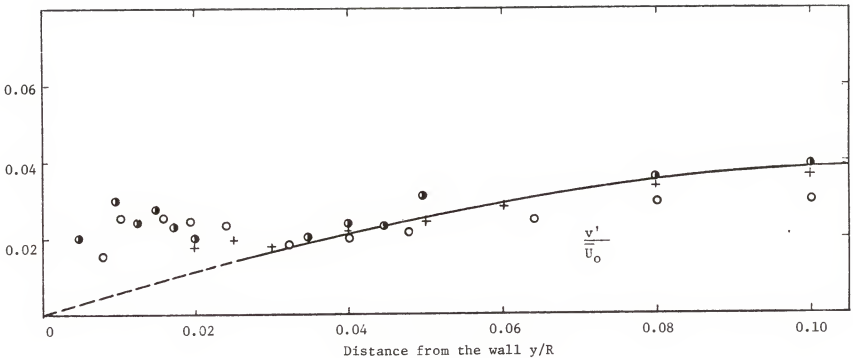

FIGURE 4.16 Radial turbulence intensity for a flow of Reynolds number 9,000.

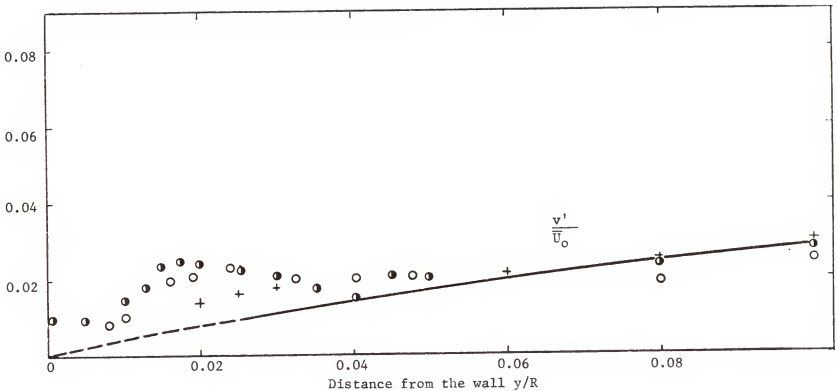

FIGURE 4.17 Radial turbulence intensity for a flow of Reynolds number 6,500.

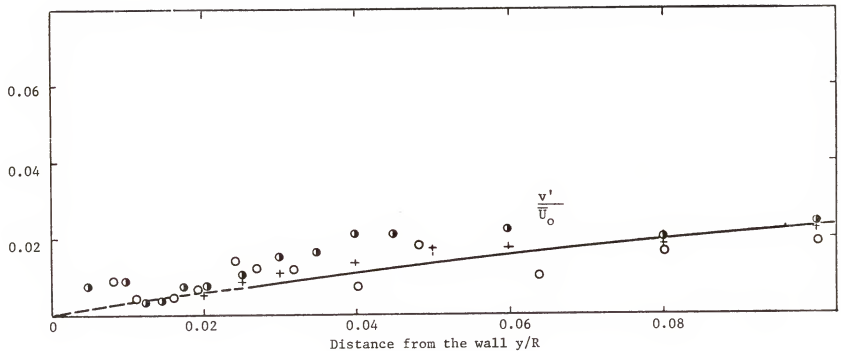

FIGURE 4.18 Radial turbulence intensity for a flow of Reynolds number 4,000.

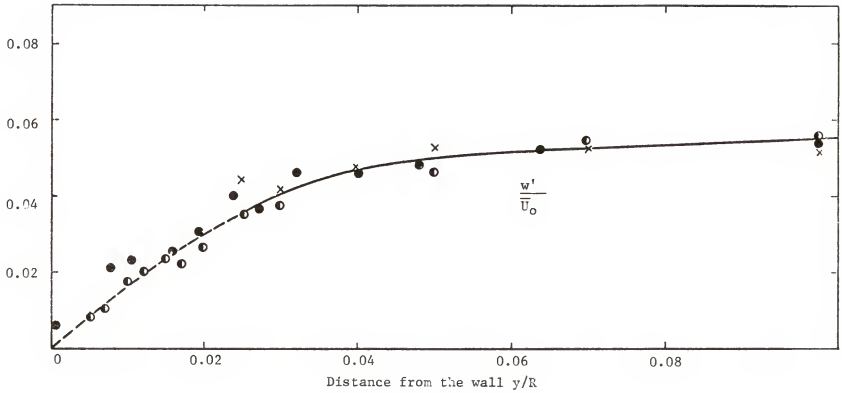

FIGURE 4.19 Circumferential turbulence intensity for a flow of Reynolds number 9,000.

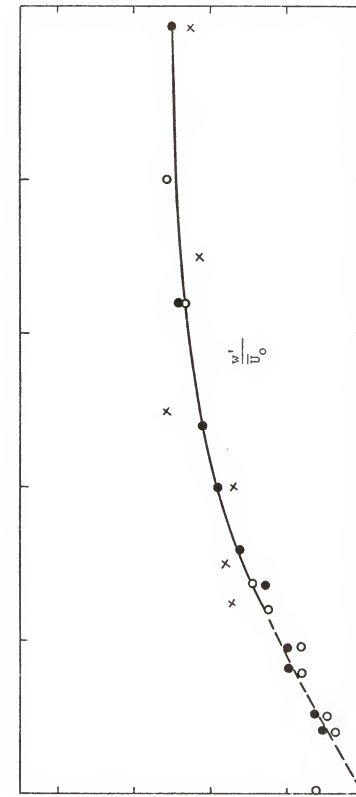

FIGURE 4.20 Circumferential turbulence intensity for a flow of Reynolds number 6,500.

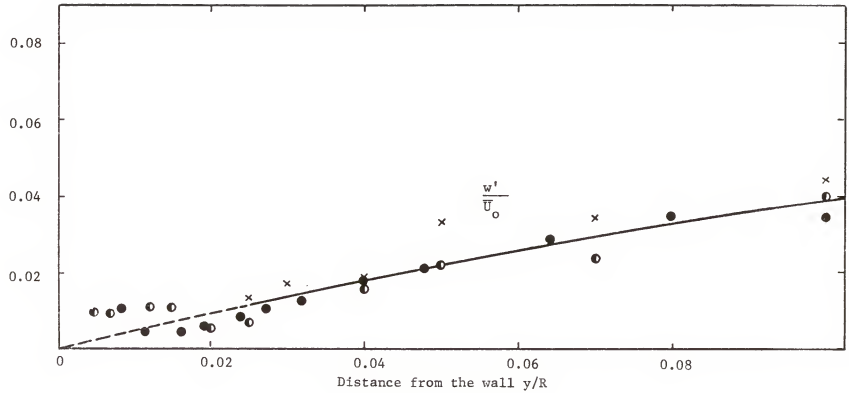

FIGURE 4.21 Circumferential turbulence intensity for a Reynolds number of 4,000.

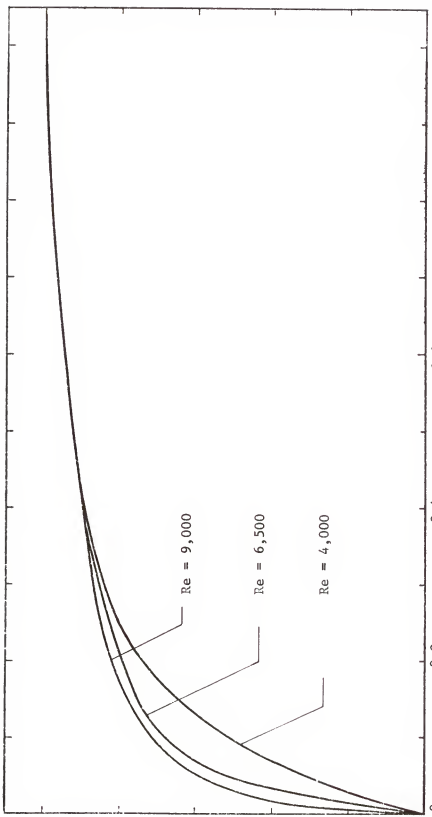

FIGURE 4.22 Summary of the mean-velocity profiles.

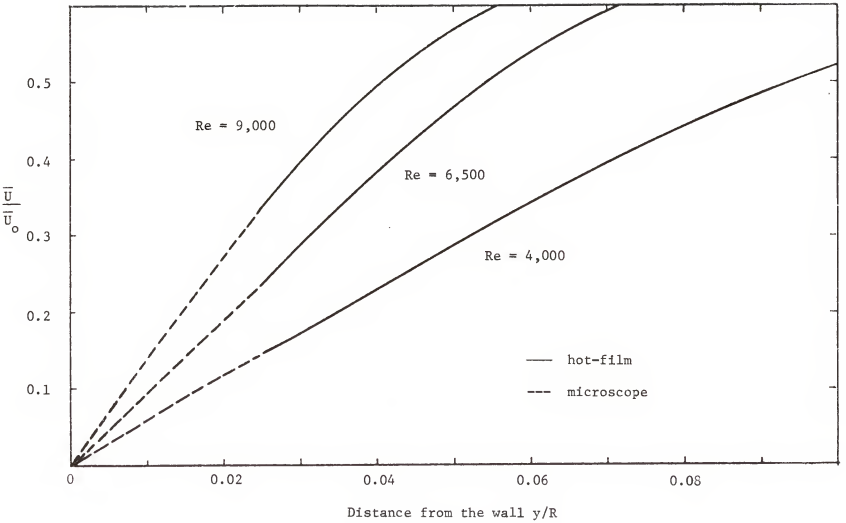

FIGURE 4.23 Summary of mean-velocity profiles in the wall region.

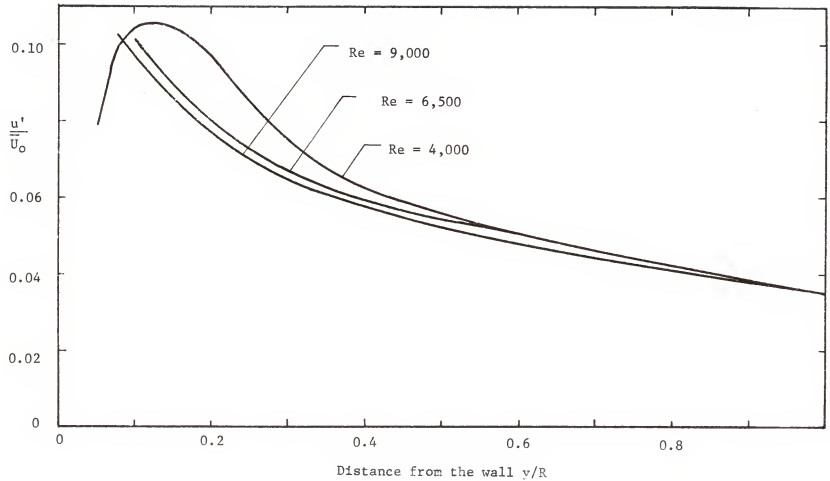

FIGURE 4.24 Summary of the axial turbulence intensity profiles.

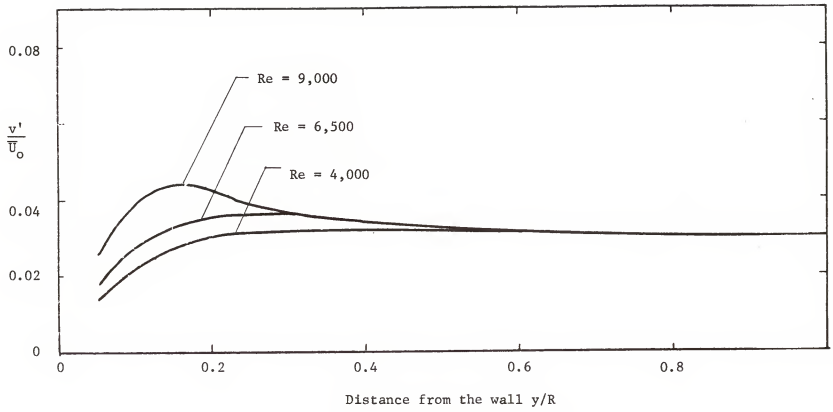

FIGURE 4.25 Summary of the radial turbulence intensity profiles.

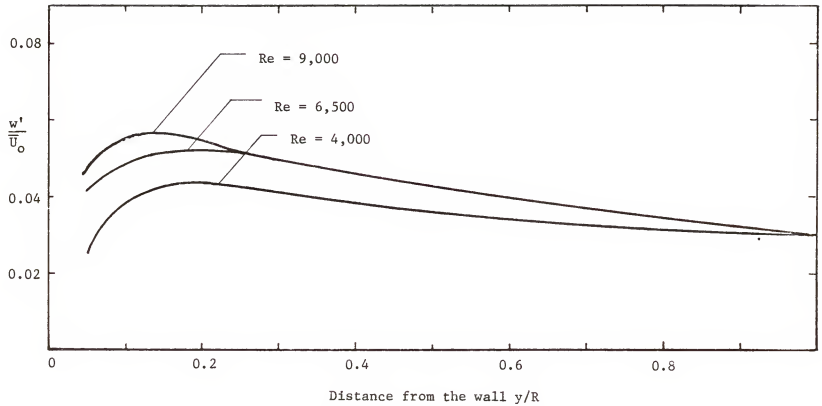

FIGURE 4.26 Summary of the circumferential turbulence intensity profiles.

TABLE 4.8 Microscope measurements at a Reynolds number of 9,000.

Microscope position turn	Particle position y/R	Velocity ratio $\overline{U}/\overline{U}_o$
1/8	.0013	.013
1/4	.0027	.034
3/8	.0040	.052
1/2	.0054	.068
5/8	.0067	.085
3/4	.0080	.097
1	.0107	.136

TABLE 4.9 Microscope measurements at a Reynolds number of 6,500.

Microscope position turn	Particle position y/R	Velocity ratio $\overline{U}/\overline{U}_o$
1/16	.0006	.004
1/8	.0013	.010
1/4	.0027	.019
3/8	.0040	.039
1/2	.0054	.052
3/4	.0080	.078
7/8	.0094	.089
1	.0107	.103

TABLE 4.10 Microscope measurements at a Reynolds number of 4,000.

Microscope position turn	Particle position y mm	Particle position y/R	Velocity ratio $\overline{U}/U_o$
1/8	.085	.0013	.006
1/4	.17	.0027	.014
1/2	.34	.0054	.033
1	.68	.0107	.052
1 1/4	.846	.0133	.080
1 1/2	1.02	.0161	.089
1 1/2	1.02	.0161	.089
1 3/4	1.19	.0187	.103
2	1.36	.0214	.130
2	1.36	.0214	.120

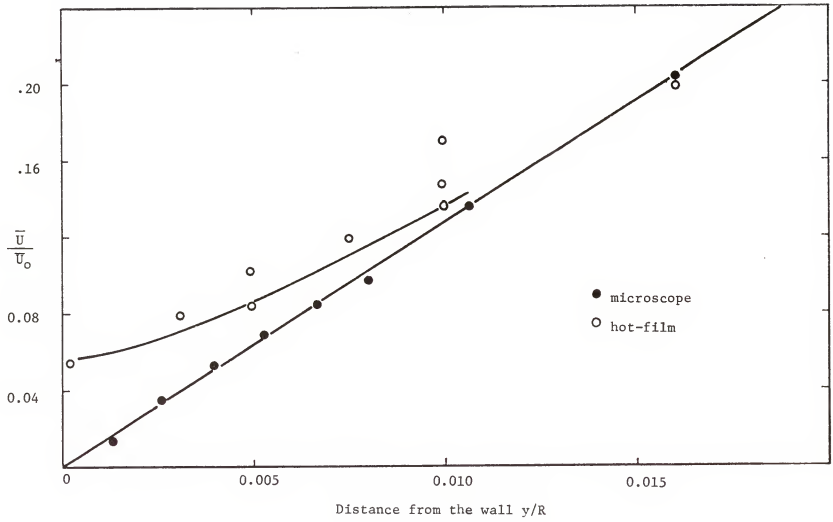

FIGURE 4.27 Microscope measurement of the mean velocity profile for a flow of Reynolds number 9,000.

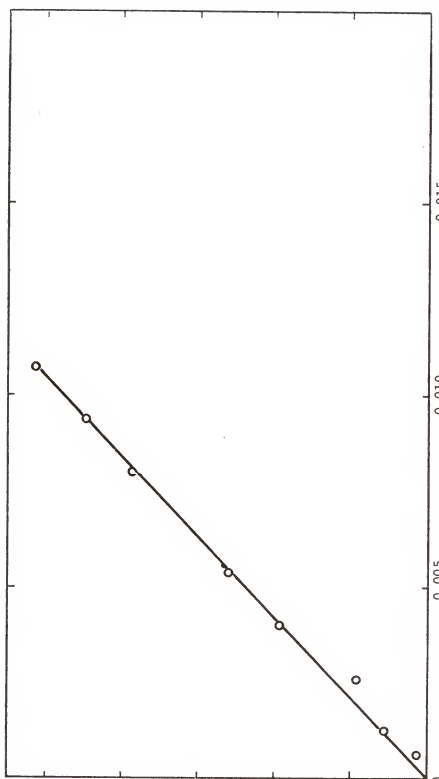

FIGURE 4.28 Microscope measurement of the mean velocity profile for a flow of Reynolds number 6,500.

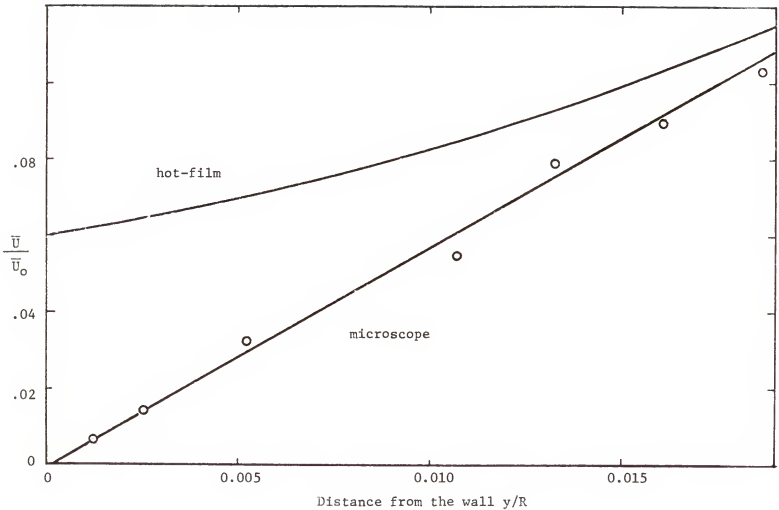

FIGURE 4.29 Microscope measurement of the mean velocity profile for a flow of Reynolds number 4,000.

CHAPTER 5
FLOW STUDIES BY THE PRISM, TRACE-PARTICLE METHOD

Flow visualization by trace particles has on several occasions proven both an informative and convenient tool for obtaining qualitative measurements. For steady flows where pathlines, streamlines, and streaklines coincide there is little ambiguity as to the interpretation of the observations. In turbulent flows however, the path, stream, and streaklines differ from one another, and knowledge of any one alone does not satisfactorily describe the flow. The observation of pathlines alone can lead to misleading interpretations as was shown by Hama (1962). For a more complete picture of the flow characteristics additional information is required.

Working with hydrogen bubbles Schraub et al. (1965) overcame the interpretation problem by using "combined-time-streak markers". Employing a timeline made up of discrete bubbles they observed both the motion of the individual bubbles (pathlines) and the line connecting all bubbles initially generated at a given time (timeline).

Flow visualization naturally lends itself to unrecorded qualitative observations. Such qualitative observations have been made here in addition to the quantitative measurements, and serve as a valuable complement in some of the descriptions. However, these descriptions are clearly distinguished from the vast bulk of quantitative records. The presented flow patterns show the flow field velocities at each location

in both magnitude and direction. The prism-cine combination facilitated the detailed measurements of three-component velocity distributions in three-dimensional space.

Prism Calibration

The relationship between image separation and the distance of a particle from the prism is not quite linear because of the curved pipe wall and the different refractive indices of water, glass, and plexiglass. An analytical relationship is derived for the distance between the two particle images and particle distance from the tube wall, as shown in Appendix A, and the analytical expression is checked by calibrations described in Chapter 3. The spacings on the grid placed inside the pipe are Δr = 0.895 mm and $\Delta\Theta$= 3.35°. The axial spacing is the same as the radial and is used to estimate the overall scale factor.

The calibration readings are shown in table 5.1. In the table the "true radius" and "true angle" are the known values from the grid, while the other values are calculated using equations 2.1 and 2.2 and the co-ordinates read from the photograph. The calculated values show good agreement with the given co-ordiantes with only some noticeable difference in values at large angle Θ and small radius r. These differences may be caused by the assumption that the refractive indices of glass, glycerin, and plexiglass are the same, and by the difficulty in accurately measuring the distance between the pipe and the focus point of the camera.

Trace-Particle Flow Measurements

The experimental results presented here were determined for the fully developed turbulent flows of water in the 12.7 cm test pipe at a

TABLE 5.1 Calibration values for the prism analysis.

True radius	Radius	Angle	Radius	Angle	Radius	Angle
63.50	63.5	0.0	63.5	3.2	63.6	6.6
62.60	62.6	0.0	62.5	3.2	62.6	6.6
61.71	61.6	0.0	61.5	3.3	61.7	6.6
60.81	60.8	0.0	60.6	3.3	60.7	6.7
59.92	59.8	0.0	59.5	3.3	59.7	6.7
59.02	58.9	0.0	58.7	3.4	59.1	6.6
58.12	57.9	0.0	57.7	3.3	58.0	6.7
57.23	57.0	0.0	56.9	3.4	56.9	6.7
56.33	56.1	0.0	56.0	3.3	56.0	6.7
55.44	55.0	0.0	55.0	3.3	55.2	6.7
54.54	54.1	0.0	54.0	3.3	54.3	6.7
53.64	53.2	0.0	53.1	3.4	53.6	6.8
52.75	52.1	0.0	52.3	3.4	52.7	6.8
51.85	51.3	0.0	51.5	3.3	51.7	6.7
50.96	50.2	0.0	50.6	3.4	50.6	6.7
50.06	49.3	0.0	49.5	3.3	49.6	6.8
49.16	48.3	0.0	48.5	3.3	48.6	6.9
48.27	47.4	0.0	47.6	3.3	47.9	6.8
47.37	46.5	0.0	46.5	3.4	47.0	6.9
46.48	45.6	0.0	45.7	3.4	45.4	6.9
45.58	44.7	0.0	44.6	3.4	44.5	6.8
44.68	43.7	0.0	43.5	3.4	43.6	6.9
43.79	42.9	0.0	42.4	3.3	42.4	6.9
True angle		0.00		3.35		6.70

Reynolds number of 6,500. This flow rate corresponds to an average centerline velocity of 54.6 mm/s and a wall-friction velocity of 3.2 mm/s.

The flow studies concern a region near the wall of thickness 15 mm, width 13 mm, and length 24 mm as shown in figure 3.6, within which flow volume the three velocity components for each particle have been determined. The motions investigated do not occur in any one co-ordinate plane alone. Therefore, for better understanding of the three-dimensional velocity fluctuations, several two-dimensional, two-component velocity plots need to be viewed simultaneously.

As described in the discussion on computation, the velocity measurements are analyzed in two ways: one in which the measurements are used directly to obtain quantities such as mean velocities and turbulence intensities, and the other using an interpolating procedure by which the resulting flow patterns for the turbulent shear structure are recorded.

Mean velocities and turbulence intensities of the flow are given in table 5.2 and plotted in figures 5.1 and 5.2. The reference profiles given in these figures are those obtained using the hot-film anemometer with x-type probes, and the optical microscope arrangement for near-wall positions, as described in Chapter 4. Mean velocity values and fluctuation intensities have been averaged over the spatial domain as previously described (see figure 3.6) and over a relatively short time interval of one second. As is shown later, this time interval is not long enough to eliminate considerable fluctuation or scatter of the recorded values.

The agreement between the mean axial velocity of the trace-particle studies compared with the previously reported hot-film measurements in

TABLE 5.2 Averaged velocities obtained from the trace-particle measurements.

y/R	$\overline{U}/\overline{U}_o$	$\overline{V}/\overline{U}_o$	$\overline{W}/\overline{U}_o$	$u'/\overline{U}_o$	$v'/\overline{U}_o$	$w'/\overline{U}_o$
0.01	0.12	0.002	0.018	0.034	0.069	0.032
0.03	0.25	0.017	0.020	0.187	0.030	0.040
0.05	0.49	0.001	0.027	0.207	0.061	0.061
0.07	0.59	0.010	0.023	0.149	0.075	0.062
0.09	0.71	0.015	0.030	0.132	0.080	0.062
0.11	0.69	-0.020	0.030	0.188	0.082	0.081
0.13	0.79	0.003	0.030	0.124	0.090	0.064
0.15	0.77	-0.030	0.003	0.084	0.115	0.051
0.17	0.77	-0.027	-0.027	0.061	0.107	0.057
0.19	0.79	-0.009	-0.011	0.083	0.096	0.061
0.21	0.78	-0.0	-0.056	0.085	0.102	0.083
0.23	0.81	-0.025	-0.071	0.067	0.132	0.091
0.25	0.82	-0.009	-0.059	0.059	0.114	0.085

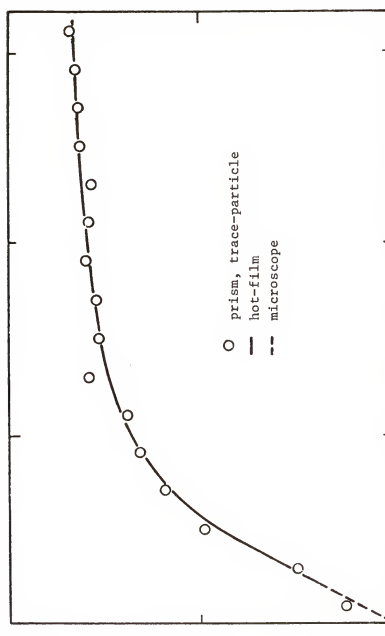

FIGURE 5.1 Mean velocity profile.

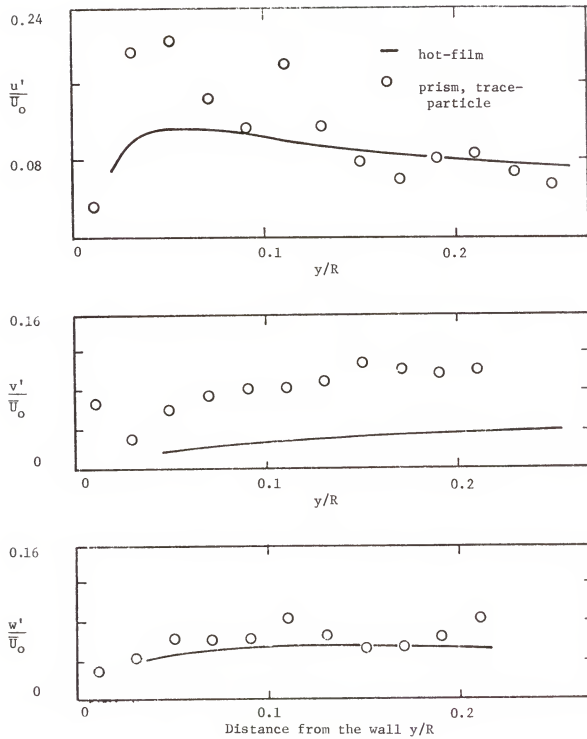

FIGURE 5.2 Relative turbulence intensities.

the core region of the flow, confirms the reliability of the trace-particle technique and allows for a study over the whole flow field, especially close to the boundary. The mean radial and circumferential velocities are found to be two orders of magnitude smaller than the average axial velocity, whereas instantaneous velocities show only one order of magnitude difference. The fact that the averaged velocity fluctuations are not zero is attributed again to the short averaging time, see table 5.2

The turbulence intensity measurements are still more sensitive to the length of the averaging time than are the averaged velocities, as is evident from the recorded results. The buffer zone, between the "viscous sublayer" and "logarithmic region" is one in which the anemometer records also show enormous scatter in intensities as can be seen in figures 4.10 through 4.21. The evaluation of intensity values from digitized data rather than continuous functional data may, in part, explain some of the scatter.

The non-zero averages of the radial and circumferential velocity fluctuations indicate that their intensities will be somewhat high, but they would be expected to reduce with a longer time record. As may be seen in the data for the structure of turbulent shear presented in the next section, one third of the time record of one second is involved in "bursting phenomena" in the near-wall and buffer regions. This "bursting" period is characterized by strong activity in the velocity field, which contributes to the overall high turbulence intensity values, particularly in the radial direction. In a more extended time record this "bursting" period would occupy less of the total time.

Despite the short time record and digitized discrete data the averages are good enough to check the reliability of the current measurements.

It is emphasized that averaged data are used as confirmation of the reliability of the applied techniques. Averaged data do not seem to give any new insight into the details of the structure of turbulence. They do, however, clearly indicate no slip at the boundary, and a maximum fluctuation intensity very close to the boundary.

Much effort has been devoted to interpretation of the records in order to describe details of the turbulent shear structure and velocity activity in the near-wall regions. Motions within the fluid near the wall appear to be crucial with regard to the mechanisms and details of turbulence generation, growth, and maintenance. In order to obtain these detailed velocity patterns, the necessary interpolation procedure possibly sacrifices up to 15% of the accuracy in the instantaneous values of the flow field velocity structure. Interpretation of the recorded data requires a time history of the instantaneous velocity values for each of the three components at many three-dimensional locations throughout the flow region under consideration.

Figures 5.6 through 5.26 show the three-dimensional velocity fields as they vary in space, and in time. The spatial measurements of the flow region studied are specified in Chapter 3 together with sketches of the shape and measurement of the chosen lattice for interpolation, as given in figure 3.8 and again in figure 5.3. In the velocity plots usually two components of velocity are plotted together so as to present the flow pattern in a plane. The radial-circumferential, axial-circumferential, and axial-radial plots are made using the same scale on each of twelve surfaces of constant radius, eleven planes of constant axial position, and seven planes of constant circumferential (aximuthal) angle. A view of one of each of these planes is shown in figure 5.4.

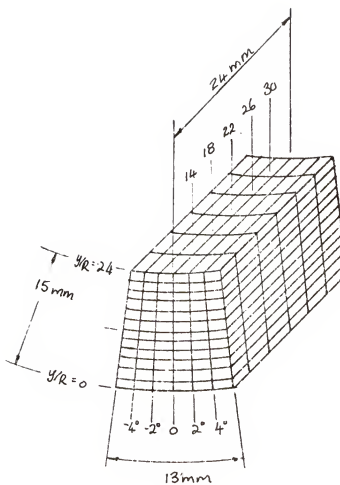

FIGURE 5.3 Lattice for interpolation

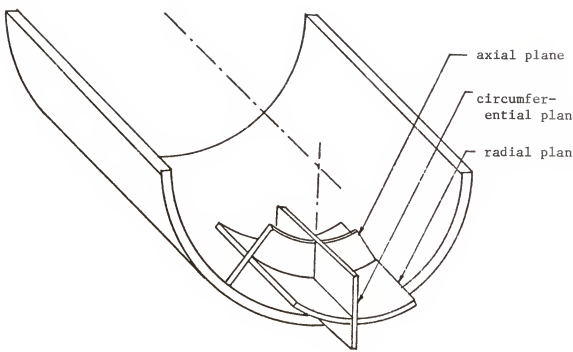

FIGURE 5.4 The axial, radial, and circumferential planes.

For convenience the surface of constant radius will here be referred to as the radial plane, the plane of constant axial position as axial plane, and the plane of constant azimuthal angle as the circumferential plane. The non-dimensional distance from the wall y/R may be easily converted to the local wall Reynolds number by $y^* = u^* y/\nu = 203\ y/R$, where $u^* = 3.2$ mm/s, and $R = 63.5$ mm.

The arrangement for presenting the variation of the flow pattern in both time and three-dimensional space is shown in figure 5.5, where a summary shows which of the results appear in each of the figures 5.6 through 5.26. A sample set of data at one instant in time is given in table 5.3.

The following paragraphs describe the results presented in figures 5.6 through 5.26, but do not interpret their implications. Interpretation and comparison with prevailing ideas on the structure of turbulence will be discussed in Chapter 6.

Figure 5.6 shows the instantaneous velocity field in axial planes located at positions x = 10, 14, 18, and 22 mm at time t = 0.025 s. The motion in position x = 10 is largely one of circumferential sweeping with a change of sweep direction between y/R = 12 ($y^+ = 24$) and y/R = 16 ($y^+ = 32$). At x = 14 and 18, there is a strong and pronounced flow toward the wall except within a small local zone at $\Theta = 0°$. The motion away from the wall for this very wall-close position can also be seen in figure 5.9. Figure 5.9 shows the axial and radial velocity components plotted together. There are two plots, one which shows the total axial velocity $U = \overline{U} + u$ plotted together with the radial component v, and the other which shows just the fluctuating components u and v together. Both

Time	Plot of v,w in the axial plane	Plot of $\bar{U}$ + u,v and u,v in the circumferential plane	Plot of $\bar{U}$ + u A set of radial planes
0.025	figure 5.6	figure 5.7	
0.025		figure 5.8	
0.025		figure 5.9	
0.025		figure 5.10	
0.025		figure 5.11	figure 5.12
0.050	figure 5.14	figure 5.15	figure 5.13
0.075	figure 5.18	figure 5.16	figure 5.17
0.125	figure 5.19		
0.275	figure 5.20		
0.300	figure 5.21		
0.325	figure 5.22		
0.375	figure 5.23	figure 5.24	
0.425	figure 5.25		
0.475	figure 5.26		

FIGURE 5.5 Summary sheet for figures of velocity field patterns.

plots are presented in order to give a clear picture of the fluctuating motion, and at the same time to demonstrate the scale of the velocity fluctuations relative to the averaged velocities.

Figure 5.9 not only indicates a fluid motion away from the wall at positions very close to the wall, but it also shows what appears to be a rotational motion normal to both the axial and radial direction. The rotation is centered on $y/R = 0.09$ ($y^+ = 18$) and the vortex centerline is at an axial position of $x = 13.5$ mm.

The length of the rotational motion may be seen by looking at figures 5.7, 5.8, 5.10, and 5.11, which contain similar plots to figure 5.9, but for different circumferential positions $\Theta = -4°$, $-2°$, $2°$, and $4°$, respectively. The rotational motion is clearly visible in each of these figures, but is perhaps most pronounced at $\Theta = -2°$. The center of rotation is located at approximately the same radial and axial position in each circumferential plane. For figures 5.10 and 5.11 corresponding to angular positions $\Theta = 2°$ and $\Theta = 4°$ the motion toward the boundary at the leading edge of the rotation appears to be much stronger than the motion away from the boundary at the trailing edge. Thus, this rotational motion appears to be something like a transverse vortex of at least 8 mm length. The plots in the same figures 5.7 through 5.11 also show that the motion is carried downstream by the mean flow, retarding the forward velocity near the wall, especially for $\Theta = 0$ as shown in figure 5.9.

The effects of the local motion away from the wall at $x = 14$ and $\Theta = 0°$ are not evident in the axial velocity plot of figure 5.12. However, such effects are noticeable a short time later at $\underline{t = 0.05\ s}$. Figure 5.13

which shows the axial velocity variation with circumferential position and distance from the wall y/R, clearly indicates a locally retarded flow zone at $\Theta = 0°$. At an axial position of x = 14 mm the slow zone extends to a distance of y/R = 0.08 (5 mm) from the wall. At this time there is also a noticeable rotation in the axial plane at x = 14, as shown in figure 5.14. The new rotational motion is centered at $\Theta = -1°$ and y/R = 0.11 ($y^+ = 22$) and is observable at x = 14 mm and maybe x = 18 mm. A look at the circumferential plane for $\Theta = -2°$ in figure 5.15 shows that the "transverse vortex" center has moved downstream to x = 16 and outward from the wall to y/R = 0.10 ($y^+ = 20$). This indicates that the eddy disturbance is travelling along the pipe about 100 mm/s (almost double the centerline velocity) and radially about 25 mm/s.

At time t = 0.075 s the transverse vortex center can be seen in figure 5.16 to have moved forward to x = 18 and outward from the wall to y/R = 0.12 ($y^+ = 24$), again showing a high axial propagation velocity of about 80 mm/s and a high radial velocity of about 25 mm/s. In figure 5.17 the "local slow zone" at x = 14 can also be seen to have moved to $\Theta = -1°$ and to have spread outward from the wall to include the axial velocity at y/R = 0.10 ($y^+ = 20$). The zone has expanded somewhat in the circumferential direction.

The flow patterns in the axial planes are shown in figure 5.18. The rotational motion previously seen only in plane x = 14 is still clearly visible at x = 14, but has also grown downstream and is noticeable at both x = 18 and x = 22. This suggests a rapid extension of this "streamwise vortex", the front end of the vortex disturbance propagating forward much faster than the average axial velocity. The vortex axis is inclined relative to the wall with its center at x = 14 located at $\Theta =$

$-1°$ and $y/R = .12$ ($y^+ = 24$) and its center $x = 22$ located at $\theta = -1°$ and $y/R = .16$ ($y^+ = 32$).

By time $t = .125$ s the streamwise vortex has travelled further downstream as may be seen in figure 5.19. The length of the vortex is not well defined, but the front end is certainly not propagating downstream as fast as it did before and the rotational motion can only be seen at $x = 18$ and 22.

Figure 5.20 at time $t = .275$ s shows the streamwise vortex after it has travelled further downstream and the portion showing rotation has expanded. The rotational motion or streamwise vortex is now seen at $x = 22$, 26, and 30. The estimated forward speed of the trailing end of the vortex is then about 36 mm/s and very close to the average forward speed of the flow at $y/R = .12$ ($\bar{U} = 40$ mm/s). The front end of the vortex is moving forward faster, but not by a large amount.

Only .025 seconds later at $t = .300$ s, the pattern has changed altogether. As is seen in figure 5.21 the streamwise vortex no longer exists. Figure 5.22 at time $t = .325$ s shows that the vortex motion is replaced by a strong radial motion directed outwards from the wall, as is seen at $x = 22$, 26, and 30. The motion is almost directly radial at $.10 \leq y/R \leq .20$, the same zone that previously contained the axis of the vortex.

The radial motion is at its strongest a short time later at $t = .375$ s. In figure 5.23 at $x = 30$ the radial flow is seen to be "ejecting" outward at a distance from the wall of $y/R = .12$ corresponding to ($y^+ = 24$). The radial component can also be seen in figure 5.25 in which the radial and axial velocities are plotted for the circumferential plane $\theta = 4°$. The axial velocity profiles show a depletion of the axial velocity

close to the boundary as was seen prior to and during the vortex motion, but does not exhibit the same inflexion profile.

The strong radial "ejection" only lasts for a short time interval, and by t = .425 s there is little evidence of it left as shown in figure 5.25. The motions recorded in figure 5.25 and later at t = .475 s in figure 5.26 show chaotic and non-distinctive patterns except perhaps for some fluid motion back towards the boundary in figure 5.26.

TABLE 5.3 Sample set of three-dimensional velocity data.

VELOCITY COMPONENTS FOR RE=6500 ON JAN 4 TIME= 2

X=10.0	THETA=-2. DEG			THETA= 0. DEG			THETA= 2. DEG		
Y/R=0.02	11.9.	-0.4.	0.5)	12.9.	-0.4.	0.8)	12.2.	-0.2.	1.4)
Y/R=0.04	23.0.	-0.8.	1.0)	25.4.	-0.7.	1.8)	24.0.	-0.3.	2.7)
Y/R=0.06	29.2.	-1.1.	1.2)	31.0.	-0.8.	2.2)	28.7.	-0.4.	3.3)
Y/R=0.08	35.6.	-1.3.	1.5)	35.7.	-0.9.	2.7)	33.2.	-0.5.	3.8)
Y/R=0.10	43.8.	-1.4.	2.1)	41.1.	-1.1.	3.1)	38.5.	-0.9.	4.0)
Y/R=0.12	47.4.	-0.8.	2.6)	41.2.	-1.2.	2.6)	39.6.	-1.3.	2.9)
Y/R=0.14	41.5.	0.2.	0.9)	40.1.	-0.6.	0.1)	40.1.	-1.2.	1.2)
Y/R=0.16	39.9.	0.5.	-1.3)	39.2.	-0.0.	-1.0)	40.4.	-1.0.	-0.3)
Y/R=0.18	39.7.	0.4.	-2.0)	39.3.	0.1.	-1.4)	40.3.	-0.5.	-1.1)
Y/R=0.20	39.9.	0.2.	-2.2)	39.6.	0.3.	-2.0)	40.2.	-0.0.	-1.9)
Y/R=0.22	40.3.	0.1.	-2.2)	40.2.	0.3.	-2.4)	40.4.	0.3.	-2.5)
Y/R=0.24	40.7.	0.1.	-2.2)	40.6.	0.2.	-2.4)	40.8.	0.4.	-2.9)

X=10.0	THETA=-4. DEG			THETA= 0. DEG			THETA= 4. DEG		
Y/R=0.02	8.2.	-0.3.	0.3)	12.9.	-0.4.	0.8)	9.8.	0.1.	1.7)
Y/R=0.04	16.4.	-0.6.	0.7)	25.4.	-0.7.	1.8)	20.4.	0.0.	3.4)
Y/R=0.06	22.8.	-0.8.	1.0)	31.0.	-0.8.	2.2)	25.6.	0.1.	4.1)
Y/R=0.08	32.5.	-0.8.	1.8)	35.7.	-0.9.	2.7)	30.9.	-0.1.	4.6)
Y/R=0.10	43.0.	-0.7.	3.2)	41.1.	-1.1.	3.1)	37.3.	-0.5.	4.1)
Y/R=0.12	42.5.	0.4.	3.9)	41.2.	-1.2.	2.6)	39.1.	-1.3.	2.9)
Y/R=0.14	41.6.	1.5.	5.0)	40.1.	-0.6.	0.1)	40.5.	-1.8.	1.6)
Y/R=0.16	41.3.	0.7.	1.5)	39.2.	-0.0.	-1.0)	41.4.	-1.4.	-0.3)
Y/R=0.18	40.6.	0.4.	-0.7)	39.3.	0.1.	-1.4)	41.2.	-0.9.	-1.1)
Y/R=0.20	40.4.	0.1.	-1.8)	39.6.	0.3.	-2.0)	41.0.	-0.4.	-1.9)
Y/R=0.22	40.4.	-0.1.	-2.1)	40.2.	0.3.	-2.4)	41.0.	0.2.	-2.9)
Y/R=0.24	40.7.	-0.2.	-1.9)	40.6.	0.2.	-2.4)	41.2.	0.5.	-3.7)

X=10.0	THETA=-6. DEG			THETA= 0. DEG			THETA= 6. DEG		
Y/R=0.02	0.0.	0.0.	0.0)	12.9.	-0.4.	0.8)	8.0.	0.1.	1.6)
Y/R=0.04	0.9.	-0.0.	0.0)	25.4.	-0.7.	1.8)	15.7.	0.2.	3.2)
Y/R=0.06	5.4.	-0.2.	0.2)	31.0.	-0.8.	2.2)	20.8.	0.4.	4.1)
Y/R=0.08	21.7.	0.3.	2.1)	35.7.	-0.9.	2.7)	27.4.	0.3.	4.8)
Y/R=0.10	41.6.	1.5.	5.0)	41.1.	-1.1.	3.1)	36.8.	-0.7.	4.2)
Y/R=0.12	41.6.	1.5.	5.0)	41.2.	-1.2.	2.6)	39.5.	-1.4.	2.6)
Y/R=0.14	41.6.	1.5.	5.0)	40.1.	-0.6.	0.1)	41.5.	-1.8.	1.2)
Y/R=0.16	41.6.	1.5.	5.0)	39.2.	-0.0.	-1.0)	42.6.	-1.7.	-0.6)
Y/R=0.18	41.3.	0.2.	1.5)	39.3.	0.1.	-1.4)	42.3.	-1.1.	-1.5)
Y/R=0.20	41.4.	-0.9.	-0.6)	39.6.	0.3.	-2.0)	42.1.	-0.4.	-2.7)
Y/R=0.22	41.4.	-1.3.	-1.3)	40.2.	0.3.	-2.4)	42.2.	0.4.	-4.2)
Y/R=0.24	41.4.	-1.3.	-1.2)	40.6.	0.2.	-2.4)	42.4.	0.9.	-5.7)

TABLE 5.3 - continued

VELOCITY COMPONENTS FOR RE=6500 ON JAN 4 TIME= 2

X=14.0	THETA=-2. DEG			THETA= 0. DEG			THETA= 2. DEG		
Y/R=0.02	12.0.	1.6.	1.3)	9.2.	-0.3.	0.4)	10.0.	0.5.	1.2)
Y/R=0.04	23.6.	3.0.	2.5)	20.0.	-0.1.	1.5)	20.3.	1.1.	2.6)
Y/R=0.06	29.4.	3.7.	3.1)	26.6.	0.2.	2.3)	25.8.	1.3.	3.2)
Y/R=0.08	36.6.	4.0.	4.0)	32.6.	-0.0.	2.9)	31.8.	1.9.	3.5)
Y/R=0.10	42.7.	3.9.	4.8)	41.1.	1.5.	2.8)	37.1.	2.2.	3.1)
Y/R=0.12	42.3.	2.7.	4.7)	43.1.	2.7.	2.1)	39.8.	2.0.	2.3)
Y/R=0.14	40.9.	2.5.	3.4)	42.4.	2.8.	1.1)	42.1.	2.0.	1.1)
Y/R=0.16	40.3.	1.9.	1.6)	41.8.	2.4.	0.5)	42.7.	1.7.	0.3)
Y/R=0.18	40.1.	0.6.	0.1)	41.5.	1.7.	-0.4)	42.4.	1.3.	-0.4)
Y/R=0.20	40.5.	0.4.	-0.9)	41.2.	0.9.	-1.3)	42.2.	0.9.	-1.1)
Y/R=0.22	40.8.	0.3.	-1.4)	41.1.	-0.1.	-1.6)	42.0.	0.4.	-1.8)
Y/R=0.24	41.2.	0.1.	-1.3)	41.5.	0.2.	-1.8)	42.0.	-0.1.	-2.4)

X=14.0	THETA=-4. DEG			THETA= 0. DEG			THETA= 4. DEG		
Y/R=0.02	11.9.	3.1.	1.9)	9.2.	-0.3.	0.4)	10.2.	1.4.	1.6)
Y/R=0.04	23.5.	5.4.	3.5)	20.0.	-0.1.	1.5)	19.3.	2.3.	3.0)
Y/R=0.06	28.0.	5.4.	4.0)	26.6.	0.2.	2.3)	24.4.	2.2.	3.3)
Y/R=0.08	37.5.	5.9.	5.3)	32.6.	-0.0.	2.9)	30.0.	2.7.	3.5)
Y/R=0.10	42.3.	5.5.	5.9)	41.1.	1.5.	2.8)	35.8.	2.5.	3.0)
Y/R=0.12	42.0.	4.4.	5.8)	43.1.	2.7.	2.1)	38.6.	2.0.	2.3)
Y/R=0.14	41.7.	2.2.	5.2)	42.4.	2.8.	1.1)	41.3.	1.4.	1.4)
Y/R=0.16	41.1.	1.2.	3.5)	41.8.	2.4.	0.5)	43.1.	1.0.	0.2)
Y/R=0.18	40.5.	0.9.	1.9)	41.5.	1.7.	-0.4)	42.9.	0.8.	-0.4)
Y/R=0.20	40.5.	0.4.	0.5)	41.2.	0.9.	-1.3)	42.7.	0.6.	-1.1)
Y/R=0.22	40.8.	-0.0.	-0.5)	41.1.	-0.1.	-1.8)	42.5.	0.2.	-2.0)
Y/R=0.24	41.1.	-0.3.	-0.8)	41.5.	0.2.	-1.8)	42.5.	-0.4.	-2.9)

X=14.0	THETA=-6. DEG			THETA= 0. DEG			THETA= 6. DEG		
Y/R=0.02	10.9.	3.4.	1.9)	9.2.	-0.3.	0.4)	9.9.	1.7.	1.4)
Y/R=0.04	20.5.	6.3.	3.7)	20.0.	-0.1.	1.5)	19.4.	2.9.	2.9)
Y/R=0.06	24.7.	6.1.	4.1)	26.6.	0.2.	2.3)	23.7.	2.7.	3.2)
Y/R=0.08	36.3.	6.9.	5.6)	32.6.	-0.0.	2.9)	28.9.	2.6.	3.3)
Y/R=0.10	42.2.	6.2.	6.1)	41.1.	1.5.	2.8)	35.2.	2.5.	2.9)
Y/R=0.12	42.4.	5.1.	5.7)	43.1.	2.7.	2.1)	36.3.	1.8.	2.2)
Y/R=0.14	42.5.	3.8.	5.3)	42.4.	2.8.	1.1)	41.4.	1.1.	1.1)
Y/R=0.16	42.3.	3.0.	4.5)	41.8.	2.4.	0.5)	43.4.	0.5.	0.1)
Y/R=0.18	41.7.	1.7.	3.2)	41.5.	1.7.	-0.4)	43.3.	0.3.	-0.6)
Y/R=0.20	41.0.	0.0.	1.8)	41.2.	0.9.	-1.3)	43.1.	0.1.	-1.5)
Y/R=0.22	40.8.	-0.5.	0.5)	41.1.	-0.1.	-1.8)	43.0.	-0.4.	-2.6)
Y/R=0.24	41.0.	-0.9.	-0.3)	41.5.	0.2.	-1.8)	43.0.	-0.5.	-3.5)

TABLE 5.3 - continued

VELOCITY COMPONENTS FOR RE=6500 ON JAN 4 TIME= 2

	THETA=-2. DEG				THETA= 0. DEG				THETA= 2. DEG
X=26.0									
Y/R=0.02	3.4.	0.4.	0.5)(	2.5.	-0.8.	0.3)(	3.7.	-1.2.	0.5)
Y/R=0.04	10.7.	0.9.	1.2)(	6.4.	-1.3.	0.6)(	8.0.	-2.0.	0.7)
Y/R=0.06	17.6.	1.0.	1.4)(	14.4.	-0.7.	1.1)(	15.5.	-3.0.	0.7)
Y/R=0.08	31.4.	0.8.	1.9)(	27.9.	-1.7.	1.2)(	25.0.	-3.6.	0.7)
Y/R=0.10	36.1.	-0.4.	1.7)(	33.6.	-2.4.	1.2)(	31.1.	-4.1.	0.8)
Y/R=0.12	36.7.	-1.0.	1.6)(	35.7.	-2.9.	1.2)(	34.9.	-4.6.	1.0)
Y/R=0.14	37.2.	-1.9.	1.5)(	37.1.	-3.7.	1.3)(	37.7.	-5.3.	1.2)
Y/R=0.16	37.9.	-2.7.	1.4)(	38.4.	-4.5.	1.6)(	39.2.	-6.0.	1.5)
Y/R=0.18	38.9.	-3.4.	1.4)(	39.9.	-5.4.	1.8)(	41.2.	-7.0.	2.0)
Y/R=0.20	40.0.	-3.3.	1.5)(	41.4.	-6.7.	2.0)(	43.9.	-8.4.	2.5)
Y/R=0.22	41.4.	-2.6.	1.4)(	42.7.	-6.1.	2.2)(	46.4.	-7.7.	2.5)
Y/R=0.24	42.8.	0.7.	1.9)(	43.6.	-1.4.	1.6)(	47.7.	-4.4.	1.0)

	THETA=-4. DEG				THETA= 0. DEG				THETA= 4. DEG
X=26.0									
Y/R=0.02	9.7.	0.3.	1.1)(	2.5.	-0.8.	0.3)(	3.4.	-1.4.	0.5)
Y/R=0.04	18.9.	0.6.	2.1)(	6.4.	-1.3.	0.6)(	9.4.	-2.5.	0.7)
Y/R=0.06	22.2.	1.4.	2.3)(	14.4.	-0.7.	1.1)(	16.4.	-3.7.	0.8)
Y/R=0.08	34.1.	1.7.	2.7)(	27.9.	-1.7.	1.2)(	23.1.	-4.4.	0.4)
Y/R=0.10	38.9.	1.7.	2.5)(	33.6.	-2.4.	1.2)(	30.2.	-5.3.	0.5)
Y/R=0.12	38.9.	0.9.	2.1)(	35.7.	-2.9.	1.2)(	34.6.	-6.0.	0.8)
Y/R=0.14	38.5.	-0.0.	1.8)(	37.1.	-3.7.	1.3)(	38.7.	-6.6.	1.1)
Y/R=0.16	38.5.	-1.0.	1.7)(	38.4.	-4.5.	1.6)(	40.8.	-7.2.	1.6)
Y/R=0.18	39.1.	-1.7.	1.3)(	39.9.	-5.4.	1.8)(	43.7.	-8.0.	2.4)
Y/R=0.20	40.5.	-1.4.	1.2)(	41.4.	-6.7.	2.0)(	46.7.	-8.4.	3.2)
Y/R=0.22	42.1.	-0.5.	1.3)(	42.7.	-6.1.	2.2)(	48.0.	-7.0.	2.4)
Y/R=0.24	42.8.	0.7.	1.8)(	43.6.	-1.4.	1.6)(	49.6.	-4.1.	1.0)

	THETA=-6. DEG				THETA= 0. DEG				THETA= 6. DEG
X=26.0									
Y/R=0.02	11.1.	0.1.	1.2)(	2.5.	-0.8.	0.3)(	3.5.	-1.3.	0.4)
Y/R=0.04	21.3.	0.1.	2.3)(	6.4.	-1.3.	0.6)(	9.1.	-2.6.	0.5)
Y/R=0.06	25.4.	0.4.	2.6)(	14.4.	-0.7.	1.1)(	16.7.	-3.9.	0.5)
Y/R=0.08	33.9.	1.5.	3.3)(	27.9.	-1.7.	1.2)(	22.9.	-4.8.	0.4)
Y/R=0.10	36.2.	1.5.	3.2)(	33.6.	-2.4.	1.2)(	30.3.	-5.6.	0.2)
Y/R=0.12	39.8.	1.5.	2.5)(	35.7.	-2.9.	1.2)(	35.8.	-6.3.	0.6)
Y/R=0.14	38.5.	1.7.	1.9)(	37.1.	-3.7.	1.3)(	40.4.	-7.0.	1.1)
Y/R=0.16	38.1.	1.1.	1.6)(	38.4.	-4.5.	1.6)(	43.3.	-7.7.	1.9)
Y/R=0.18	39.0.	-0.3.	0.9)(	39.9.	-5.4.	1.8)(	45.9.	-8.4.	2.9)
Y/R=0.20	41.3.	-0.8.	0.9)(	41.4.	-6.7.	2.0)(	48.8.	-8.7.	3.8)
Y/R=0.22	42.7.	0.4.	1.6)(	42.7.	-6.1.	2.2)(	50.3.	-6.4.	2.6)
Y/R=0.24	43.1.	1.0.	1.4)(	43.6.	-1.4.	1.6)(	50.0.	-4.1.	1.2)

TABLE 5.3 - continued

VELOCITY COMPONENTS FOR RE=6500 ON JAN 4 TIME= 2

X=18.0	THETA=-2. DEG				THETA= 0. DEG				THETA= 2. DEG	
Y/R=0.02	10.1.	2.6.	1.8)(	0.3.	-0.0.	0.0)(	7.9.		0.9.	1.2)
Y/R=0.04	16.5.	4.0.	3.3)(	8.9.	0.7.	1.6)(	13.8.		1.5.	2.0)
Y/R=0.06	29.9.	5.9.	5.A)(	21.7.	1.7.	3.8)(	21.9.		2.1.	3.2)
Y/R=0.08	36.9.	6.6.	6.7)(	29.9.	2.3.	5.2)(	27.6.		3.9.	3.8)
Y/R=0.10	43.2.	6.9.	7.9)(	38.1.	5.0.	5.9)(	33.2.		5.1.	3.9)
Y/R=0.12	43.2.	5.9.	7.6)(	39.6.	7.1.	5.3)(	36.6.		5.3.	3.4)
Y/R=0.14	43.3.	5.6.	6.9)(	41.3.	8.0.	4.2)(	40.3.		5.5.	2.9)
Y/R=0.16	43.3.	7.4.	6.5)(	43.6.	9.7.	2.7)(	42.1.		5.8.	2.4)
Y/R=0.18	42.5.	7.7.	2.1)(	43.6.	8.4.	2.3)(	43.6.		6.4.	2.0)
Y/R=0.20	41.5.	-2.0.	-1.8)(	43.2.	4.7.	1.0)(	43.7.		5.0.	0.9)
Y/R=0.22	42.3.	-0.9.	-1.2)(	43.5.	1.0.	-0.8)(	44.1.		2.4.	-0.4)
Y/R=0.24	42.7.	-0.4.	-1.0)(	44.1.	0.7.	-1.2)(	44.5.		0.5.	-1.4)

X=18.0	THETA=-4. DEG				THETA= 0. DEG				THETA= 4. DEG	
Y/R=0.02	13.1.	3.3.	2.4)(	0.3.	-0.0.	0.0)(	9.9.		1.6.	1.4)
Y/R=0.04	22.5.	4.7.	3.9)(	8.9.	0.7.	1.6)(	16.4.		2.3.	2.3)
Y/R=0.06	33.7.	6.4.	5.9)(	21.7.	1.7.	3.8)(	23.7.		3.1.	3.4)
Y/R=0.08	38.9.	6.7.	6.8)(	29.9.	2.3.	5.2)(	28.4.		4.0.	3.8)
Y/R=0.10	43.2.	7.0.	7.5)(	38.1.	5.0.	5.9)(	32.7.		4.5.	3.7)
Y/R=0.12	43.5.	6.8.	7.2)(	39.6.	7.1.	5.3)(	35.7.		4.7.	3.2)
Y/R=0.14	43.9.	6.4.	6.9)(	41.3.	8.0.	4.2)(	38.8.		4.8.	2.7)
Y/R=0.16	44.2.	6.5.	6.6)(	43.6.	9.7.	2.7)(	42.0.		4.7.	2.2)
Y/R=0.18	43.6.	5.3.	4.2)(	43.6.	8.4.	2.3)(	43.4.		4.9.	1.7)
Y/R=0.20	41.5.	-0.0.	-0.6)(	43.2.	4.7.	1.0)(	43.9.		4.3.	0.9)
Y/R=0.22	40.8.	-1.8.	-1.4)(	43.5.	1.0.	-0.8)(	44.3.		2.7.	-0.6)
Y/R=0.24	41.3.	-1.5.	-1.3)(	44.1.	0.7.	-1.2)(	44.6.		0.5.	-1.7)

X=18.0	THETA=-6. DEG				THETA= 0. DEG				THETA= 6. DEG	
Y/R=0.02	13.2.	3.1.	2.2)(	0.3.	-0.0.	0.0)(	9.9.		1.9.	1.3)
Y/R=0.04	23.5.	4.5.	3.9)(	8.9.	0.7.	1.6)(	17.0.		2.9.	2.3)
Y/R=0.06	33.7.	6.0.	5.6)(	21.7.	1.7.	3.8)(	23.5.		3.7.	3.3)
Y/R=0.08	39.7.	7.1.	6.5)(	29.9.	2.3.	5.2)(	27.4.		4.4.	3.6)
Y/R=0.10	43.9.	8.0.	7.0)(	38.1.	5.0.	5.9)(	31.7.		4.9.	3.7)
Y/R=0.12	44.2.	8.5.	6.9)(	39.6.	7.1.	5.3)(	34.9.		4.6.	3.2)
Y/R=0.14	44.7.	8.6.	6.6)(	41.3.	8.0.	4.2)(	38.2.		4.3.	2.6)
Y/R=0.16	45.1.	9.2.	6.3)(	43.6.	9.7.	2.7)(	42.2.		4.0.	2.0)
Y/R=0.18	45.2.	9.4.	5.1)(	43.6.	8.4.	2.3)(	43.6.		4.2.	1.5)
Y/R=0.20	43.9.	6.2.	2.4)(	43.2.	4.7.	1.0)(	43.8.		3.6.	0.6)
Y/R=0.22	41.8.	1.0.	-0.2)(	43.5.	1.0.	-0.8)(	44.3.		2.1.	-1.2)
Y/R=0.24	40.7.	-1.8.	-1.3)(	44.1.	0.7.	-1.2)(	44.8.		0.3.	-2.7)

TABLE 5.3 - continued

VELOCITY COMPONENTS FOR RE=6500 ON JAN 4 TIME= 2

	THETA=-2. DEG			THETA= 0. DEG			THETA= 2. DEG		
X=22.0									
Y/R=0.02	4.8.	-0.2.	0.5)	0.4.	-0.0.	0.0)	2.2.	-0.5.	0.2)
Y/R=0.04	14.5.	0.2.	1.9)	4.9.	-0.5.	0.3)	7.1.	-1.0.	0.7)
Y/R=0.06	25.2.	0.9.	3.2)	15.2.	-0.6.	1.4)	15.4.	-1.9.	1.5)
Y/R=0.08	34.1.	2.1.	4.3)	26.1.	0.6.	2.7)	22.5.	-2.7.	1.8)
Y/R=0.10	38.2.	2.1.	4.5)	33.3.	-0.4.	3.2)	30.1.	-3.9.	2.1)
Y/R=0.12	37.9.	1.1.	3.9)	34.6.	-1.5.	2.9)	33.9.	-4.8.	2.4)
Y/R=0.14	38.1.	0.1.	3.5)	36.5.	-3.1.	2.7)	37.5.	-5.2.	2.7)
Y/R=0.16	39.2.	-1.2.	2.4)	38.7.	-4.7.	2.7)	40.8.	-6.6.	3.2)
Y/R=0.18	39.9.	-2.8.	0.7)	41.9.	-6.0.	2.3)	44.8.	-7.6.	2.7)
Y/R=0.20	40.6.	-3.7.	-0.7)	43.9.	-4.5.	0.4)	46.3.	-4.8.	1.1)
Y/R=0.22	41.7.	-1.4.	-1.8)	43.9.	-1.6.	-1.0)	45.9.	-2.0.	-0.4)
Y/R=0.24	42.3.	-0.5.	-1.8)	43.6.	0.6.	-2.0)	45.5.	0.3.	-1.6)

	THETA=-4. DEG			THETA= 0. DEG			THETA= 4. DEG		
X=22.0									
Y/R=0.02	12.0.	-0.3.	1.3)	0.4.	-0.0.	0.0)	1.6.	-0.7.	0.3)
Y/R=0.04	21.3.	-0.0.	2.6)	4.9.	-0.5.	0.3)	8.4.	-0.7.	1.1)
Y/R=0.06	31.4.	0.8.	4.1)	15.2.	-0.6.	1.4)	18.4.	-1.6.	1.7)
Y/R=0.08	38.7.	1.9.	5.1)	26.1.	0.6.	2.7)	24.1.	-2.3.	1.8)
Y/R=0.10	42.9.	3.0.	5.7)	33.3.	-0.4.	3.2)	30.8.	-3.8.	2.0)
Y/R=0.12	42.0.	3.3.	5.3)	34.6.	-1.5.	2.9)	35.5.	-5.2.	2.3)
Y/R=0.14	41.0.	3.4.	4.7)	36.5.	-3.1.	2.7)	38.9.	-5.5.	2.6)
Y/R=0.16	40.3.	1.7.	2.6)	38.7.	-4.7.	2.7)	42.8.	-6.4.	3.0)
Y/R=0.18	40.0.	-0.3.	-0.4)	41.9.	-6.0.	2.3)	47.4.	-6.7.	2.6)
Y/R=0.20	40.7.	-2.3.	-2.1)	43.9.	-4.5.	0.4)	47.6.	-4.8.	1.1)
Y/R=0.22	40.7.	-2.4.	-2.1)	43.9.	-1.6.	-1.0)	47.2.	-1.9.	-0.4)
Y/R=0.24	41.7.	-2.3.	-2.1)	43.6.	0.6.	-2.0)	46.3.	-0.0.	-1.6)

	THETA=-6. DEG			THETA= 0. DEG			THETA= 6. DEG		
X=22.0									
Y/R=0.02	13.1.	-0.5.	1.3)	0.4.	-0.0.	0.0)	1.5.	-0.3.	0.2)
Y/R=0.04	24.2.	-0.4.	2.7)	4.9.	-0.5.	0.3)	7.4.	-0.1.	0.9)
Y/R=0.06	34.1.	-0.1.	4.0)	15.2.	-0.6.	1.4)	17.6.	-1.0.	1.5)
Y/R=0.08	39.4.	0.4.	4.9)	26.1.	0.6.	2.7)	24.9.	-1.9.	1.6)
Y/R=0.10	44.0.	2.5.	5.7)	33.3.	-0.4.	3.2)	32.6.	-3.4.	1.7)
Y/R=0.12	43.9.	4.5.	5.8)	34.6.	-1.5.	2.9)	37.1.	-5.7.	1.8)
Y/R=0.14	43.9.	6.7.	5.9)	36.5.	-3.1.	2.7)	41.7.	-7.1.	2.2)
Y/R=0.16	43.2.	6.6.	3.8)	38.7.	-4.7.	2.7)	46.9.	-8.4.	3.1)
Y/R=0.18	42.4.	2.6.	0.3)	41.9.	-6.0.	2.3)	49.2.	-7.0.	2.7)
Y/R=0.20	41.0.	-1.5.	-1.7)	43.9.	-4.5.	0.4)	49.3.	-4.7.	1.1)
Y/R=0.22	41.4.	-1.5.	-1.7)	43.9.	-1.6.	-1.0)	47.9.	-2.3.	-0.5)
Y/R=0.24	42.3.	-0.9.	-1.5)	43.6.	0.6.	-2.0)	46.7.	-0.4.	-1.6)

TABLE 5.3 - continued

VELOCITY COMPONENTS FOR RE=6500 ON JAN 4 TIME= 2

	THETA=-2. DEG			THETA= 0. DEG			THETA= 2. DEG		
X=30.0									
Y/R=0.02	7.5.	0.9.	1.0)	3.5.	0.2.	0.4)	3.6.	-0.6.	0.3)
Y/R=0.04	13.9.	1.6.	2.0)	9.2.	0.5.	0.6)	8.3.	-0.5.	0.4)
Y/R=0.06	19.1.	2.0.	2.2)	17.1.	0.4.	0.2)	16.1.	-0.5.	0.1)
Y/R=0.08	28.3.	1.2.	1.3)	28.6.	-0.2.	-0.5)	26.0.	-0.6.	-0.4)
Y/R=0.10	34.8.	0.2.	0.5)	35.3.	-1.1.	-0.8)	32.4.	-1.3.	-0.9)
Y/R=0.12	36.8.	-1.6.	-0.2)	36.5.	-2.5.	-0.6)	35.9.	-2.8.	-0.9)
Y/R=0.14	37.7.	-3.0.	-0.3)	37.2.	-3.5.	-0.6)	37.0.	-3.8.	-0.9)
Y/R=0.16	39.1.	-3.9.	-0.0)	37.9.	-4.6.	-0.7)	37.8.	-4.5.	-0.8)
Y/R=0.18	40.6.	-4.5.	0.4)	39.4.	-5.5.	-0.4)	38.6.	-5.4.	-0.8)
Y/R=0.20	42.5.	-3.3.	1.5)	40.7.	-4.7.	0.3)	39.5.	-5.7.	-0.7)
Y/R=0.22	44.2.	-0.6.	2.8)	43.4.	-1.8.	2.2)	42.8.	-4.3.	0.5)
Y/R=0.24	44.7.	1.1.	3.3)	44.8.	1.2.	3.4)	49.1.	-1.7.	2.9)
X=30.0	THETA=-4. DEG			THETA= 0. DEG			THETA= 4. DEG		
Y/R=0.02	11.2.	1.1.	1.7)	3.5.	0.2.	0.4)	2.7.	-1.0.	0.4)
Y/R=0.04	21.1.	2.1.	3.2)	9.2.	0.5.	0.6)	7.5.	-1.0.	0.6)
Y/R=0.06	23.8.	2.3.	3.6)	17.1.	0.4.	0.2)	15.4.	-1.2.	0.3)
Y/R=0.08	28.3.	2.5.	3.9)	28.6.	-0.2.	-0.5)	25.0.	-1.6.	-0.2)
Y/R=0.10	34.5.	1.8.	3.4)	35.3.	-1.1.	-0.8)	31.8.	-2.1.	-0.6)
Y/R=0.12	36.0.	0.1.	1.7)	36.5.	-2.5.	-0.6)	35.4.	-2.5.	-0.9)
Y/R=0.14	38.1.	-1.9.	0.5)	37.2.	-3.5.	-0.6)	36.9.	-3.5.	-0.8)
Y/R=0.16	40.1.	-2.5.	1.2)	37.9.	-4.6.	-0.7)	38.1.	-4.2.	-0.6)
Y/R=0.18	42.1.	-3.6.	1.7)	39.4.	-5.5.	-0.4)	39.4.	-5.2.	-0.5)
Y/R=0.20	43.7.	-1.3.	2.6)	40.7.	-4.7.	0.3)	39.6.	-5.1.	-0.5)
Y/R=0.22	44.7.	0.4.	3.2)	43.4.	-1.8.	2.2)	44.9.	-4.6.	1.0)
Y/R=0.24	44.8.	1.2.	3.3)	44.8.	1.2.	3.4)	52.1.	-3.3.	2.3)
X=30.0	THETA=-6. DEG			THETA= 0. DEG			THETA= 6. DEG		
Y/R=0.02	12.1.	1.1.	1.9)	3.5.	0.2.	0.4)	2.0.	-0.9.	0.3)
Y/R=0.04	22.8.	2.1.	3.5)	9.2.	0.5.	0.6)	3.6.	-1.6.	0.6)
Y/R=0.06	25.6.	2.4.	4.0)	17.1.	0.4.	0.2)	11.7.	-2.0.	0.6)
Y/R=0.08	30.9.	2.6.	4.5)	28.6.	-0.2.	-0.5)	22.3.	-2.5.	0.0)
Y/R=0.10	33.6.	2.9.	5.2)	35.3.	-1.1.	-0.8)	32.6.	-3.2.	-0.5)
Y/R=0.12	35.2.	1.3.	3.8)	36.5.	-2.5.	-0.6)	36.6.	-3.5.	-0.8)
Y/R=0.14	37.6.	-3.5.	0.2)	37.2.	-3.5.	-0.6)	37.1.	-3.9.	-0.7)
Y/R=0.16	41.3.	-2.6.	1.9)	37.9.	-4.6.	-0.7)	38.2.	-4.5.	-0.6)
Y/R=0.18	43.3.	-1.6.	2.8)	39.4.	-5.5.	-0.4)	39.1.	-4.6.	-0.1)
Y/R=0.20	44.7.	0.2.	3.3)	40.7.	-4.7.	0.3)	39.5.	-5.1.	0.4)
Y/R=0.22	44.8.	0.9.	3.3)	43.4.	-1.8.	2.2)	45.5.	-4.3.	1.4)
Y/R=0.24	44.9.	1.7.	3.3)	44.8.	1.2.	3.4)	51.8.	-3.3.	2.2)

TABLE 5.3 - continued

VELOCITY COMPONENTS FOR RE=6500 ON JAN 4 TIME= 2

X=34.0	THETA=-2. DEG				THETA= 0. DEG				THETA= 2. DEG		
Y/R=0.02	8.8.	0.9.	1.2)(	6.6.	0.7.	0.6)(	4.3.	0.4.	0.1)		
Y/R=0.04	14.6.	1.4.	1.9)(	10.9.	1.0.	0.6)(	9.2.	0.8.	0.2)		
Y/R=0.06	19.9.	1.8.	2.4)(	19.0.	1.7.	0.8)(	19.0.	1.6.	0.3)		
Y/R=0.08	25.5.	2.3.	2.1)(	24.6.	1.1.	0.6)(	25.8.	1.3.	0.2)		
Y/R=0.10	37.2.	-0.3.	0.6)(	35.8.	-1.2.	-0.2)(	36.1.	-1.3.	-0.2)		
Y/R=0.12	39.4.	-2.5.	0.1)(	37.5.	-2.8.	-0.5)(	37.5.	-2.6.	-0.4)		
Y/R=0.14	41.4.	-5.7.	-0.2)(	39.0.	-4.2.	-0.6)(	38.5.	-3.6.	-0.5)		
Y/R=0.16	42.8.	-8.2.	-0.5)(	40.5.	-5.7.	-0.6)(	39.3.	-4.4.	-0.5)		
Y/R=0.18	43.7.	-6.1.	-0.1)(	42.0.	-7.0.	-0.5)(	40.4.	-5.4.	-0.5)		
Y/R=0.20	44.1.	-7.8.	0.3)(	42.7.	-7.2.	-0.3)(	41.2.	-6.0.	-0.4)		
Y/R=0.22	44.8.	-6.4.	0.9)(	43.4.	-7.2.	0.0)(	41.5.	-6.3.	-0.4)		
Y/R=0.24	45.3.	-4.7.	1.5)(	44.4.	-6.4.	0.7)(	42.2.	-6.9.	-0.5)		
X=34.0	THETA=-4. DEG				THETA= 0. DEG				THETA= 4. DEG		
Y/R=0.02	11.6.	1.0.	1.8)(	6.6.	0.7.	0.6)(	1.9.	0.2.	0.0)		
Y/R=0.04	20.4.	1.8.	3.2)(	10.9.	1.0.	0.6)(	7.2.	0.6.	0.1.		
Y/R=0.06	27.1.	2.2.	3.7)(	19.0.	1.7.	0.8)(	16.7.	1.4.	0.2)		
Y/R=0.08	35.1.	2.6.	4.1)(	24.6.	1.1.	0.6)(	23.5.	0.9.	0.3)		
Y/R=0.10	44.1.	2.9.	4.4)(	35.8.	-1.2.	-0.2)(	36.4.	-1.4.	-0.0)		
Y/R=0.12	46.3.	1.1.	3.1)(	37.5.	-2.8.	-0.5)(	37.7.	-2.7.	-0.2)		
Y/R=0.14	46.3.	-2.8.	1.6)(	39.0.	-4.2.	-0.6)(	38.6.	-3.5.	-0.3)		
Y/R=0.16	45.5.	-5.8.	0.8)(	40.5.	-5.7.	-0.6)(	39.3.	-4.1.	-0.3)		
Y/R=0.18	44.6.	-7.9.	0.5)(	42.0.	-7.0.	-0.5)(	40.1.	-4.8.	-0.3)		
Y/R=0.20	44.9.	-7.0.	0.9)(	42.7.	-7.2.	-0.3)(	40.2.	-4.9.	-0.3)		
Y/R=0.22	45.3.	-5.3.	1.4)(	43.4.	-7.2.	0.0)(	40.2.	-4.9.	-0.3)		
Y/R=0.24	45.7.	-3.5.	1.9)(	44.4.	-6.4.	0.7)(	40.0.	-4.4.	-0.3)		
X=34.0	THETA=-6. DEG				THETA= 0. DEG				THETA= 6. DEG		
Y/R=0.02	12.3.	1.0.	1.9)(	6.6.	0.7.	0.6)(	0.0.	0.0.	0.0)		
Y/R=0.04	23.0.	1.6.	3.4)(	10.9.	1.0.	0.6)(	1.3.	0.1.	0.0)		
Y/R=0.06	31.8.	2.1.	4.1)(	19.0.	1.7.	0.8)(	9.4.	0.8.	0.1)		
Y/R=0.08	38.5.	2.5.	4.4)(	24.6.	1.1.	0.6)(	19.6.	-0.0.	-0.3)		
Y/R=0.10	44.8.	2.7.	4.5)(	35.8.	-1.2.	-0.2)(	36.9.	-1.8.	0.3)		
Y/R=0.12	46.8.	2.7.	4.2)(	37.5.	-2.8.	-0.5)(	38.0.	-2.7.	0.2)		
Y/R=0.14	48.0.	0.8.	3.1)(	39.0.	-4.2.	-0.6)(	38.9.	-3.7.	0.1)		
Y/R=0.16	47.7.	-2.2.	2.3)(	40.5.	-5.7.	-0.6)(	39.6.	-4.4.	-0.0)		
Y/R=0.18	46.4.	-5.3.	1.6)(	42.0.	-7.0.	-0.5)(	39.8.	-4.5.	-0.1)		
Y/R=0.20	45.4.	-6.0.	1.4)(	42.7.	-7.2.	-0.3)(	39.8.	-4.4.	-0.1)		
Y/R=0.22	45.6.	-4.2.	1.8)(	43.4.	-7.2.	0.0)(	39.6.	-4.0.	-0.0)		
Y/R=0.24	45.8.	-2.7.	2.0)(	44.4.	-6.4.	0.7)(	39.5.	-3.9.	-0.0)		

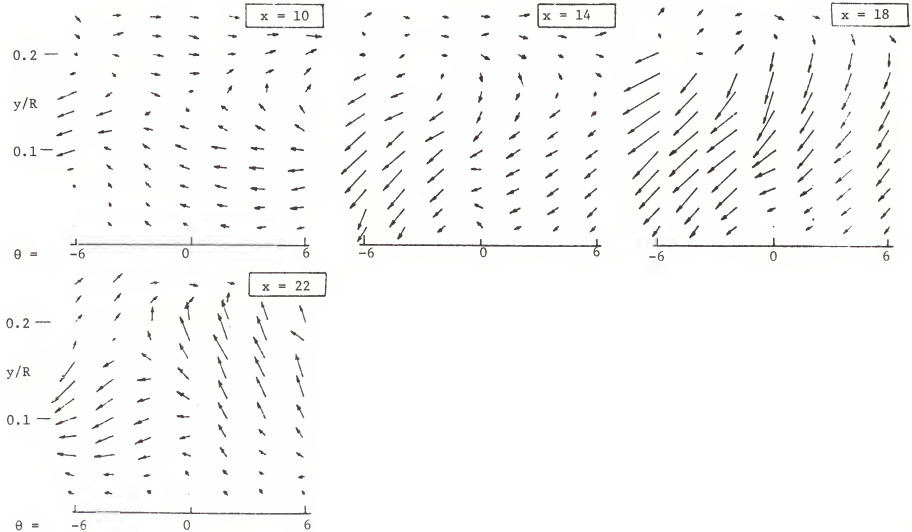

FIGURE 5.6 Velocity field for four axial planes at time t = 0.025 s.

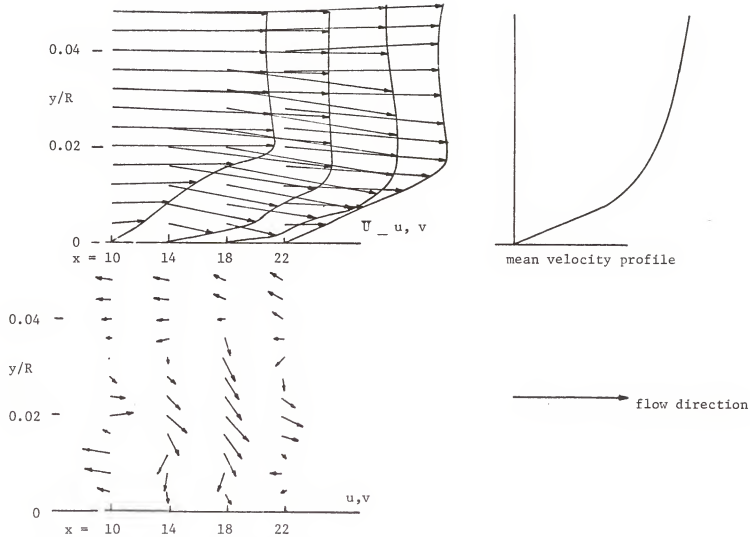

FIGURE 5.7 Velocity field on the circumferential plane $\Theta = -4°$ at time t = .025 s.

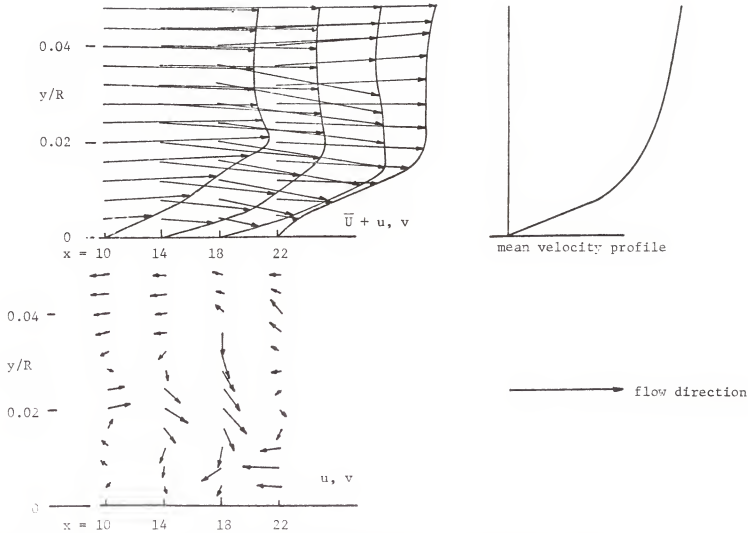

FIGURE 5.8 Velocity field on the circumferential plane $\theta = -2°$ at time t = .025 s.

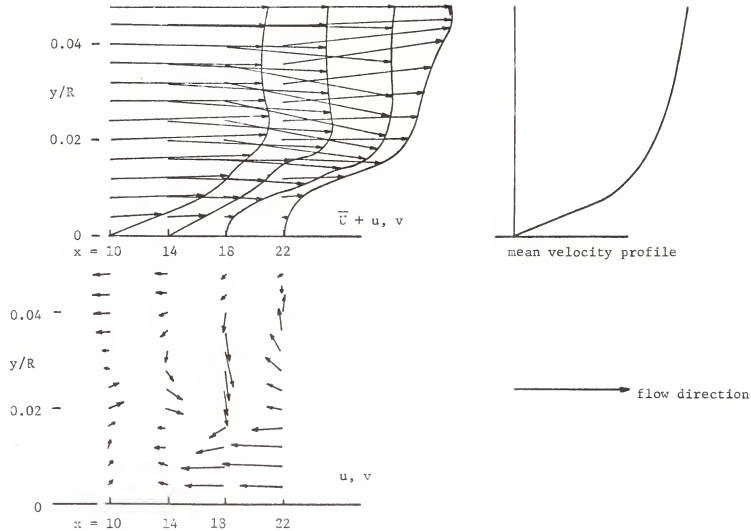

FIGURE 5.9 Velocity field on the circumferential plane $\theta = 0°$ at time t = .025 s.

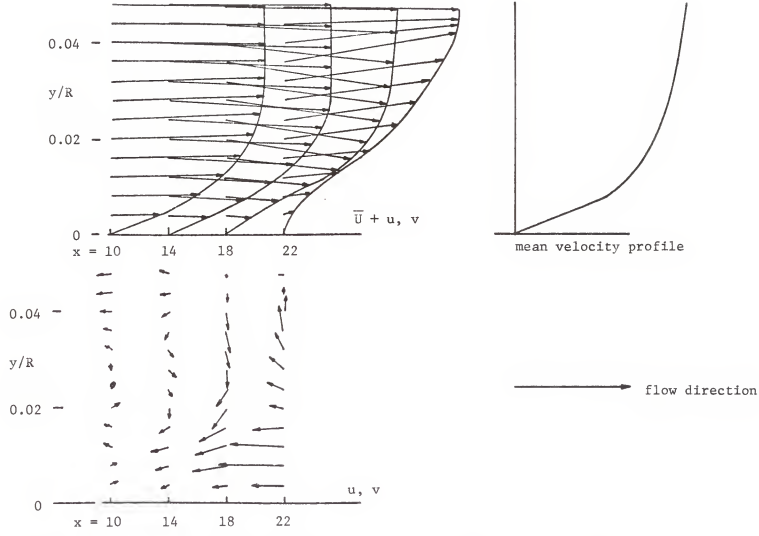

FIGURE 5.10 Velocity field on the circumferential plane Θ = 2° at time t = .025 s.

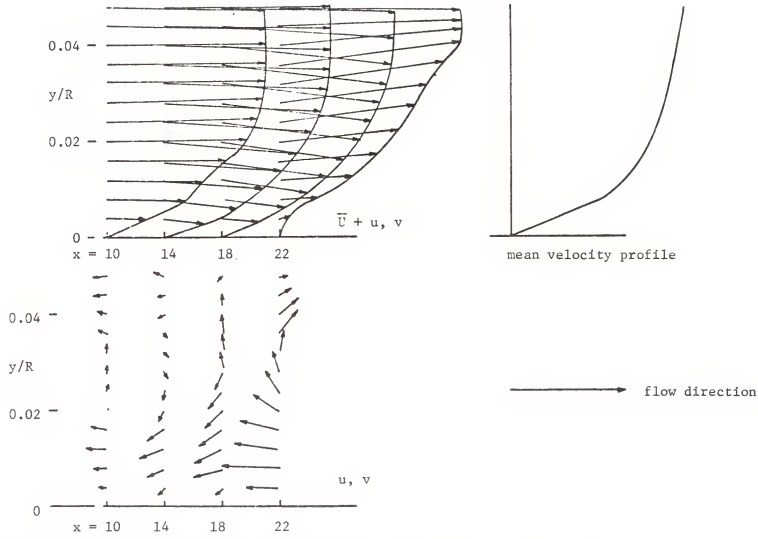

FIGURE 5.11 Velocity field on the circumferential plane $\Theta = 4°$ at time t = .025 s.

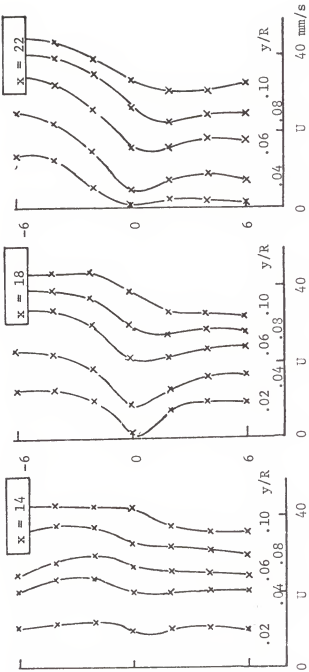

FIGURE 5.12 Axial-velocity field on three axial planes at time t = .025 s.

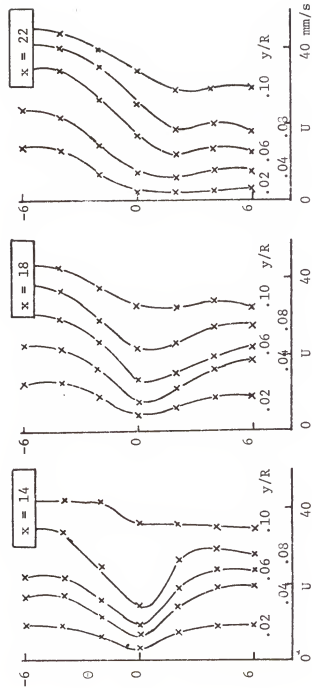

FIGURE 5.13 Axial-velocity field at three axial planes, at time t = .050 s.

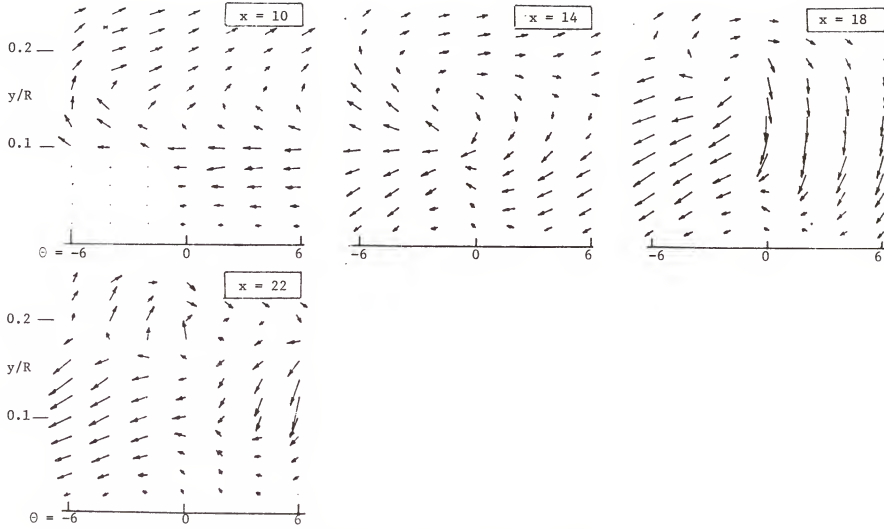

FIGURE 5.14 Velocity field on four axial planes at time t = .050 s.

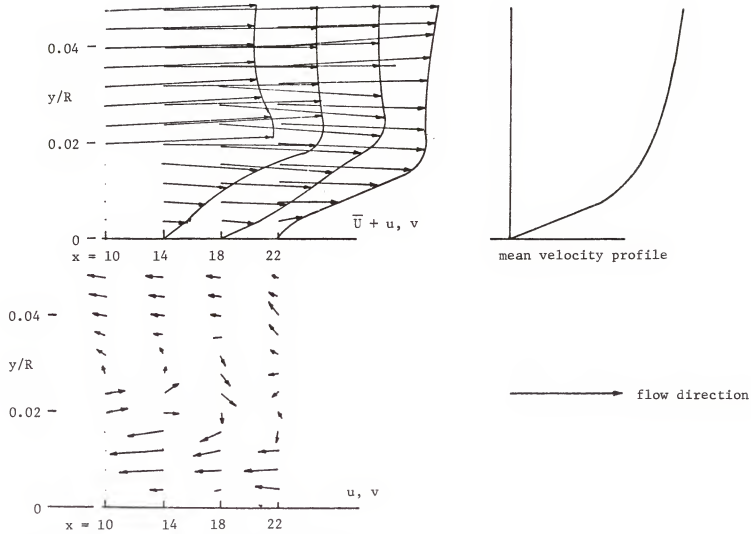

FIGURE 5.15 Velocity field on the circumferential plane $\Theta = -2°$ at time t = .050 s.

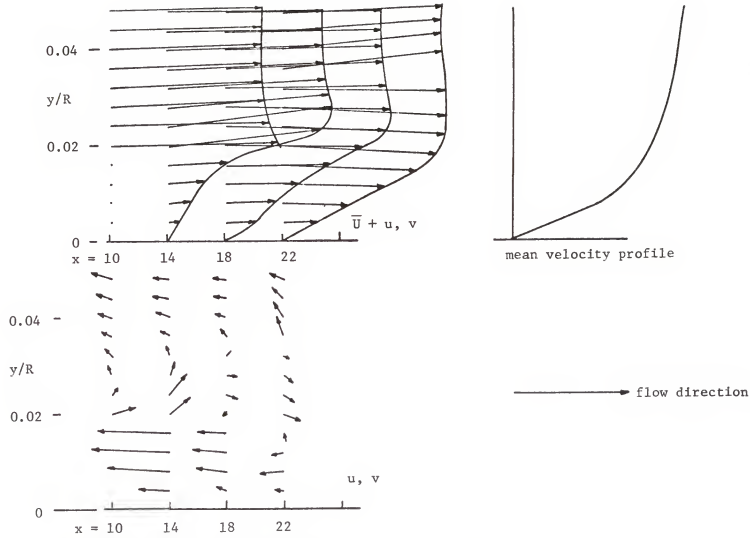

FIGURE 5.16 Velocity field on the circumferential plane $\Theta = -2°$ at time t = .075 s.

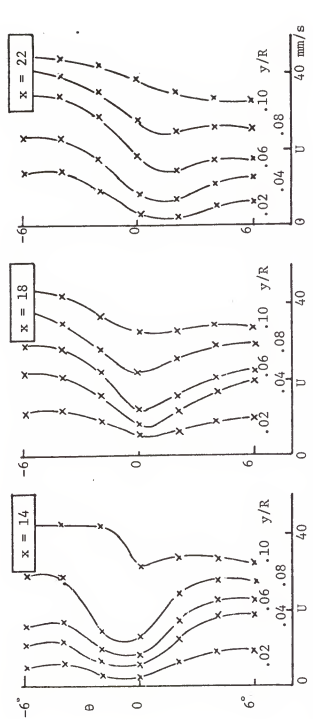

FIGURE 5.17 Axial-velocity field on three axial planes at time t = .075 s.

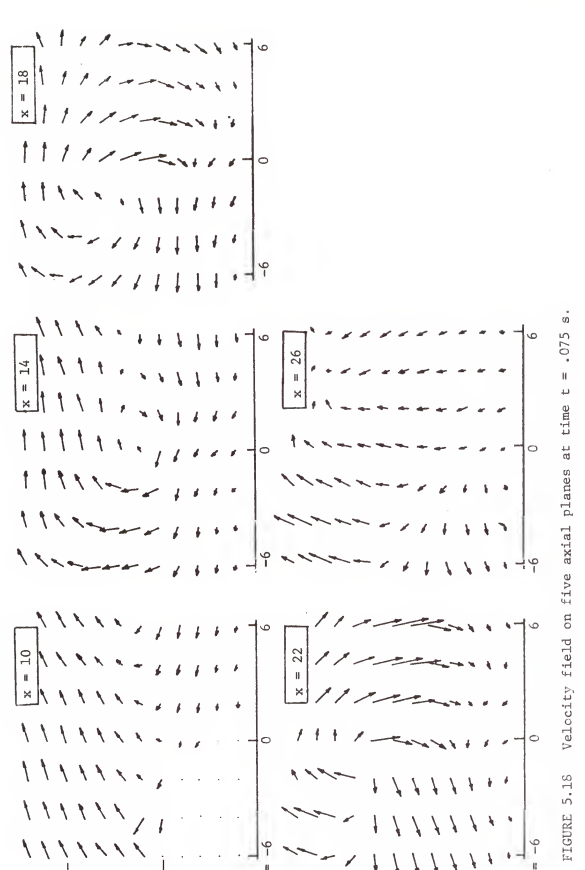

FIGURE 5.18 Velocity field on five axial planes at time t = .075 s.

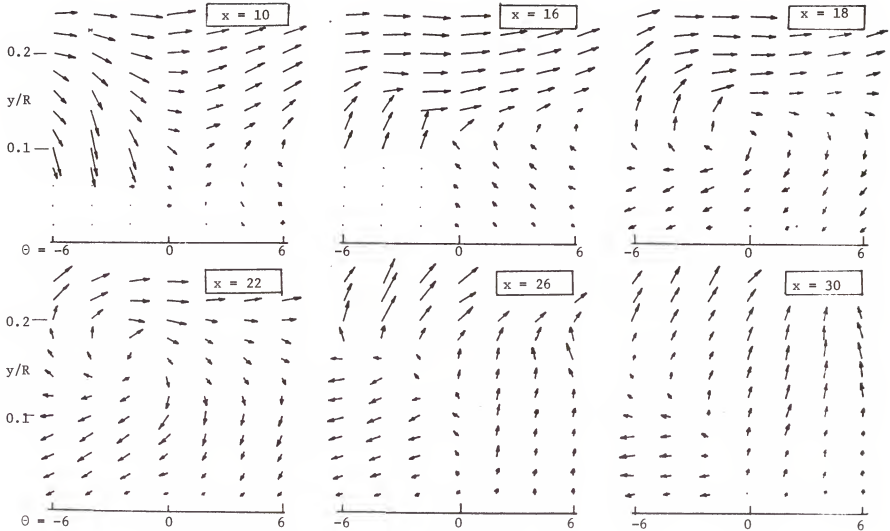

FIGURE 5.19 Velocity field on six axial planes at time t = .125 s.

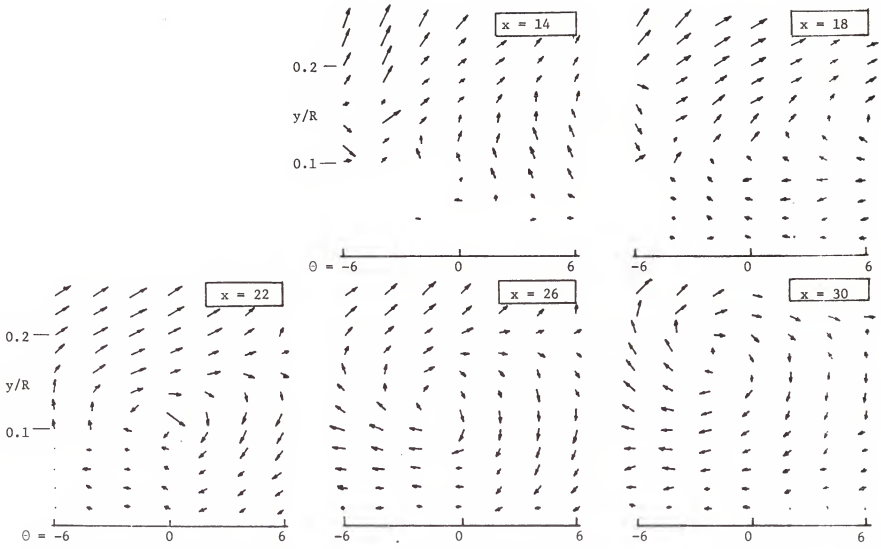

FIGURE 5.20 Velocity field on five axial planes at time t = .275 s.

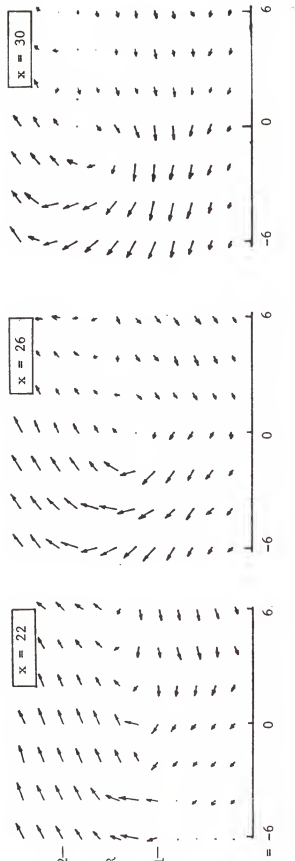

FIGURE 5.21 Velocity field on three axial planes at time t = .300 s.

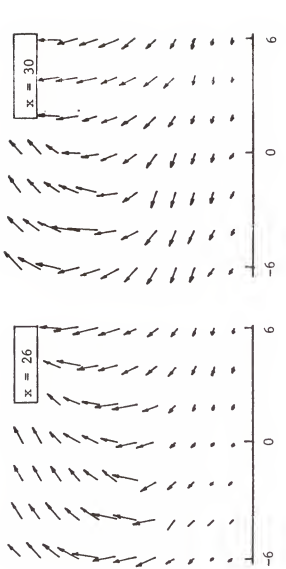

FIGURE 5.22 Velocity field on three axial planes at time t = .325 s.

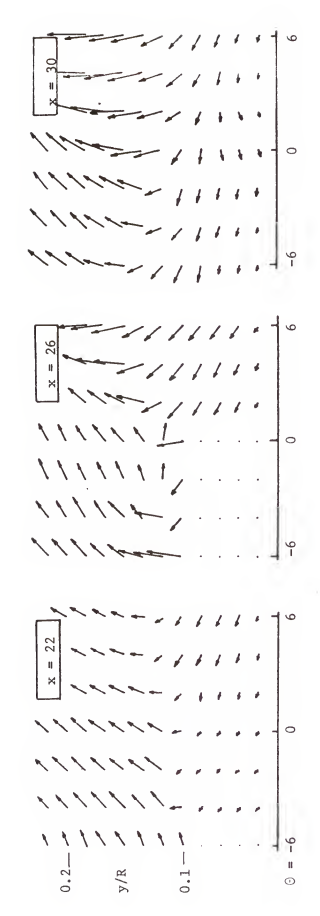

FIGURE 5.23 Velocity field on three axial planes at time t = .375 s.

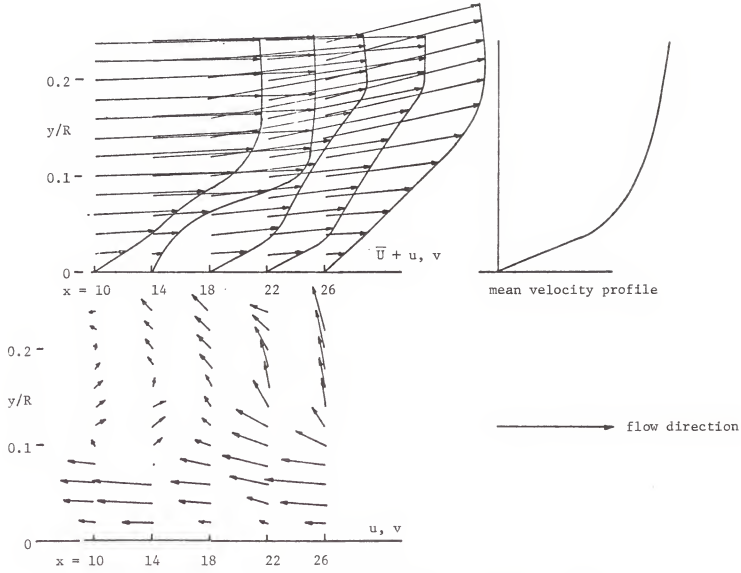

FIGURE 5.24 Velocity field on the circumferential plane $\Theta = 4°$ at time t = .375 s.

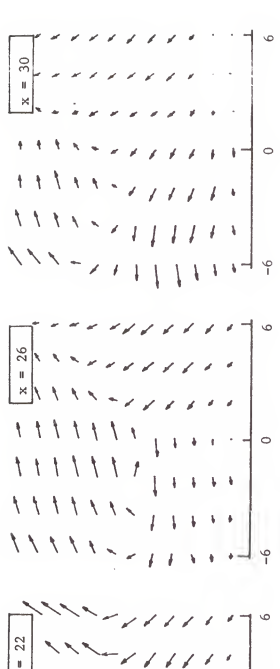

FIGURE 5.25 Velocity field for three axial planes at time t = .425 s.

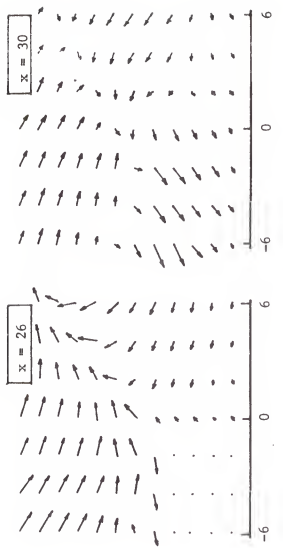

FIGURE 5.26 Velocity field on three axial planes at time t = .475 s.

CHAPTER 6
CONCLUSIONS

Discussion of Recorded Features of Wall Turbulence

The presented records for the three-dimensional velocity field variations in time and space are again sketched in figures 6.1, 6.2 and 6.3. From these figures it can be seen that there appear to be four consecutive types of motion involved; an axial flow retardation in the region adjacent to the wall; formation and growth of a streamwise vortex; a strong radial movement away from the wall; and a subsequent acceleration of the region adjacent to the wall. These motions are very similar to those described by Kline et al. (1967), Corino & Brodkey (1969), and Kim et al. (1971) and will be discussed in detail.

Figure 6.2 shows that there is initially a thin slow-speed zone close to the boundary. The axial velocity in this circumferentially-narrow zone is less than that of the average velocity at the same radius. This slower moving region lies within a distance $y^+ = 16$ ($y = 5$ mm) from the pipe wall. It has an axial extent of approximately $x^+ = 40$ and a shorter circumferential extent of approximately $\theta^+ = 10$. Upstream of the slow-speed zone the axial velocity is very much the same as that of the mean velocity, and can be expected to overtake the low speed zone. The chasing of fluid in the thin slow moving region, by a higher speed

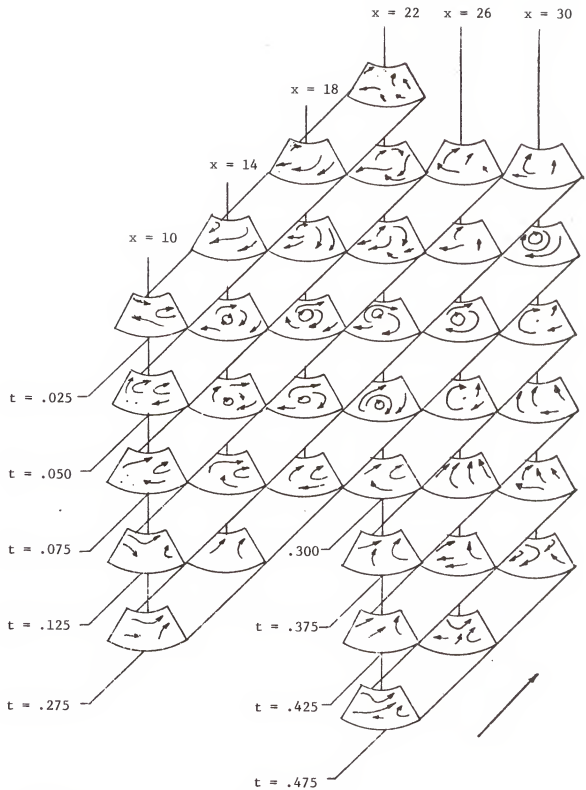

FIGURE 6.1 Summary of the velocity field in the axial planes.

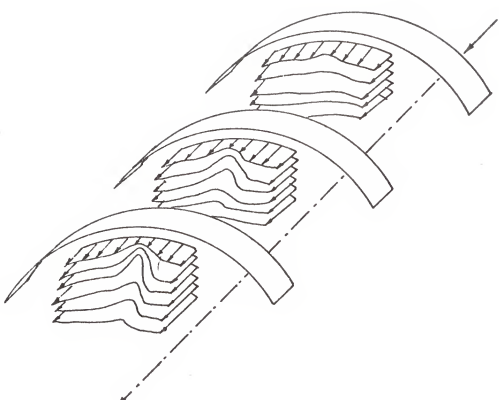

FIGURE 6.2 Summary of the axial velocity field.

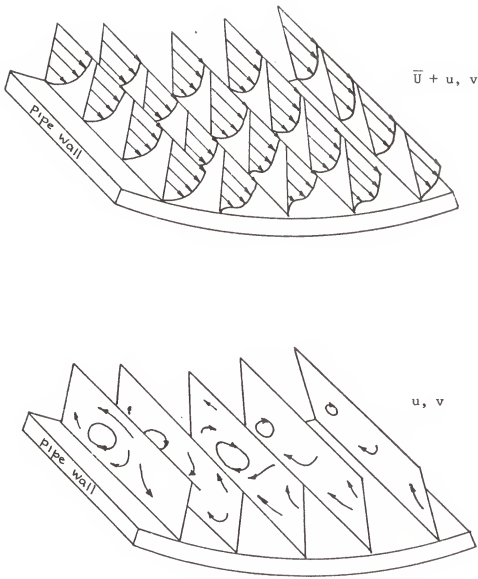

FIGURE 6.3 Summary of axial-radial velocity field.

zone just upstream, is clearly shown in figures 6.2 and 6.3. The graph of figure 6.3 may be interpreted as a transverse vortex being carried downstream by the average velocity or as a small slow speed streak being overtaken from the rear by a higher speed region.

Low and high speed streaks, first observed by Kline & Runstadler (1959), exist in the wall-near regions of more generally disturbed flow and consist alternately of regions of high and low forward velocities travelling side by side. The streaks are possibly formed by the stretching and compression of the spanwise vorticity component by the motion to or from the wall as described by Kline et al. (1967). Motion away from the boundary carries slow moving fluid into an otherwise faster moving region, and at the same time compresses the spanwise vorticity component thus producing a narrow low speed streak. The slow speed streaks have been observed by many authors to grow outwards from the wall as the streaks are carried downstream. Kline et al. (1967) attribute the "lifting" of the low speed streak to the streamwise vorticity. Corino & Brodkey (1969) describe the formation of a low-speed or "decelerated" region as the gradual replacement of fluid possessing the local mean velocity with fluid from upstream possessing a lower velocity. Corino & Brodkey (1969) also describe a faster moving or "accelerated" region upstream of the decelerated region. The accelerated region was observed by them to usually be moving toward the wall, just as in this study.

The low velocities in the low speed streak cause the instantaneous velocity profile to differ substantially from the mean velocity

profile (see figure 6.3). The instantaneous velocity profile possesses a narrow inflexion zone, at about $y^+ = 8$. The instantaneous inflexional profile seems to be associated with a rapidly growing streamwise vortex as seen in figure 6.1. An inflexional zone also occurs in the circumferential variation of the axial velocity but there is not a mean shear gradient as there is for the radial variation of the axial velocity. Therefore the circumferential variation is not thought to initiate the instability, but the presence of these local shear layers to either side of the inflected velocity profile is important to the growth of the subsequent motion.

The streamwise vortex, originating at the inflexional zone, appears to grow rapidly downstream in length and diameter. Figure 6.1 shows this growth while the motion is being transported downstream by the average motion. The vortical nature of this oscillatory growth may be related to the variation in the radial velocity with circumferential position of the higher speed region overtaking the low speed streak. Figure 5.6 shows that upstream of the low speed streak, at $x = 10$, the motion is radially outward from the wall to one side of the streak and toward the wall on the other. This change in radial velocity in the circumferential direction applies a "twist" to the disturbance growing out from the inflexional zone.

Kim et al. (1971) observed both the inflexional instantaneous profiles and subsequent streamwise vortices. Corino & Brodkey (1969) observing a much smaller region of flow, did not detect the vortical

nature of the disturbance, but described the motion in terms of the accelerated or high speed region interacting with the decelerated region. They describe an ejection of fluid from the decelerated region by action of the high shear region produced between the high and low speed zones. Their description of "ejection" includes also the next stage after the vortex formation and growth.

During the growth of the streamwise vortex there is little change in the retarded nature of axial velocity profile. After some time, however, the streamwise vortex suddenly loses identity and is replaced by a strong radial motion directed away from the boundary; see figure 6.1. This radial efflux carries with it the low velocities near the wall and extends the slow moving region outwards from the boundary. Although the axial velocity profile is further depleted, it no longer contains the inflexional character.

The cause of the sudden and strong motion originating in the same regions as occupied by the streamwise vortex and directed radially away from the boundary is not quite clear. Corino & Brodkey (1969) view the radial motion as part of the process of ejection already mentioned and caused by the interaction of the fast and slow moving regions producing a high shear zone. Kim et al. (1971) describe the chaotic motion following the termination of the oscillatory motion as "break-up". They suggest that the chaotic motions may arise from some secondary instability.

Figure 6.1 shows that the streamwise vortex changes character over its entire length simultaneously. The strong radial outward motion is almost immediately followed by chaotic set of motions. Finally, after some time the axial velocity near the boundary is accelerated. Since

there does not appear to be a strong enough radial component carrying the higher velocity into the wall region, the fluid must enter the region from a fast moving upstream region. Corino & Brodkey (1969) call this stage the "sweep".

Thus, the fluid motions observed here closely match the "burst" sequence of Kim et al. (1971) and the "ejection" process of Corino & Brodkey (1969). Because of the randomness of the phenomena studied, the very beginning of the burst sequence happened not to be included in the record, and due to the time consuming and cumbersome processes for evaluation of the film records it has not been possible at present to search the records for a second sequence.

Concluding Remarks

Only recently has it become a more popular view that self-preserving wall turbulence is not an entirely random process and cannot be adequately described in terms of averaged quantities alone, although such suggestions were advanced by Lindgren as long ago as 1957. According to the observations reported in this study, there appear to be certain distinctive patterns of motion in the high shear stress zone adjacent to the wall in fully developed turbulent pipe flow or turbulent boundary layer flow. These motions have been described in some detail before by Kline et al. (1967) and Kim et al. (1971) as "bursts",and by Corino & Brodkey (1969) as "ejections and sweeps".

The bursty nature of the wall turbulence must be of some importance in understanding the mechanisms involved in self-preserving turbulent flows. Kim et al. (1971) show that nearly all the turbulence production

in the region near the wall takes place during periods of bursting. Wallace, Eckelmann & Brodkey (1972) classify the turbulent velocity components and show that the ejection type motion (u negative and v positive) contributes 70% of the Reynolds stress term $-\rho\overline{uv}$, while the sweep type motion (u positive and v negative) also contributes 70%. The excess of 40% is accounted for by the interaction between the ejection and sweep motions.

The existence of such motions highlights the failing of the statistical theory to predict or describe the true nature of the structure of turbulent shear. Statistical averaging needs to take into account the special features of the turbulent flow.

The work presented in this study was initiated as an investigation into the wall region of fully developed turbulent pipe flow using hot-film anemometry to measure turbulent velocities under the critical conditions of energy balance found at lower Reynolds number flows. The averaged values of velocity and of turbulence intensity recorded, however, did not yield any new information regarding the mechanisms involved in the turbulent flow. Subsequent work utilizing trace particles was performed in order to better describe the detailed occurrence of velocity events.

The hot-film measurements of turbulent flow fields in pipe flow confirm certain well documented results. At the Reynolds numbers in question (Re = 4,000; 6,500; 9,000) the turbulence intensity is largest near the pipe wall, and the average velocity profile for the highest Reynolds number flow agrees with the universal velocity profile. However, certain other features are also clear, the velocity ratio in the

wall region varies with Reynolds number and the peak in the radial turbulence intensity is almost nonexistent at the lowest Reynolds number flow Re = 4,000.

The three-dimensional velocity field patterns obtained by measuring the velocity of trace particles in the viscous sublayer and buffer region of turbulent pipe flow show the bursty nature of wall turbulence. The important works of Kline et al. (1967), Kim et al. (1971), and Corino & Brodkey (1969) are essentially two-dimensional views of a three-dimensional motion. A special feature of the present study is that it determines the three-dimensional velocity pattern in a volumetric flow region, and therefore makes much clearer the details of the bursting process. This is accomplished at the price of some error introduced by the interpolation procedure.

From the work presented the following conclusions may be drawn:

1. The bursting motion close to the wall for fully developed turbulent pipe flow of Reynolds number 6,500 consists of four consecutive stages: the lifting of a slow speed streak to a distance of $y^+ = 16$ from the wall; the formation and rapid growth of a streamwise vortex; the sudden and strong radial velocity away from the boundary, followed almost immediately by a more chaotic but weaker motion; and finally the acceleration of the low speed streak near the wall. These stages are in essential agreement with those described by Kline et al. (1967) and Kim et al. (1971) for turbulent boundary layer flows and by Corino & Brodkey (1969) for turbulent pipe flow. Stage three is previously described as chaotic, without mention of the especially strong radial velocities recorded here. The streamwise

vortex of stage two may perhaps result from the inflexion of the instantaneous velocity profile produced by the lifted low speed streak. The prime cause for the sudden change of flow pattern from a vortex to some radial ejection between stages two and three is not clear, and that it takes place over the whole length of the vortex at one and the same instant does not seem to have been observed by other authors.

2. The bursting motion is three-dimensional. All three velocity components are actively involved in each of the first three stages of bursting. The fourth stage involves only the axial and radial components of velocity where faster moving fluid moves toward the wall and subsequently overtakes the slow speed streak.

3. There is no evidence of slip at the wall for fully developed turbulent pipe flow. Measurements of the average velocity were made to within a distance of 0.06 mm ($y/R = 0.001$) from the pipe wall for three Reynolds numbers of flow; 4,000; 6,500 and 9,000 (for Reynolds number 6,500 the distance ratio $y/R = 0.001$ is equivalent to $y^+ = 0.2$). The average profiles were linear in the neighborhood of the wall and the least squares fit to the data passed through the origin for each Reynolds number flow.

4. The hot-film calibration data indicate the existence of a critical velocity value, below which the hot-film probe is insensitive to velocity change. With the present arrangement this critical value was measured to be 1.4 mm/s and is thought to be related to the free convection velocity from the heated film. For low velocities the square root of the velocity is found not to be proportional to the square of the hot-film anemometer output and the calibration

curve is therefore non-linear.

5. Turbulent velocity measurements made with the hot-film sensors were not reliable closer to the wall than 1 mm. Hot-film measurements of the velocity within 1 mm of the wall do not discriminate between flows of different low flow rates (Reynolds number less than 4,000). This insensitivity is not detected for measurements within the same wall near region at higher Reynolds number turbulent flows, but its existence at low Reynolds numbers removes any confidence in the interpretation of wall-near readings. The poor response characteristics of the hot-film sensor to low velocities, combined with wall interferences contribute to the uncertain response of the sensor in the wall-near region.
6. For turbulent pipe flows in which the Reynolds number is less than 9,000 there is a sizeable variation of velocity ratio $u^+ = \overline{U}/u^*$ with Reynolds number, in the "wall region". The wall region being located outside of the "viscous sublayer", but not extending into the core region. This variation does not appear to have been noted at higher Reynolds number flows.

Of the work presented the following items may be considered as new contributions to the study of turbulence:

1. A measuring technique is developed to measure three-dimensional turbulence velocities. The motions of a particle travelling with the fluid are recorded cinematographically through a glass prism. The glass prism affords a stereoscopic view of the flow field and in turn the three-dimensional location of each particle.

2. All three components of velocity are measured simultaneously at many locations throughout a volumetric flow region near the wall in fully developed turbulent pipe flow.
3. A velocity interpolation procedure is proposed for turbulent flows in which the velocity is known at many arbitrary positions. The procedure involves repeated interpolation using a weighting function which is improved on each cycle by comparison with the computed spatial correlation function.
4. A three-dimensional record of the detailed velocity field for a "burst" near the wall in self-preserving, fully developed turbulent flow is presented.
5. During "bursting" a particularly strong radial motion directed away from the wall is found to replace the streamwise vortex motion. This radial motion precedes the more chaotic motion of the third stage in the "bursting" sequence.
6. Prior to the formation of the streamwise vortex of the bursting sequence there exists a transverse vortex with its axis parallel to the wall and normal to the pipe axis. This vortex propagates at a velocity significantly faster than that of the average flow.
7. It is suggested that the shape of the radial turbulence intensity profile may be a criterion in determining whether the turbulence is self-preserving or not. The peak in the radial turbulence intensity profile near the wall, so clearly defined at higher Reynolds number flows, diminishes with decreasing Reynolds number. The Reynolds number at which this peak disappears may be related to the critical Reynolds number for self-preservation of turbulence.

APPENDIX A
ANALYSIS OF THE RELATIONSHIP BETWEEN PARTICLE POSITION IN THE FLOW AND PARTICLE POSITION AS SEEN IN THE PRISM

A glass prism can be used to observe simultaneously two views of the flow field. The technique is shown in figure A-1 for a prism and pipe combination. A point P in the flow field is seen at both position B and E in the two prism faces. The locations of B and E are then related to the co-ordinate position of point P. This relation is derived by expressing the co-ordinates of positions C and D in terms of known geometric quantities and the co-ordinate positions of B and E, and then intersecting lines PC and PD to find the co-ordinate position of point P.

The refractive indices of the glass prism, glycerin, and plexiglass wall are assumed to be the same. With the origin of a set of rectangular co-ordinates (y,z) lie at the center of the pipe as shown in figure A-1 the equations describing the line AB, line FB, line BC, line PC, and circle CD may be written as

line AB $\quad y = -\tan(\frac{\pi}{2} - \Omega)\ z + h$

line FB $\quad y = -\tan(\frac{\pi}{2} - \phi)\ z + d$

line BC $\quad y = \tan(\Omega + \delta)\ z + y_B - \tan(\Omega + \delta)\ z_B$

line PC $\quad y = \cot(\Theta_C + \gamma)\ z + y_C - \cot(\Theta_C + \gamma)\ z_C$

circle CD $\quad y^2 = R^2 - z^2$

where angles Ω, ϕ, δ, γ, and Θ are defined in figure A-1 and R is the radius of the pipe.

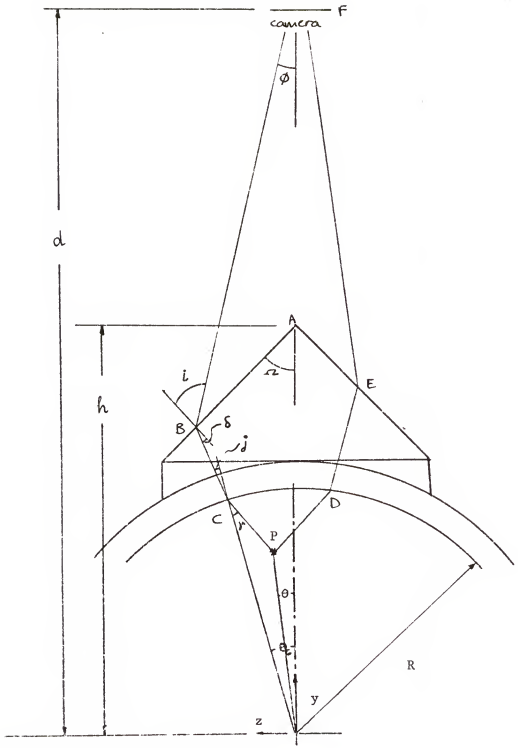

FIGURE A - 1 Prism mounted on the pipe

From Snell's law for refractive indices

$$\sin i/\sin \delta = n_g/n_a$$

$$\sin \gamma/\sin j = n_g/n_w$$

where $i = (\frac{\pi}{2} - \Omega) + \phi$ and n_g, n_a, and n_w are the refractive indices of glass, air, and water, respectively. Solving for δ and for γ in terms of Ω and ϕ yields

$$\delta = \sin^{-1} (n_a \sin (\frac{\pi}{2} - \Omega + \phi)/n_g \qquad \text{(A-1)}$$

and $$\gamma = \sin^{-1} (n_g \sin (\frac{\pi}{2} - \Omega + \phi)/n_w) \qquad \text{(A-2)}$$

Intersecting lines AB and FB to find angle ϕ gives

$$\phi = \tan^{-1} z_B/(d - h + \tan (90 - \Omega) z_B \qquad \text{(A-3)}$$

Intersecting line BC and circle CD to find the co-ordinates of C gives

$$z_C + (- a + \sqrt{b^2 - 4 ac})/2$$

and $$y_C = \sqrt{R^2 - z^2_C} \qquad \text{(A-4)}$$

where $a = 1 + \tan^2 (\Omega + \delta)$

$$b = 2 \tan (\Omega + \delta) y_B - 2 \tan^2 (\Omega + \delta) z_B$$

$$c = y^2_B - R^2 + \tan^2 (\Omega + \delta) z^2_B - 2 \tan (\Omega + \delta) z_B y_B \qquad \text{(A-5)}$$

Equations A-1 through A-5 express the co-ordinates of point C in terms of the co-ordinates of the image B in the prism face, the geometric quantities d, h, and Ω, and the refractive indices n_a, n_g, and n_w. The co-ordinates of the point D can be similarly expressed in terms of the co-ordinates of image E in the other prism face. For calculation purposes (z_D, y_D) is calculated by using z_E for z_B in equations A-1 through A-5 and afterwards setting $z_D = -z_C$, $y_D = y_C$ and $\gamma_D = \gamma_C$.

Intersecting lines PD and PC for the co-ordinates of point P gives

$$z_P = \frac{(\cot (\Theta_D + \gamma_D) z_D + \cot (\Theta_C - \gamma_C) z_C - \sqrt{R^2 - z^2_C} + \sqrt{R^2 - z^2_D}}{\cot (\Theta_C + \gamma_C) + \cot (\Theta_D + \gamma_D)}$$

$$y_P = \cot(\Theta_C + \gamma_C)(z_P - z_C) + \sqrt{R^2 - z_C^2} \qquad \text{(A-6)}$$

where $\Theta_C = \tan^{-1} z_C / \sqrt{R^2 - z_C^2}$

and $\Theta_D = \tan^{-1} - z_D / \sqrt{R^2 - z_D^2}$

Thus the position of particle P is expressed in terms of the co-ordinates of the images B and E in the two prism faces, the geometric quantities h, d, and Ω and the refractive indices n_a, n_g, and n_w.

For the purposes of this study $\Omega = \frac{\pi}{4}$, h = 108 mm, d = 558 mm, $n_a = 1.0$, $n_g = 1.49$ and $n_w = 1.33$.

A similar technique may be employed to simultaneously obtain two views of the flow field in a square pipe or tank, by utilizing the pipe or tank walls. The arrangement is shown in figure A-2. Following an analysis similar to that shown for the pipe-prism combination, the position of a point P may be expressed as a function of z_B, z_E, h, d, n_a, n_p, and n_w. The results of such an analysis yield

$$\delta_B = \sin^{-1}(n_a \sin(\tfrac{\pi}{2} - \Omega + \phi_B)/n_p)$$

$$\gamma_C = \sin^{-1}(n_a \sin(\tfrac{\pi}{2} - \Omega + \phi_B)/n_w)$$

$$\phi_B = \tan^{-1}[z_B/(d - h + \tan(90 - \Omega)\, z_B)]$$

$$z_C = (k - y_B + \tan(\Omega + \delta_C)\, z_B)/(\tan(\Omega + \delta_C) + \cot\Omega)$$

$$y_C = -\cot(\Omega)\, z_C + k \qquad \text{(A-7)}$$

and

$$\delta_E = \sin^{-1}(n_a \sin(\tfrac{\pi}{2} - \Omega + \phi_E)/n_p)$$

$$\gamma_D = \sin^{-1}(n_a \sin(\tfrac{\pi}{2} - \Omega + \phi_E)/n_w)$$

$$\phi_E = \tan^{-1}[z_E/(h - d + \tan(90 - \Omega)\, z_E)]$$

$$z_D = (y_E - k + \tan(\Omega + \delta_E)\, z_E)/(\tan(\Omega + \delta_E) + \cot\Omega)$$

$$y_D = \cot(\Omega)\, z_D + k \qquad \text{(A-8)}$$

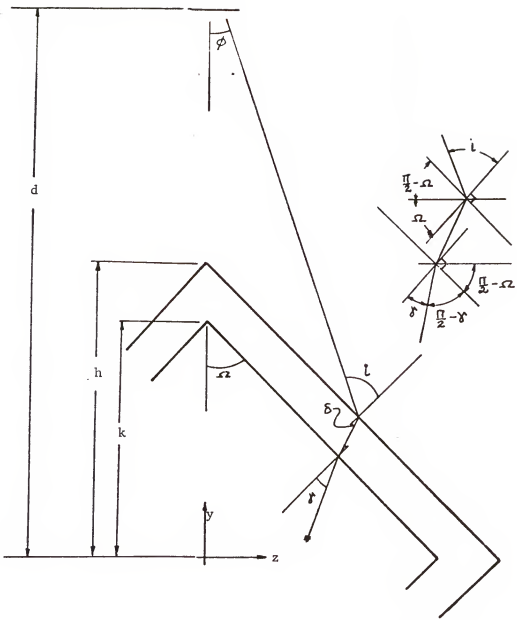

FIGURE A-2 Stereoscopic effect for square pipe.

Intersecting lines PC and PD gives

$$z_P = \frac{(\tan(\Omega + \gamma_D) - \cot\Omega)\, z_D + (\tan(\Omega + \gamma_C) - \cot\Omega)\, z_C}{\tan(\Omega + \gamma_D) + \tan(\Omega + \gamma_C)}$$

$$y_P = \tan(\Omega + \gamma_C)(z_P - z_C) - \tan(90 - \Omega)\, z_C + k \qquad \text{(A-9)}$$

Thus co-ordinates of point P (y_P, z_P) may be expressed in terms of the co-ordinates of image positions B and E, the geometry, and the material properties.

APPENDIX B

COMPUTER PROGRAM FOR THE EVALUATION AND INTERPOLATION OF THE VELOCITY FIELD

```
        COMPILER OPTIONS -  NAME=  MAIN,OPT=02,LINECNT=78,SIZE=0000K,
                            SOURCE,EBCDIC,NOLIST,DECK,LOAD,MAP,NOEDIT,ID,NOXREF
ISN 0002            DIMENSIONU(15),UX(15),UR(15),UT(15),X(80),R(80),T(80),VELX(80),
                   1VELR(80),VELT(80),XL(13,14,7),RL(13,14,7),TL(13,14,7),
                   2VELXL(13,14,7),VELRL(13,14,7),VELTL(13,14,7),CORRX(14,5),
                   3CORRR(14,5),CORNR(14,5),CORRT(14,5),NAX(14,5),NAR(14,5),
                   4NAN(14,5),NAT(14,5),D(13,14,7)
ISN 0003            DIMENSIONUA(16),VA(16),WA(16),NA(16),URA(16),VRA(16),WRA(16)
ISN 0004            TIME=0
ISN 0005            DO 50 M=1,14
ISN 0006            DO 51 N=1,5
ISN 0007            CORRX(M,N)=0
ISN 0008            CORRR(M,N)=0
ISN 0009            CORRT(M,N)=0
ISN 0010            CORNR(M,N)=0
ISN 0011            NAX(M,N)=0
ISN 0012            NAR(M,N)=0
ISN 0013            NAT(M,N)=0
ISN 0014            NAN(M,N)=0
ISN 0015         51 CONTINUE
ISN 0016            UA(M)=0
ISN 0017            VA(M)=0
ISN 0018            WA(M)=0
ISN 0019            NA(M)=0
ISN 0020            URA(M)=0
ISN 0021            VRA(M)=0
ISN 0022            WRA(M)=0
ISN 0023         50 CONTINUE
ISN 0024            READ(5,39)(U(I),I=1,14)
ISN 0025            READ(5,39)(UX(I),I=1,14)
ISN 0026            READ(5,39)(UR(I),I=1,14)
ISN 0027            READ(5,39)(UT(I),I=1,14)
ISN 0028            DO 399 I=1,14
ISN 0029            U(I)=54.6*U(I)
ISN 0030        399 CONTINUE
ISN 0031         39 FORMAT(14F4.3)
ISN 0032            DO 99 MAN=1,100
ISN 0033            READ(5,29)JRE,NAME
ISN 0034         29 FORMAT(I4,I2)
ISN 0035            IF(JRE.EQ.0) GO TO 66
ISN 0037            DO 12 I=1,100
```

```
ISN 0038            READ(5,11)LIME,X(I),R(I),T(I),VELX(I),VELR(I),VELT(I)
ISN 0039            LIMIT=I
ISN 0040            IF(LIME.EQ.0) GO TO 13
ISN 0042            MIME=LIME
ISN 0043         11 FORMAT(1X,I3,6F8.3)
ISN 0044         12 CONTINUE
ISN 0045         13 CONTINUE
ISN 0046            PI=1.570795
ISN 0047            DO 14 I=1,7
ISN 0048            DO 16 J=1,12
ISN 0049            DO 17 K=1,7
ISN 0050            XL(I,J,K)=4*I+6
ISN 0051            RL(I,J,K)=63.5*(1-0.02*J)
ISN 0052            TL(I,J,K)=2*(K-4)*PI/90
ISN 0053            X(LIMIT)=XL(I,J,K)
ISN 0054            R(LIMIT)=63.5
ISN 0055            T(LIMIT)=TL(I,J,K)
ISN 0056            PX=0
ISN 0057            BR=0
ISN 0058            BT=0
ISN 0059            C=0
ISN 0060            DO 15 L=1,LIMIT
ISN 0061            IF(X(L).LT.XL(I,J,K)-6.OR.X(L).GT.XL(I,J,K)+6) GO TO 15
ISN 0063            A=SQRT((X(L)-XL(I,J,K))**2+(R(L)*COS(T(L))-RL(I,J,K)*COS(TL(I,J,K)
                   1))**2+(R(L)*SIN(T(L))-RL(I,J,K)*SIN(TL(I,J,K)))**2)
ISN 0064            IF(A.GT.4) GO TO 15
ISN 0066            H=0
ISN 0067            IF(RL(I,J,K)-R(L).GT.63.5-RL(I,J,K)) H=(4-A)/4
ISN 0069            B=(4-A)/4
ISN 0070            PX=PX+VELX(L)*B
ISN 0071            BR=BR+VELR(L)*B
ISN 0072            BT=BT+VELT(L)*B
ISN 0073            C=C+B+H
ISN 0074         15 CONTINUE
ISN 0075            D(I,J,K)=1.0
ISN 0076            IF(C.EQ.0) D(I,J,K)=0
ISN 0078            IF(C.EQ.0) C=1
ISN 0080            VELXL(I,J,K)=PX/C
ISN 0081            VELRL(I,J,K)=BR/C
ISN 0082            VELTL(I,J,K)=BT/C
ISN 0083         17 CONTINUE
ISN 0084         16 CONTINUE
ISN 0085            WRITE(6,30)JRE,NAME,MIME
ISN 0086         30 FORMAT(1H1,10X,30HVELOCITY  COMPONENTS  FOR  RE=,I4,3X,
                   18HON   JAN,I2,8H   TIME=,I3,/)
```

```
ISN 0087            DO 18 KAD=1,3
ISN 0088            KAB=4-KAD
ISN 0089            KAC=4+KAD
ISN 0090            E=TL(I,1,KAB)*90/PI
ISN 0091            F=0.0
ISN 0092            G=TL(I,1,KAC)*90/PI
ISN 0093            WRITE(6,19)XL(I,1,1),E,F,G
ISN 0094         19 FORMAT(1H0,13X,2HX=,F4.1,9X,3(6HTHETA=,F3.0,4H DEG,8X))
ISN 0095            DO 20 J=1,12
ISN 0096            RADW=0.02*J
ISN 0097            WRITE(6,21)RADW
ISN 0098         21 FORMAT(14X,4HY/R=,F4.2)
ISN 0099            WRITE(6,22)(VELXL(I,J,K),VELRL(I,J,K),VELTL(I,J,K),K=KAB,KAC,KAD)
ISN 0100         22 FORMAT(1H+,22X,3(1H(,F5.1,1H,,F5.1,1H),))
ISN 0101         20 CONTINUE
ISN 0102         18 CONTINUE
ISN 0103         14 CONTINUE
ISN 0104            WRITE(6,601)MAN,MINE,LIMIT
ISN 0105        601 FORMAT(1H1,10X,I3,10X,I3,10X,I3)
ISN 0106            DO 200 IA=1,12
ISN 0107            J=IA
ISN 0108            DO 201 I=1,7
ISN 0109            DO 202 K=1,7
ISN 0110            UA(IA)=UA(IA)+VELXL(I,J,K)
ISN 0111            VA(IA)=VA(IA)+VELRL(I,J,K)
ISN 0112            WA(IA)=WA(IA)+VELTL(I,J,K)
ISN 0113            NA(IA)=I
ISN 0114            URA(IA)=URA(IA)+(VELXL(I,J,K)-U(J))**2
ISN 0115            VRA(IA)=VRA(IA)+VELRL(I,J,K)**2
ISN 0116            WRA(IA)=WRA(IA)+VELTL(I,J,K)**2
ISN 0117        202 CONTINUE
ISN 0118        201 CONTINUE
ISN 0119        200 CONTINUE
ISN 0120            DO 32 M=1,12
ISN 0121            DO 33 N=1,5
ISN 0122            DO 34 I=1,7
ISN 0123            DO 35 K=1,7
ISN 0124            IF(D(I,M,K).EQ.0) GO TO 35
ISN 0126            IF(VELXL(I,M,K).EQ.0.AND.VELRL(I,M,K).EQ.0.AND.VELTL(I,M,K).EQ.0)
                   1GO TO 35
ISN 0128            IF(I+N.GT.6) GO TO 36
ISN 0130            IF(D(I+N,M,K).EQ.0) GO TO 36
ISN 0132            IF(VELXL(I+N,M,K).EQ.0.AND.VELRL(I+N,M,K).EQ.0.AND.VELTL(I+N,M,K)
                   1.EQ.0) GO TO 36
ISN 0134            CORRX(M,N)=CORRX(M,N)+(VELXL(I,M,K)-U(M))*(VELXL(I+N,M,K)-U(M))
ISN 0135            NAX(M,N)=NAX(M,N)+1
ISN 0136         36 CONTINUE
```

```
ISN 0137            IF(I-N.LT.1) GO TO 361
ISN 0139            IF(I-N.LT.1.OR.D(I-N,M,K).EQ.0) GO TO 361
ISN 0141            IF(VELXL(I-N,M,K)*VELRL(I-N,M,K)*VELTL(I-N,M,K).EQ.0) GO TO 361
ISN 0143            CORRX(M,N)=CORRX(M,N)+(VELXL(I,M,K)-U(M))*(VELXL(I-N,M,K)-U(M))
ISN 0144            NAX(M,N)=NAX(M,N)+1
ISN 0145          361 CONTINUE
ISN 0146            IF(K+N.GT.7) GO TO37
ISN 0148            IF(D(I,M,K+N).EQ.0) GO TO 37
ISN 0150            IF(VELXL(I,M,K+N)*VELRL(I,M,K+N)*VELTL(I,M,K+N).EQ.0) GO TO 37
ISN 0152            CORRT(M,N)=CORRT(M,N)+VELTL(I,M,K)*VELTL(I,M,K+N)
ISN 0153            NAT(M,N)=NAT(M,N)+1
ISN 0154           37 CONTINUE
ISN 0155            IF(K-N.LT.1) GO TO 371
ISN 0157            IF(K-N.LT.1.OR.D(I,M,K-N).EQ.0) GO TO 371
ISN 0159            IF(VELXL(I,M,K-N)*VELRL(I,M,K-N)*VELTL(I,M,K-N).EQ.0) GO TO 371
ISN 0161            CORRT(M,N)=CORRT(M,N)+VELTL(I,M,K)*VELTL(I,M,K-N)
ISN 0162            NAT(M,N)=NAT(M,N)+1
ISN C163          371 CONTINUE
ISN 0164            IF(M+N.GT.12) GO TO 38

ISN 0166            IF(D(I,M+N,K).EQ.0) GO TO 38
ISN 0168            IF(VELXL(I,M+N,K)*VELRL(I,M+N,K)*VELTL(I,M+N,K).EQ.0) GO TO 38
ISN C170            CORRR(M,N)=CORRR(M,N)+VELRL(I,M,K)*VELRL(I,M+N,K)
ISN C171            NAR(M,N)=NAR(M,N)+1
ISN C172           38 CONTINUE
ISN 0173            IF(M-N.LT.1) GO TO 35
ISN 0175            IF(D(I,M-N,K).EQ.0) GO TO 35
ISN 0177            IF(VELXL(I,M-N,K)*VELRL(I,M-N,K)*VELTL(I,M-N,K).EQ.0) GO TO 35
ISN 0179            CORNR(M,N)=CORNR(M,N)+VELRL(I,M,K)*VELRL(I,M-N,K)
ISN 0180            NAN(M,N)=NAN(M,N)+1
ISN 0181           35 CONTINUE
ISN 0182           34 CONTINUE
ISN 0183           33 CONTINUE
ISN 0184           32 CONTINUE
ISN 0185            TIME=1
ISN 0186           99 CONTINUE
ISN 0187           66 CONTINUE
ISN 0188            WRITE(6,208) JRE
ISN 0189          208 FORMAT(1H1,10X,3HSET,I4,3X,5HUMEAN,2X,5HVMEAN,2X,5HWMEAN,2X,
                     14HURMS,3X,4HVRMS,3X,4HWRMS//)

ISN 0190            DO 206 J=1,12
ISN C191            RADW=0.02*J
ISN 0192            WALL=0
ISN 0193            IF(J.EQ.1) WALL=NA(J)/4
    0195            G=(NA(J)+WALL)*54.6
```

```
ISN 0196            AA=UA(J)/G
ISN 0197            BB=VA(J)/G
ISN 0198            CC=WA(J)/G
ISN 0199            DD=SQRT(URA(J)/G)/7.39
ISN 0200            EE=SQRT(VRA(J)/G)/7.39
ISN 0201            FF=SQRT(WRA(J)/G)/7.39
ISN 0202            WRITE(6,207)RADW,AA,BB,CC,DD,EE,FF
ISN 0203        207 FORMAT(11X,3HY/R,F4.2,2X,6F7.4)
ISN 0204        206 CONTINUE
ISN 0205            WRITE(6,47)
ISN 0206         47 FORMAT(1H0,10X,19HCORRELATION  COEFFS,/)
ISN 0207            WRITE(6,46)
ISN 0208         46 FORMAT(1H0,26X,35HN=1       N=2       N=3       N=4       N=5,/)
ISN 0209            DO 40 M=1,14
ISN 0210            RADW=0.02*M
ISN 0211            WRITE(6,21)RADW
ISN 0212            DO 41 N=1,5
ISN 0213            IF(M+N.GT.12) GO TO 48
ISN 0214            CORRR(M,N)=CORRR(M,N)/(NAR(M,N)*54.6*UR(M)*UR(M+N)*TIME*54.6)
ISN 0215         48 CONTINUE
ISN 0216            CORRX(M,N)=CORRX(M,N)/(NAX(M,N)*54.6**2*TIME*UX(M)**2)
ISN 0217            CORRT(M,N)=CORRT(M,N)/(NAT(M,N)*54.6**2*TIME*UT(M)**2)
ISN 0218         42 IF(M-N.LT.1) GO TO 41
ISN 0219            CORNR(M,N)=CORNR(M,N)/(NAN(M,N)*54.6*UR(M)*UR(M-N)*TIME*54.6)
ISN 0220         41 CONTINUE
ISN 0221            WRITE(6,44)(CORRX(M,N),N=1,5)
ISN 0222            WRITE(6,45)(CORRR(M,N),N=1,5)
ISN 0223            WRITE(6,45)(CORNR(M,N),N=1,5)
ISN 0224            WRITE(6,45)(CORRT(M,N),N=1,5)
ISN 0225         44 FORMAT(1H+,22X,5F8.3)
ISN 0226         45 FORMAT(1H0,22X,5F8.3)
ISN 0227         40 CONTINUE
ISN 0228            STOP
ISN 0229            END
```

BIBLIOGRAPHY

AHLBORN, F. 1902 Abhandl Gebiete Naturwiss. 17.

BAKER, D. J. 1966 J. Fluid Mech. 26, 573.

BAKEWELL, H. P. & LUMLEY, J. L. 1967 Phys. Fluids 10, 1880.

BATCHELOR, G. K. 1953 Theory of Homogeneous Turbulence. Cambridge University Press, Cambridge.

BOCK, PAUL 1963 Trans. New York Academy of Sciences Series II 25, 902.

BRODKEY, ROBERT S. 1967 The Phenomena of Fluid Motions. Addison-Wesley Publishing Company, Reading, Massachusetts.

CAFFYN, J. E. & UNDERWOOD, R. M. 1952 Nature 169, 239.

CLAUSER, F. H. 1956 Advances in Appl. Mechanics 4, 1.

COANTIC, MICHEL 1962 Publications Scientifiques et Techniques du Ministère de l'Air. N. T. 113.

COANTIC, MICHEL 1967a Comptes Rendus 264A, 826.

COANTIC, MICHEL 1967b Comptes Rendus 264A, 967.

COMPTE-BELLOT, G. 1965 Publications Scientifiques et Techniques du Ministere de l'Air. N. T. 419.

CORCOS, G. M. 1964 J. Fluid Mech. 18, 353.

CORINO, E. R. & BRODKEY, ROBERT S. 1969 J. Fluid Mech. 37, 1.

CORRSIN, S. & LUMLEY, J. 1956 Appl. Sci. Research, 6A, 114.

CUTTER, D. W. & SMITH, A. M. O. 1961 Aerospace Engineering 20, 24.

DEISSLER, R. G. 1958. Phys. Fluids 1, 111.

DRYDEN, H. L. 1939 Ind. Eng. Chem. 31, 416.

DRYDEN, H. L. & KUETHE, A. M. 1929 NACA Tech. Repts. No. 320.

EAGLE, A. & FERGUSON, R. M. 1930 Proc. Roy. Soc. (London) 127A, 540.

EDEN, C. G. 1912 Rept. of Nat. Advis. Comm. on Aeronautics 1911-1912, R. & M 58.

FAGE, A. & TOWNEND, H. C. H. 1932 Proc. Roy. Soc. (London) 135, 656.

GELLER, E. W. 1955 J. Aero. Sci. 22, 869.

HAGEN, G. 1839 Ann. d. Ph. und Ch. (2) 46, 423.

HAMA, FRANCIS R. 1962 Phys. Fluids 5, 644.

HEISENBERG, W. 1948 Z. Physik 124, 628; translation NACA TM 1431.

HINZE, J. O. 1959 Turbulence. McGraw-Hill, New York.

KIM, H. T., KLINE, S. J. & REYNOLDS, W. C. 1971 J. Fluid Mech. 50, 133.

KING, L. V. 1914 Phil. Trans. Roy. Soc. (London) 214A, 373.

KLEBANOFF, P. S. & TIDSTROM, K. D. 1959 NASA Tech. note D-195.

KLINE, S. J. 1965 Fluid Mechanics of Internal Flow. Proceedings of a Symposium, Warren, Michigan. Edited by Gino Sorran, Elsevier Publishing Company, Amsterdam.

KLINE, S. J., REYNOLDS, W. C., SCHRAUB, F. A. & RUNSTADLER, P. W. 1967 J. Fluid Mech. 30, 741.

KLINE, S. J. & RUNSTADLER, P. W. 1959 Trans. ASME(E), 81(3), 166.

KOLIN, A. 1944 J. Appl. Physics 15, 150.

KOLIN, A. 1953 Amer. J. Phys. 21, 619.

KOVASZANAY, L. 1947 NACA TM 1130.

KOVASZNAY, L. S. G., KOMODA, H. & VASUDEVA, B. R. 1962 Proceedings of the 1962 Heat Transfer and Fluid Mechanics Institute. Stanford University Press, Stanford, California.

LANDAHL, M. T. 1967 J. Fluid Mech. 29, 441.

LANDAHL, M. T. 1972a XIII IUTAM Congress, Moscow.

LANDAHL, M. T. 1972b J. Fluid Mech. 56, 775.

LANDAHL, M. T. 1973 International Symposium on Modern Developments in Fluid Dynamics. Haifa, Israel.

LAUFER, JOHN 1951 NACA Report 1053.

LAUFER, JOHN 1954 NACA Report 1174.

LIN, C. C. 1948 Proc. Natl. Acad. Sci. U.S. 34, 760.

LINDGREN, E. RUNE 1954 Arkiv för Fysik 7, 293.

LINDGREN, E. RUNE 1957 Arkiv för Fysik 12, 1.

LINDGREN, E. RUNE 1959a Arkiv för Fysik 15, 97.

LINDGREN, E. RUNE 1959b Arkiv för Fysik 15, 503.

LINDGREN, E. RUNE 1959c Arkiv för Fysik 16, 101.

LINDGREN, E. RUNE 1960a Arkiv för Fysik 18, 449.

LINDGREN, E. RUNE 1960b Arkiv för Fysik 18, 533.

LINDGREN, E. RUNE 1962 Arkiv för Fysik 23, 403.

LINDGREN, E. RUNE 1963 Arkiv för Fysik 24, 269.

LINDGREN, E. RUNE 1969 Phys. Fluids 12, 418.

LINDGREN, E. RUNE & CHAO, JUNN-LING 1969 Phys. Fluids 12, 1364.

LING, S. C. & HUBBARD, P. G. 1956 J. Aeronaut. Sci. 23, 890.

MAREY, 1893 Comptes Rendus 116, 913.

MORRISON, W. R. B., BULLOCK, K. J. & KRONAUER, R. E. 1971 J. Fluid Mech. 47, 639.

NEDDERMAN, R. M. 1961 Chem. Eng. Sci. 16, 113.

NIEUWENHUIZEN, J. K. 1964. Chem. Eng. Sci. 19, 367.

NIKURADSE, J. 1930 Proceedings of the Third International Congress of Applied Mechanics (Sveriges Litografiska Tryckerier, Stockholm) 1, 239.

NIKURADSE, J. 1932 VDI Forschungsheft No. 356.

PÉCLET, E. & MASSON, V. 1860 Traite de la Chaleur. Paris 1, 385; an English translation of parts in "Condensation of Steam in Covered and Bare Pipes" by C. P. Paulding, D. Van Nostrand Company, Inc., New York, N.Y. (1904)

PERRY, A. E. & MORRISON, G. L. 1971a J. Fluid Mech. 47, 577.

PERRY, A. E. & MORRISON, G. L. 1971b J. Fluid Mech. 47, 765.

PETERS, JEAN-LUC 1970 These Doctorat de Specialite. Universite D-Aix-Marseilles. Faculte des SCiences de Marseille. 1970.

POPOVITCH, A. T. & HUMMEL, R. L. 1967a Chem. Eng. Sci. 22, 21.

POPOVITCH, A. T. & HUMMEL, R. L. 1967b AICHE J. 13, 854.

PRANDTL, L. 1910 Physikalische Zeitschrift 11, 1072.

PRANDTL, L. & TIETJENS, O. G. 1925 Naturwissenschaften 13, 1050.

RAYLEIGH, LORD 1880 Proc. Math. Soc. (London) 11, 57.

REYNOLDS, O. 1883 Trans. Roy. Soc. (London) 174A, 935.

ROBERSON, E. C. 1955 NGTE Rept. No. R181.

SCHILLER, L. 1921 ZAMM 1, 436.

SCHRAUB, F. A., KLINE, S. J., HENRY, J., RUNSTADLER, P. W., & LITTELL, A. 1965 ASME J. Basic Eng. 87, 429.

SCHUBAUER, G. B. & KLEBANOFF, P. S. 1956 NACA Report 1289.

SCHUBAUER, G. B. & SKRAMSTAD, H. K. 1949 NACA Report 909.

SCHUBERT, GERALD & CORCOS, G. M. 1967 J. Fluid Mech. 29, 113.

STANTON, T. E. 1916 Great Britain Advisory Committee for Aeronautics; Reports and Memoranda No. 272.

STANTON, T. E., MARSHAL, DOROTHY & BRYANT, C. N. 1920 Proc. Roy. Soc. (London) 97, 413.

TAYLOR, G. I. 1916 Great Britain Advisory Committee for Aeronautics; Reports and Memoranda No. 272.

TAYLOR, G. I. 1935 Proc. Roy. Soc. (London) 151A, 421.

TAYLOR, G. I. 1936 Proc. Roy. Soc. (London) 156A, 307.

TAYLOR, G. I. 1938 Proc. Roy. Soc. (London) 164A, 476.

TCHEN, C. M. 1947 Ph.D. thesis, Delft.

TOLLMIEN, W. 1926 Z. angew. Math. u. Mech. 6, 468.

TOWNSEND, A. A. 1956 The Structure of Turbulent Shear Flow. Cambridge University Press, Cambridge.

VAN MEEL, D. A. & VERMIJ, H. 1961 Appl. Sci. Res. A10, 109.

VOGELPOHL, G. & MANNESMANN, D. 1946 NACA TM 1109.

VON KÁRMÁN, T. 1934. Proc. of the Fourth International Congress for Appl. Mech. Cambridge, England.

VON KÁRMÁN, T. & HOWARTH, L. 1938 Proc. Roy. Soc. (London) 164A, 192.

WALLACE, JAMES M., ECKELMANN, HELMUT & BRODKEY, ROBERT S. 1972 J. Fluid Mech. 54, 39.

WILLMARTH, W. W. & LU, S. S. 1973 J. Fluid Mech. 60, 481.

WILLMARTH, W. W. & TU, B. J. 1967 Phys. Fluids 10, S134.

WILLMARTH, W. W. & WOOLDRIDGE, C. E. 1962 J. Fluid Mech. 14, 187.

WOOD, W. W. 1968 J. Fluid Mech. 32, 3.

WYGNANSKI, I. J., & CHAMPAGNE, F. H. 1973 J. Fluid Mech. 59, 281.

WYGNANSKI, I. J., SOKOLOV, M. & FRIEDMAN, D. 1974 Final Report TAU/SOE - 94/74. Tel-Aviv University, School of Engineering, Ramat-Aviv, Israel.

BIOGRAPHICAL SKETCH

Richard Rushby Johnson was born in Cape Town, South Africa on January 27, 1948. He attended local primary school while growing up along with his three brothers on a small farm in the Cape Peninsula. His secondary school years were spent at Wynberg Boys High School in Cape Town. Upon completion of his matriculation, Richard entered the University of Cape Town as a student in mechanical engineering. Throughout his years at the university, Richard received a scholarship from Clifford Harris Civil Engineering Company and gained valuable experience working for this firm during school holidays. In December 1968 the author received his B. Sc. degree in Mechanical Engineering with First Class Honors. Continuing his studies at the same university, Richard did work for a Master of Science degree and conducted a high speed gas dynamic study for his thesis project. As a graduate assistant and as a junior lecturer after he completed the master's degree in December 1969, the author taught fluid mechanics and other courses in the department until August 1970. In the fall of 1970, Richard came to the United States to begin a Ph.D program in Engineering Sciences at the University of Florida.

I certify that I have read this study and that in my opinion it conforms to acceptable standards of scholarly presentation and is fully adequate, in scope and quality, as a dissertation for the degree of Doctor of Philosophy.

E. Rune Lindgren, Chairman
Professor of
Engineering Mechanics

I certify that I have read this study and that in my opinion it conforms to acceptable standards of scholarly presentation and is fully adequate, in scope and quality, as a dissertation for the degree of Doctor of Philosophy.

L. E. Malvern
Professor of
Engineering Mechanics

I certify that I have read this study and that in my opinion it conforms to acceptable standards of scholarly presentation and is fully adequate, in scope and quality, as a dissertation for the degree of Doctor of Philosophy.

U. H. Kurzweg
Associate Professor of
Engineering Mechanics

I certify that I have read this study and that in my opinion it conforms to acceptable standards of scholarly presentation and is fully adequate, in scope and quality, as a dissertation for the degree of Doctor of Philosophy.

A. A. Broyles
Professor of Physics

I certify that I have read this study and that in my opinion it conforms to acceptable standards of scholarly presentation and is fully adequate, in scope and quality, as a dissertation for the degree of Doctor of Philosophy.

R. J. Gordon

R. J. Gordon
Associate Professor of
Chemical Engineering

This dissertation was submitted to the Graduate Faculty of the College of Engineering and to the Graduate Council, and was acceptable as partial fulfullment of the requirements for the degree of Doctor of Philosophy.

December, 1974

Dean, College of Engineering

Dean, Graduate School